THE DEVELOPMENT OF HIGH MASS-SPECIFIC ACTIVITY RHODIUM SULFIDE CATALYSTS FOR HOR/HER IN HYDROGEN-BROMINE FUEL CELL

©2019

Yuanchao Li

Submitted to the graduate degree program in Department of Chemical and Petroleum Engineering and the Graduate Faculty of the University of Kansas in partial fulfillment of the requirements for the degree of Doctor of Philosophy.

Committee members

Dr. Trung Van Nguyen, Chair

Dr. Laurence Weatherley

Dr. Kevin Leonard

Dr. Juan Bravo Suarez

Dr. Xianglin Li

Date defended: Dec 12, 2018

The Dissertation Committee for Yuanchao Li certifies
that this is the approved version of the following dissertation :

THE DEVELOPMENT OF HIGH MASS-SPECIFIC ACTIVITY RHODIUM SULFIDE CATALYSTS FOR HOR/HER IN HYDROGEN-BROMINE FUEL CELL

Dr. Trung Van Nguyen, Chair

Date approved: Jan 29, 2019

Abstract

The integration of intermittent energies into the electrical grid like wind and solar power demands the participation of efficient and cost-effective energy storage systoms. H_2-Br_2 fuel cell is one of the promising technologies due to the advantage from the fast kinetics of Br_2/Br^- and low price of HBr. The corrosive nature of Br_2/Br^- determines that the metallic Pt is not a good choice for the HOR/HER catalysis on the negative electrode in the long-term operation of the fuel cell. The Rh_xS_y is free from the corrosion of the bromine and bromide. The low mass-specific surface area and activity of existing Rh_xS_y catalyst for HOR/HER, however, obstruct the deployment of the H_2-Br_2 fuel cell. In this dissertation, a clear roadmap to solve those problems has been demonstrated.

Core-shell structure was the first attempt to increase the mass-specific surface area of rhodium sulfide catalyst. Catalysts with Rh_xS_y as shell and different percentages (5%, 10%, and 20%) of platinum on carbon as core material were synthesized. The TEM and EDX results confirm the existence of the core-shell structure. Cyclic voltammetry was used to evaluate the Pt-equivalent mass specific ECSA and durability of these catalysts. Cycling test and polarization curve measurement in the H_2-Br_2 fuel cell were used to assess the catalyst stability and performance in a real fuel cell. The results show that the catalyst with core-shell structure has higher mass-specific ECSA ($50\ m^2/gm-Rh$) compared to a commercial catalyst (Rh_xS_y/C catalyst from BASF, $6.9\ m^2/gm-Rh$). It also shows better HOR/HER performance in the fuel cell. Compared to the platinum catalyst, the core-shell catalysts show more stable performance in the fuel cell cycling test. The cheap metal core material was also explored to replace the expensive Pt

material. However, the CV test suggests that the cheap metal catalyst was dissolved in the acidic $RhCl_3$ solution and then precipitated by the sulfide ion during the synthesis, which results in a lower ECSA/mass compared to the commercial catalyst.

Supporting carbon materials were functionalized to create more suitable nucleation sites for the precipitation of rhodium sulfide nano-particles resulting in a catalyst with smaller particle size, better particle distribution, and higher hydrogen oxidation and evolution reaction performance. XPS and FT-IR confirm that the dominant functional group on the carbon is the ketone group, which is more suitable group for rhodium sulfide particles formation than the carboxylic group. TEM and cyclic voltammetry results confirm that the catalysts with treated carbon have a smaller average particle size (7.2 nm vs. 13.2 nm) and higher mass-specific ECSA (21.8 $m^2/g-Rh$ vs. 9.1 $m^2/g-Rh$) than those with the untreated carbon. The H_2-Br_2 fuel cell test results show that the catalysts with functionalized carbon have better performance in the kinetic region but poorer performance in the mass transfer dominant region. The issue was identified to be due to the weak affinity of the ketone group on the carbon surface with the Nafion ionomer in the catalyst ink.

The mass-specific surface area of Rh_xS_y was further increased by the selection of a more effective nanoparticle growth mechanism. The diffusion-controlled nanoparticle growth mechanism was created by controlling the concentration of Rh_2S_3 monomer in the synthesis of rhodium sulfide catalyst, which decreases the average particle size from 13.2 nm to 3.2 nm by the TEM measurements. The mass-specific ECSA is improved from 9.1 $m^2/g-Rh$ to 43 $m^2/g-Rh$ with this approach. Moreover, the crystal phase composition in the mixed Rh_xS_y was modified by the usage of a new sulfur source, Na_2S, which results in an increase in the active area specific exchange current (0.59 A/cm^2 vs 0.51 A/cm^2). The mass-specific exchange current density increases from 0.58 $A/mg-Rh$ (Rh_xS_y/untreated carbon synthesized by the traditional sulfur source) to 2.8 $A/mg-Rh$ with the combination of the usage of functionalized carbon material, the diffusion-controlled of nanoparticle growth mechanism, and the new sulfur source.

The affinity issue between the ketone functional group on the carbon surface and the Nafion ionomer in the catalyst ink was resolved by using the Baeyer-Villiger reaction and ester hydrolysis to convert the Nafion-unfriendly ketone group to the Nafion-friendly carboxylic group. After the organic reactions, the modification of the surface functional group was validated by the FT-IR method. Furthermore, the TEM, XRD, and cyclic voltammetry methods confirm that the organic reactions have no negative effect on the catalyst and carbon surface in the process of organic reactions. The H_2-Br_2 fuel cell tests confirm that the mass transfer resistance observed in the fuel cell with the Rh_xS_y on the ketone-dominated pretreated carbon was significantly reduced by this approach. The discharge performance of hydrogen-bromine fuel cell with the Rh_xS_y/pretreated carbon with surface functional groups conversion is improved by 2.8 times compared to that of the fuel cell with the commercial Rh_xS_y catalyst.

Acknowledgements

First and foremost, I'd like to offer my sincerest thanks for my advisor, Dr. Nguyen. When coming to the KU, I was a young man who cannot speak fluent English, and know nothing about electrochemical engineering. The great patience of Dr. Nguyen helps me to be a qualified Ph.D. candidate hand by hand. His professional foundation and imaginative ideas always serve as an example of how to be a successful researcher for me.

Secondly, I'd like to thank the rest of my committee members, Dr. Laurence Weatherley, Dr. Kevin Leonard, Dr. Juan Bravo Suarez, and Dr. Xianglin Li for their valuable suggestions in my Ph.D. study.

Then I'd like to appreciate my fellow lab mates, Dr. Yarlagadda, Dr. Dowd, and Dhrubajit for their bits of help in my research.

Finally, I'd like to thank the support from my parents, my parents-in-law, my lovely daughter Lydia, and my charming wife Xian Li! I cannot finish the Ph.D. study without your contribution! My wife gave up her career in China and came to the U.S with me for my Ph.D. study. She is the most excellent wife and mom in the world. I also want to especially appreciate my daughter who wakes me up every early morning.

Contents

List of Figures

List of Tables

Nomenclature

CAES	Compressed air energy storage
CL	Catalyst layer
CV	Cyclic voltammetry
ECSA	Electrochemical surface area
EES	Electrical energy storage
EIS	Electrochemical impedance spectroscopy
FES	Flywheel energy storage
FT-IR	Fourier-transform infrared spectroscopy
GDE	Gas diffusion electrode
GDL	Gas diffusion layer
HER	Hydrogen reduction reaction
HOMO	Highest occupied molecular orbital
HOR	Hydrogen oxidation reaction
LUMO	Lowest unoccupied molecular orbital
MEA	Membrane electrode assemblies
MPL	Microporous layer
MWCNT	Multi-wall carbon nanotube

NPs	Nanoparticles
PEM	Proton exchange membrane
PHS	Pumped hydro storage
RFB	Redox flow battery
TEM	Transmission electron microscopy
TES	Thermal energy storage
XPS	X-ray photoelectron spectroscopy
XRD	X-ray diffraction

Chapter 1

Introduction

1.1 Background of Electrical Energy Storage (EES) Research

The research and usage of alternative energy are highly attractive topics worldwide as we face the challenges of the depletion of fossil fuel, environmental pollution, and global warming.[2,3] The percentage of wind and solar power in the total electricity generated has been steadily increasing. It is reported by U.S. Energy Information Administration that there are 6.3% and 1.3% of electricity generation from wind and solar source, respectively, in 2017. Compared to the electricity from conventional fossil fuel burning, however, the electrical energy from the new energies suffer from their intermittent and unpredictable natures.[4] It is still difficult to predict the wind speed and the level of sunshine accurately by now. The volatile and intermittent performances of new energy sources can impact the security and stability of the electrical grid when they are incorporated into the network on a large scale. Though people admire the benefits from the low-carbon future brought by the green energies, the electricity system must continue to be reliable. The lights must go on when the switch is flipped. There are three major types to address this challenge. One is to expand and diversify interconnections among grid resources. Building a national and reliable electric grid may balance the weather effect on the power generation of intermittent energy. When Boston is cloudy for the solar power, Miami may enjoy sunshine at the same time. The second strategy is to build smart grid which can predict and pinpoint real-time balancing concerns. The third and most important one is to develop the grid-scale storage technologies. The traditional power peaking technology may secure the stability of the network when the power from wind and solar contributes less 10% of the total electricity generation. When the percentage is higher than this threshold, the energy storage method is needed to stabilize the electrical network.[5]

Besides the benefits to the stability of the electrical network, electrical energy storage can also reduce the cost to users. In the electricity market, the price of electricity can vary even on the same day due to the changing intensity of supply and demand. The price difference between the peak and off-peak in the electric load curve determines the profits of energy storage. A typical electric load curve in Figure 1.1 shows that there is a morning ramp from 5 to 8 AM, an hourly-peak demand at 6 PM, and the load to the electric grid is low at the night hours. A cost-effective energy storage system can be used to store the cheap electricity at night and release it to the user at the stages of morning ramp and hourly peak demand to reduce the cost.

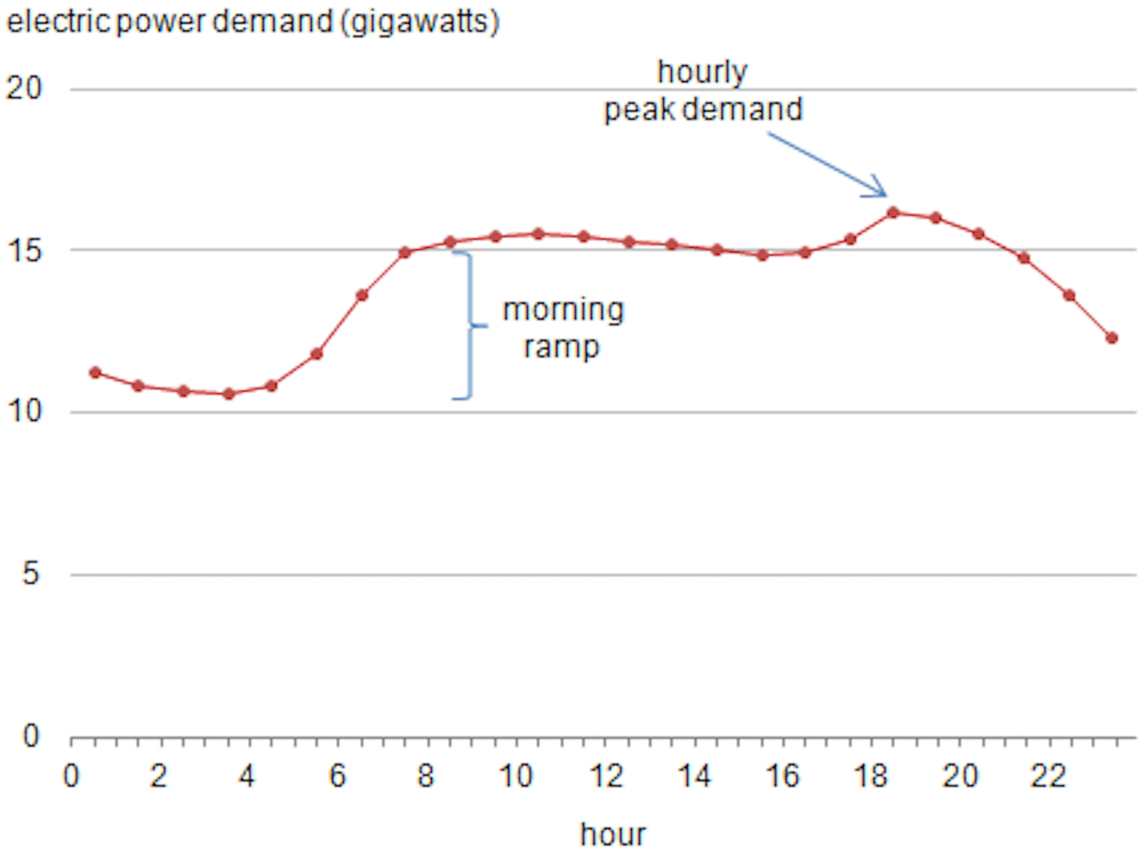

Figure 1.1. Electric load curve: New England of USA
(Source: U.S. Energy Information Administration based on data from Independent System Operator New England)

US energy storage market is no longer in its infancy and has been increasing rapidly and because of the necessity of developing clean energy and economic profits. The US installed energy storage systems with 1,080 cumulative megawatt-hours between 2013 and 2017, of which 27 % was added in 2017. It is estimated that the U.S. energy market will exceed $ 1.2 billion in 2019.[6]

1.2 Types of Electrical Energy Storage Systems

An electrical energy storage (EES) system stores electrical energy through a physical or chemical method and then outputs the electricity when it is needed by the users in the electrical network.

1.2.1 Mechanical Energy Storage Systems

The electricity can be stored in the various forms of mechanical energy ranging from potential energy to kinetic energy. Pumped hydro storage (PHS), compressed air energy storage (CAES), and flywheel energy storage (FES) are the typical examples of the mechanical energy storage systems.

The PHS is the oldest energy storage technology and still represents the most massive scale in the installation of energy storage system worldwide. It pumps the water back to the reservoir at the high level by using the cheap surplus off-peak electricity. When facing high electrical demand, the stored water can be released through turbines to generate electricity. The PHS station highly relies on the local landscape and can directly impact on the environment.[7]

The CAES compresses the air in large gas storage spaces like old oil or gas wells by using the off-peak electricity and then releases it to power turbines to generate electricity during the peak demand. The compression process creates heat while the thermal energy is released during the expansion stage. The efficiency of the CAES can be significantly improved if the heat can be stored and used during expansion. The first compressed air energy storage facility was the E.ON-Kraftwerk's 290MW plant built in Huntorf, Germany in 1978. CAES is the second largest form of energy storage just behind PHS.[8]

The electricity can be stored in a flywheel by using a motor to spin it to a very high speed and maintain it as the rotational energy. FES can output the electricity by using the flywheel to drive a generator. FES systems are made of high strength carbon–fiber rotors and magnetic bearings. The advantage of the FES is the fast speed to reach its energy capacity.[9]

1.2.2 Chemical Storage Systems

H_2 and synthetic natural gas (SNG) can be used to store electricity in the form of chemical energy. The source of H_2 comes from the electrolysis of water. If the desired product is SNG, H_2 can react with CO_2 via the Sabatier reaction.[10] Or the stored H_2 can be used in a H_2-O_2 fuel cell to generate electricity or directly combusted to release the thermal energy. The chemical storage systems have not been widely used on the commercial level due to a series of problems from the production, storage, distribution and usage (PSDU) of hydrogen. For example, the efficiency of the pathway from electricity$\rightarrow H_2 \rightarrow$electricity is only 34-44%. The research efforts on the chemical storage system are underway in the aspects of increasing the efficiency in the energy utilization and H_2 storage density.[11]

1.2.3 Electrical Methods

The supercapacitor (SC) and the superconducting magnetics are the two main technologies to store energy by electrical methods.

The capacitor consisting of two electrical conductors (plates) and a dielectric material in the middle stores the energy electrostatically. The energy is stored in an electrostatic field between the two plates. The potential difference across the two plates causes positive charges collected on one plate while the negative charges collected on another plate. After the capacitor is fully charged, there is no current flowing through the capacitor. When there is a demand in the electrical network, the stored electrical charges are released. The capacitors have been widely used in consumer electronics like laptop and cell phone to stabilize power supply. However, it is limited by the low energy density values for the large-scale energy storage. The supercapacitor is a new type of energy storage device like a hybrid of a traditional capacitor and a battery. It stores the energy through the fast adsorption/desorption of ion on the interface between electrode and electrolyte. Based on the mechanisms of energy storage and conversion, it can be divided into electric double layer capacitors (EDLC) and pseudocapacitors. EDLC is developed from the Helmholtz's double layer theory referring to two parallel layers of charges surrounding the solid particle, liquid droplet or gas bubble. The first layer of double-layer contains the ions (anion or cation) adsorbed onto the surface via chemical interaction, while the second layer consists of the ions with opposite charge attracted to the first-layer charge through Coulomb force. The separation of charge is achieved in the double layer rather than the two plates of the conventional capacitor. Thus the distance of charge separation is only 3-8 Å which is much smaller than the traditional capacitor. High surface area activated carbon material, or graphene are widely used as a carbon electrode for the EDLC. The pseudocapacitors are achieved by the fast Faradaic electron transfer with reversible redox reaction additional to the double layer capacity. The electrodes are often made with metal oxide and conducting polymer. Currently, the high cost, low energy density, and questionable cycle life limit the commercialization level of the supercapacitors.[12]

The superconducting magnet is one type of electromagnet made with the superconducting material. It stores the energy in the magnetic field generated by the current in the superconducting material of which temperature is lower than the superconducting critical temperature. The cost of superconducting material, the size required to store large-scale energy (100 miles loop for 1 GWh and extremely low critical temperature (at least 138 K) limit the commercialization of superconducting magnetics.[13]

1.2.4 Thermal Energy Storage

The thermal energy storage (TES) stores the thermal energy in the material with large heat capacity, which can be used in the heat engine cycles to generate electricity. TES can be divided into sensible heat storage (SHS), latent heat storage (LHS) and thermochemical heat storage (THS). The SHS uses the heat capacity of the material to store and release the thermal energy by increasing and decreasing the temperature of the material respectively. The cost of SHS is cheap due to the extensive sources of low cost materials like water, soil, and rock. The LHS involves the phase change process. The material used in the LHS transforms from solid to liquid phase for the discharge of energy, while the charge of energy changes the liquid phase to the solid phase. Compared to the LHS, the phase change material (PCM) has higher energy density. Molten salt is the typical PCM. A chemical bond can release the energy, while the forming of the bond absorbs energy. Then a reversible chemical reaction can be used for the thermal energy storage, named THS. It achieves the highest energy storage density compared to SHS and LHS. One example for the THS is the reaction between silica gel and water. TES has been widely commercialized, though the long response time limits its application in the power regulation of the electrical network.[14, 15]

1.3 Electrochemical Energy Storage System

Electrochemical energy storage systems are designed to convert the energy between electricity and chemical energy, which are featured with high energy densities and stable operating voltage. The sources of material that can be used in an electrochemical energy storage system are broad. Theoretically speaking, any materials with a difference in the Fermi level can be used to build an electrochemical energy storage device. By connecting an electrode to an external power supply, one can electrically control the electrochemical potential of electrons in the electrode, thereby driving reaction. The negative potential to the electrode increases the electron energy above the lowest unoccupied molecular orbital (LUMO) of electrolyte. Then the electron can be ejected into the electrolyte and reduce it to negatively charged species. On the other hand, the positive potential to the electrode decreases the electron energy below the highest occupied molecular orbital (HOMO) of electrolyte which makes the electrode be able to accept the electrons from the adjacent electrolyte. The controlled potential on the electrode determines the electrochemical reaction for the electrical energy storage and release.

The internal energy of electrode materials in the batteries is the chemical potential composed of ion energy, covalent bond energy, Van der Waals force, and hydrogen bond. At the standard conditions, every substance has its own Gibbs formation energy. The standard Gibbs free energy change ($\Delta_r G$) can be calculated for a electrochemical reaction (eq 1.1) by equation 1.2.

$$\alpha A + \beta B \longrightarrow \gamma C + \delta D \tag{1.1}$$

$$\Delta_r G = \gamma \Delta_f G_C + \delta \Delta_f G_D - \alpha \Delta_f G_A - \beta \Delta_f G_B \tag{1.2}$$

The Gibbs free energy can be expressed below:

$$\Delta G = \Delta U + P\Delta V + V\Delta P - T\Delta S - S\Delta T \tag{1.3}$$

where U is the internal energy, P is the pressure, V is the volume, S is the entropy and T is the temperature.

The heat (Q) and change of internal energy (ΔU) is,

$$Q = T\Delta S, \quad \Delta U = Q - W \tag{1.4}$$

Substitute the equation 1.4 into equation 1.3 to get the change of Gibbs free energy (ΔG),

$$\Delta G = -W + P\Delta V + V\Delta P - S\Delta T \tag{1.5}$$

For a constant pressure and constant temperature process,

$$\Delta G = -W \tag{1.6}$$

When the work refers to the electrical work only,

$$\Delta G = -QE = -nFE \tag{1.7}$$

where E is the voltage, Q is the electrical charge, F is the Faraday constant.

Combining with the definition of Gibbs free energy, the voltage can be calculated as,

$$E = -\Delta G_r / nF = -\sum \Delta G_{r,i} / nF \tag{1.8}$$

The Gibbs free energy of formation is usually referred in the manual of thermodynamics which is measured for the bulk material. In the system of electrochemical reaction, the Gibbs free energy of formation may deviate from the ideal and bulk material. The Gibbs free energy of material used in the electrochemical reaction is supposed to include the contribution from the defect of material to get the accurate estimation.

$$\Delta G_{F,i} = \Delta G_{F,i}(bulk) + \Delta G_{F,i}(defect) \tag{1.9}$$

Even when the chemical formula of the reactants and products in the charging/discharging process is same, the open circuit voltage of charging/discharging may be different due to the irreversible change of material structures. This phenomenon is named voltage hysteresis by thermodynamics.

In the process of electrochemical energy storage method, the electron and ion are ejected or adsorbed to the interface of electrode/electrolyte. It may be accomplished via several possible mechanisms like intercalation reaction, phase transition, conversion reaction, reversible chemical bonding, surface charging, free radical mechanism, underpotential deposition, and interfacial charging. Through those mechanisms of electron ejection and ion adsorption/desorption, the electrical energy can be converted into the chemical energy or reverse.

The electrochemical reactions are thermodynamically reversible. However, some of the reverse reactions are kinetically impossible. Then the electrochemical systems can be divided into the primary battery which cannot be charged and a secondary battery which is chargeable. The secondary battery is preferable for the application of the energy storage system.

Figure 1.2 shows several energy storage systems regarding power rating, which identifies potential applications, and duration of discharge. It can be seen that the electrochemical energy storage systems have a wide range in the system power size and discharge time, which facilitates their

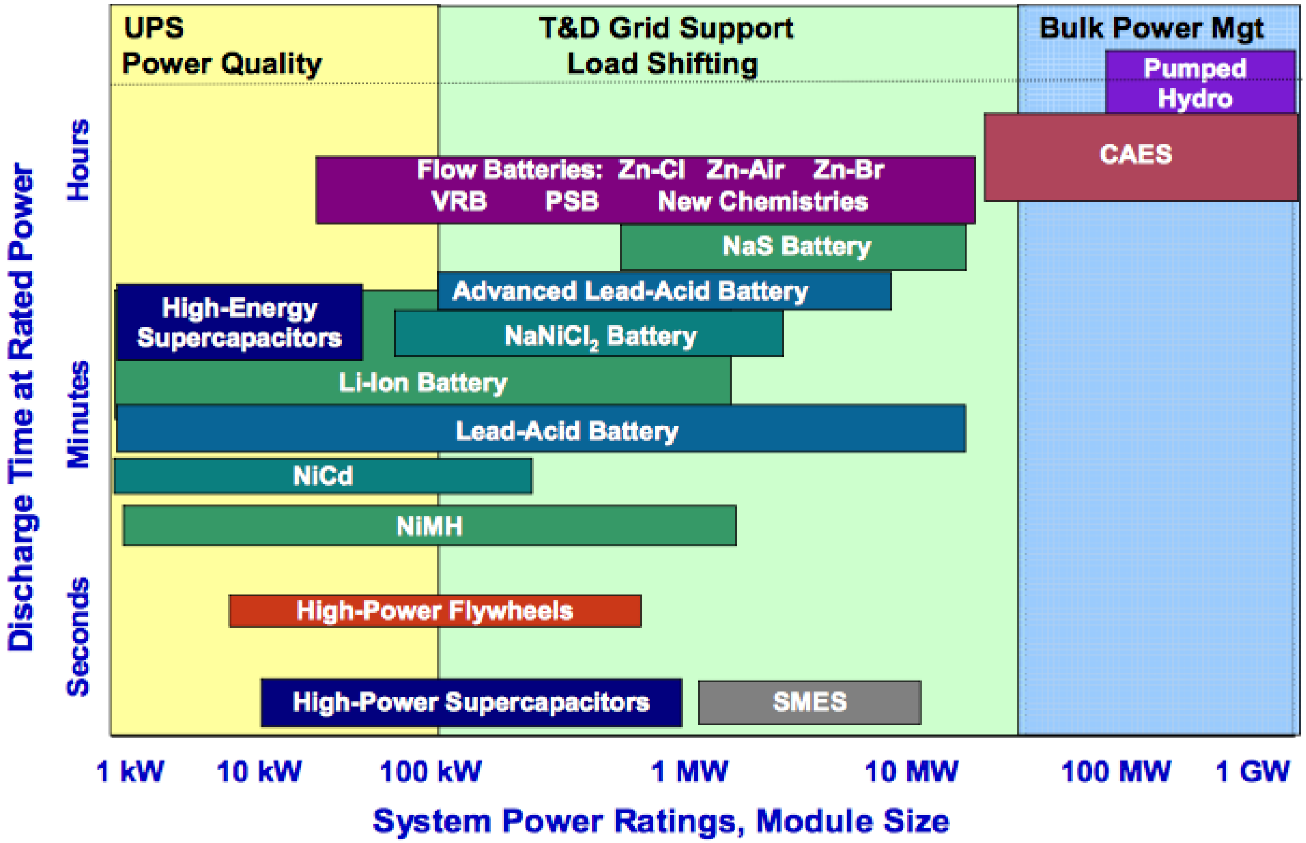

Figure 1.2. Comparison of discharge time and power rating for various electrical energy storage systems. Reprinted from courtesy of Electric Power Research Institute (EPRI), Palo Alto, CA 94304, USA.

extensive applications. The representative systems of electrochemical storage will be introduced in the following sessions.

1.3.1 Li-ion Batteries

Li-ion batteries store the electrical energy in the electrodes made of Li-intercalation compounds. The Li^+ ions transfer between the positive and the negative electrode during charge and discharge. The energy is released and stored with concomitant oxidation and reduction processes occurring at the two electrodes. There is an electrolyte for the ions transportation, which can be a liquid, a gel, or a solid polymer. The majority type of electrolyte in the Li-ion batteries is the liquid electrolytes made of organic alkyl carbonate solvents and lithium salt such as $LiPF_6$, $LiBF_4$, and $Li[PF_3(C_2F_5)_3]$(LiFAP). To stabilize the electrolyte/electrode interface, a varieties of additives like vinylene carbonate are added to the electrolyte.[16] The typical electrochemical redox reactions in the Li-ion batteries are shown below,

$$\begin{aligned} Anode: \mathrm{Li}_x\mathrm{C}_6 &\xrightarrow{\text{discharge}} x\mathrm{Li}^+ + xe^- + \mathrm{C}_6, \quad E = -2.84\ V\ vs.\ RHE \\ Cathode: \mathrm{Li}_{1-x}\mathrm{CoO}_2 + x\mathrm{Li}^+ + xe^- &\xrightarrow{\text{discharge}} \mathrm{LiCoO}_2, \quad E = 0.76\ V\ vs.\ RHE \\ Cell\ reaction: \mathrm{LiC}_6 + \mathrm{CoO}_2 &\xrightarrow{\text{discharge}} \mathrm{C}_6 + \mathrm{LiCoO}_2, \quad E = 3.6\ V\ vs.\ RHE \end{aligned} \tag{1.10}$$

The voltage of Li-ion cells is 3.6V. Its capability and power are about 150 Ah/kg and over 200 Wh/kg, respectively. The usage of the flammable organic electrolyte is a risk of heat generation, especially in the scale-up applications. The whole lithium-ion battery system has to be managed carefully to avoid the overcharge, a condition where the applied potential is higher than the safe potential of the organic electrolyte. The lithiated-graphite electrode may result in Li-dendrite growth and potential electrical shoring due to the operation voltage of batteries is close to that of metallic lithium. The cost of Li-ion is also a concern in the large-scale energy storage system.[17]

1.3.2 Sodium-sulfur Batteries

Sodium-sulfur batteries attract the research interest due to the abundant resources and low cost of elements got involved. Due to the sensitivity to O_2 and H_2O, the sodium anode is separated from cathode by a Na^+ conducting solid state membrane. The widely used membrane in the Na-S batteries is $\beta'' - Al_2O_3$ which demonstrates a high conductivity of Na^+. To enhance the conductivity, Na-S batteries operate at the elevated temperature, 300-350°C.[18] The electrochemical redox reactions involved in the Na-S batteries are shown below,

$$\begin{aligned} Anode: 2\mathrm{Na} &\xrightarrow{\text{discharge}} 2e^- + 2\mathrm{Na}^+, \quad E = -0.271\ V\ vs.\ RHE \\ Cathode: x\mathrm{S} + 2\mathrm{Na}^+ + 2e^- &\xrightarrow{\text{discharge}} \mathrm{Na_2S}_x \quad E = 1.509 - 1.937\ V\ vs.\ RHE \\ Cell\ reaction: 2\mathrm{Na} + x\mathrm{S} &\xrightarrow{\text{discharge}} \mathrm{Na_2S}_x \quad E = 1.78 - 2.208\ V\ vs.\ RHE \end{aligned} \tag{1.11}$$

The anode sodium is in a molten state during battery operation. It can offer a voltage of 1.78-2.208V at 350°C. Ford company developed it in the late 1960s and 1970s for electric vehicle applications.[19] The high operating temperature in the Na-S batteries may reduce the material durability and increase the complexity of thermal management. The future R&D of Na-S batteries will focus on the optimization of solid oxide membrane for the low operating temperature and the use of a more cost-effective material.[20]

1.3.3 Lead-carbon Batteries

The lead-acid battery was first invented in 1859 by the French physicist Gaston Plante. It is viewed as the first type of rechargeable battery. The low cost and the high current capacity of the lead-acid battery makes it attractive for use in vehicles though the energy-to-weight ratio is low. The redox reaction between PbO_2 and Pb is used to store the energy.[21]

$$\begin{aligned} Anode: \mathrm{Pb} + \mathrm{SO_4}^{2-} &\xrightarrow{\text{discharge}} \mathrm{PbSO_4} + 2e^-, \quad E = -0.359\ V\ vs.\ RHE \\ Cathode: \mathrm{PbO_2} + 4\mathrm{H}^+ + 2e^- + \mathrm{SO_4}^{2-} &\xrightarrow{\text{discharge}} \mathrm{PbSO_4} + 2\mathrm{H_2O}, \quad E = 1.691\ V\ vs.\ RHE \\ Cell\ reaction: \mathrm{Pb} + \mathrm{PbO_2} + 2\mathrm{H_2SO_4} &\xrightarrow{\text{discharge}} 2\mathrm{PbSO_4} + 2\mathrm{H_2O}, \quad E = 2.05\ V\ vs.\ RHE \end{aligned} \tag{1.12}$$

The cell offers 2.05V as the standard voltage. Full or partial replacement of lead by carbon material in the negative electrode is one way to improve the cycle-life and energy-to-weight ratio of lead-acid further. The major difference in the lead-carbon battery is that the high-surface-area carbon electrode does not undergo any chemical reaction. The storage process in the negative electrode is accomplished by two parts, 1) double-layer (nonfaradic) storage, 2) H^+ pseudocapacitance (faradic) storage.[22] The second part is shown below,

$$nC_6{}^{x-}(H^+)_x \xrightarrow{\text{discharge}} nC_6{}^{(x-2)-}(H^+)_{x-2} + 2H^+ + 2e^-, \quad E = -0.309\ V\ vs.\ RHE \tag{1.13}$$

The H^+ which is stored in the negative carbon electrode in the fully charged state migrates to the positive electrode during the discharge. Then the cycle life of a battery can be prolonged by eliminating nucleation and growth of $PbSO_4$ in the negative electrode during the discharge. In the large-scale application for energy storage, the slow ramp rate may fail to respond to the fast change of the wind or solar renewable energy.

1.3.4 Redox Flow Batteries

A schematic diagram of a redox flow battery (RFB) is shown in Figure 1.3.[23] The energy is stored as chemical potential in the two electrolyte tanks. The energy conversion happens on the electrode surface of the RFB. Liquid electrolytes are pumped from storage tanks to the electrode surface where the chemical energy is converted to electrical energy for the discharge or vice versa. The obvious difference of the RFB toward the traditional batteries is the energy storage site. The RFB stores the energy in the electrolyte tanks, while traditional batteries store energy in the electrode materials. Then the power of the system is determined by the total area size of the electrode surface while the concentration and volume of electrolyte decide the energy storage capacity. The advantage of redox flow batteries over lithium battery is its long durability, while its disadvantage is the low energy density due to the low solubility of reactive species in the water. It provides great flexibility to adjust the power and storage capability. As shown in Figure 1.2, the range of energy capability of RFB is vast, from hours to days.

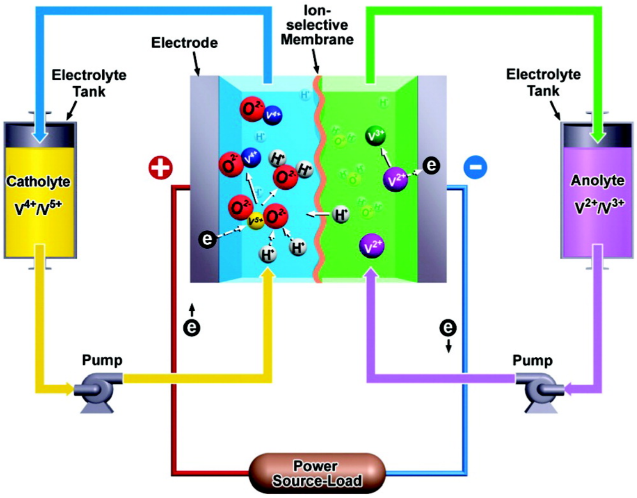

Figure 1.3. Schematic of an all vanadium redox flow battery as an example of RFB

1.3.4.1 Vanadium flow batteries

The four different oxidation states of vanadium make it possible to form two couples of redox species in the positive/negative electrodes respectively. Since the vanadium is the only active element in the two electrodes, the cross-contamination of anolyte and catholyte in vanadium flow batteries (VRB) is easy to be recovered compared to other types of RFB.[24] The energy conversion is accomplished via the valence state change of vanadium via the following electrochemical redox reactions,

$$\begin{aligned} Anode: \mathrm{V}^{2+} &\xrightarrow{\text{discharge}} \mathrm{V}^{3+} + e^-, \quad E = -0.255\ V\ vs.\ RHE \\ Cathode: \mathrm{VO_2}^{+} + 2\mathrm{H}^+ + e^- &\xrightarrow{\text{discharge}} \mathrm{VO}^{2+} + \mathrm{H_2O}, \quad E = 0.991\ V\ vs.\ RHE \\ Cell\ reaction: \mathrm{VO_2}^{+} + 2\mathrm{H}^+ + \mathrm{V}^{2+} &\xrightarrow{\text{discharge}} \mathrm{VO}^{2+} + \mathrm{V}^{3+}, \quad E = 1.246\ V\ vs.\ RHE \end{aligned} \tag{1.14}$$

The vanadium electrochemical redox reactions can offer a cell voltage of 1.246V at room temperature. As mentioned in the Figure 1.3, the anolyte is a solution of V(III)/V(II) while the catholyte is composed of a solution of V(V)/V(IV). H_2SO_4 is the most commonly used supporting electrolyte for both electrodes. The concentration of vanadium species determines the energy density of VRBs. The higher the concentration is, the higher is the energy capacity. The concentration of vanadium, however, is limited by the precipitation of solid vanadium oxide phases. V_2O_5 precipitation is formed when the concentration is larger than 2M above 40°C. The research on extending the solubility range of vanadium ions in the electrolyte is an active area.

1.3.4.2 Zn-Br flow batteries

The zinc-bromine flow battery is type of hybrid flow battery which has a stationary battery electrode and a flow battery electrode.[25] A solution of zinc bromide is stored in two separate tanks shown in Figure 1.4. Bromide is converted to bromine at the positive electrode while the zinc cation is deposited as metallic zinc on the negative electrode surface during charge. The reactions are listed below,

$$\begin{aligned} Anode: \mathrm{Zn} &\xrightarrow{\text{discharge}} \mathrm{Zn}^{2+} + 2e^-, \quad E = -0.762\ V\ vs.\ RHE \\ Cathode: \mathrm{Br}_2(aq) + 2e^- &\xrightarrow{\text{discharge}} 2\mathrm{Br}^-, \quad E = 1.09\ V\ vs.\ RHE \\ Cell\ reaction: \mathrm{Zn} + \mathrm{Br}_2(aq) &\xrightarrow{\text{discharge}} 2\mathrm{Br}^- + \mathrm{Zn}^{2+}, \quad E = 1.85\ V\ vs.\ RHE \end{aligned} \tag{1.15}$$

This cell can provide 1.85V as the standard voltage. Due to the metallic zinc generated in the charging process, there is a need for the full discharge every few days to prevent zinc dendrites that can puncture the separator. It is a waste of electricity stored in the RFB.

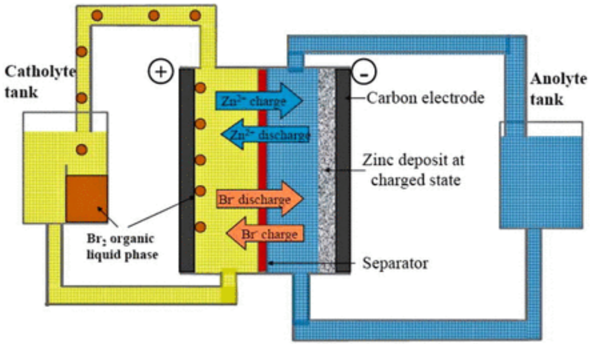

Figure 1.4. Schematic of Zinc-Bromine Flow Battery[1]
Figure reproduced with kind permission from Woodhead Publishing Limited, Cambridge, UK.

1.4 Hydrogen-Bromine Fuel Cell

1.4.1 Introduction of Hydrogen-Bromine Fuel Cell

H_2-Br_2 fuel cell is also a type of electrochemical energy storage system. Since it is the main topic of this dissertation, it is introduced in a single section. After the invention in 1964,[26] it attracts extensive interests from the industry and academic institutions due to the fast kinetics and low-cost energy storage materials.[27,28,29,30] The hydrogen-bromine fuel cell is composed of a H_2 electrode, a Br_2 electrode, and a proton exchange membrane (PEM) as the electrolyte, which is shown in Figure 1.5. The starting material in H_2-Br_2 fuel cell is HBr, which is fed from a external tank to the bromine (positive) side of the fuel cell and oxidized to bromine by the electricity from an intermittent energy source. The H^+ cations in the HBr solution migrate across the PEM to the negative electrode and are then oxidized to H_2 which is stored externally in a tank. When there is a demand for electricity, the fuel cell is discharged to release energy. The bromine-rich solution and hydrogen gas are fed back to the positive and negative electrode respectively for the discharging reaction. The bromine is reduced to bromide while the hydrogen is oxidized to hydronium ion which migrates back to the negative electrode via the PEM to form HBr again. The low price of the starting material, HBr is viewed as a huge advantage of the H_2-Br_2 fuel cell. Currently, the bulk price of HBr is only \$0.8/lb which is 4% of the price of vanadium (\$18.4/lb). The cheap source of energy storage material makes the hydrogen-bromine fuel cell a cost-effective one. The fast kinetics of the bromine/bromide reaction is another advantage of this type of fuel cell, which will be introduced in the section of 1.4.2.1. The hydrogen-bromine fuel cell is a type of hybrid fuel cell which has a gaseous phase negative electrode and a liquid phase positive electrode. Since the cross-contamination may be unavoidable, the separation of gas from the liquid is much easier compared to the mixture of two liquid phases. The electrochemical reactions in a hydrogen-bromine fuel cell are listed below,

$$\begin{aligned} Anode: \mathrm{H_2} &\xrightarrow{\text{discharge}} 2\mathrm{H^+} + 2e^-, \quad E = 0\ V\ vs.\ RHE \\ Cathode: \mathrm{Br_2} + 2e^- &\xrightarrow{\text{discharge}} 2\mathrm{Br^-}, \quad E = 1.09\ V\ vs.\ RHE \\ Cell\ reaction: \mathrm{H_2} + \mathrm{Br_2} &\xrightarrow{\text{discharge}} 2\mathrm{H^+} + 2\mathrm{Br^-}, \quad E = 1.09\ V\ vs.\ RHE \end{aligned} \tag{1.16}$$

The fuel cell can provide 1.09V as the standard potential.

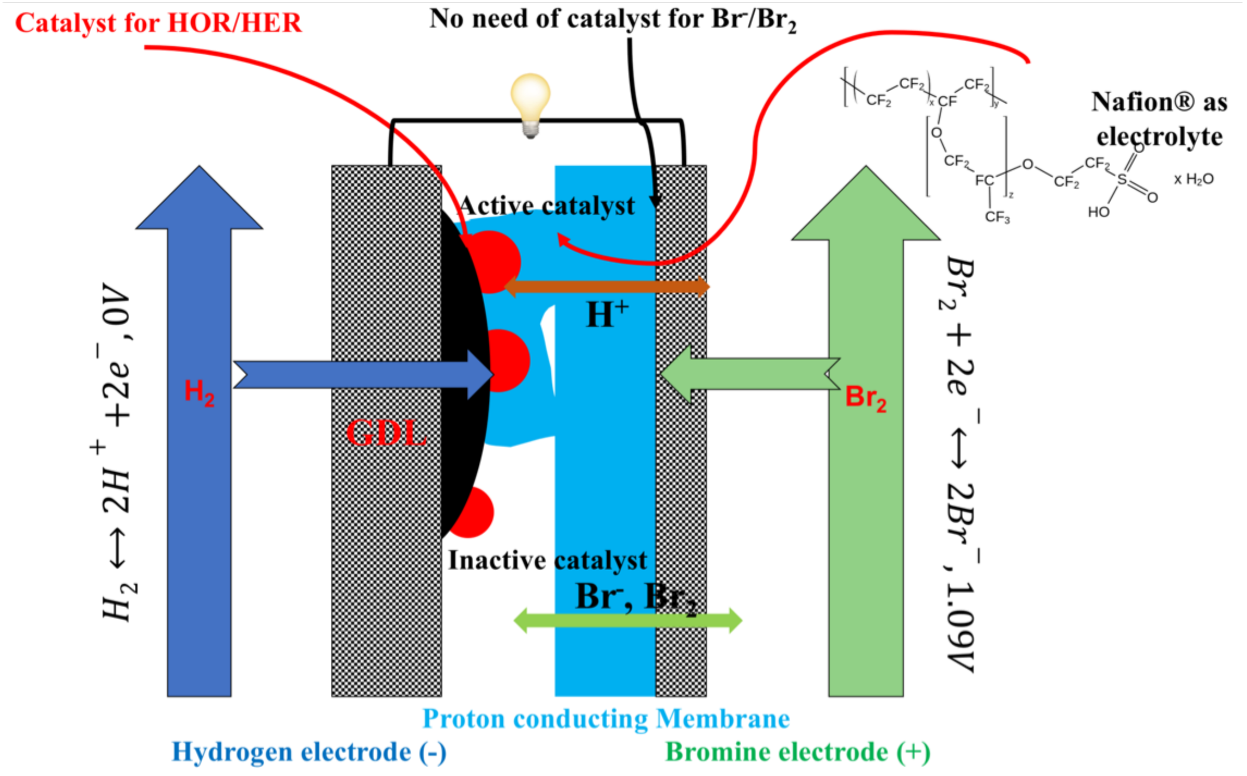

Figure 1.5. Schematic diagram of H_2-Br_2 fuel cell

1.4.2 Components in the Hydrogen-Bromine Fuel Cell

1.4.2.1 Electrode

There are two electrodes in the H_2-Br_2 fuel cell, the positive electrode for the bromine/bromide reaction and the negative electrode for the hydrogen/hydronium reaction. The hydrogen electrode in the hybrid H_2-Br_2 fuel cell is similar with that of the H_2-O_2 PEM fuel cell. The high-surface-area carbon supported catalyst like Pt/C is used to catalyze the hydrogen oxidation reaction (HOR) and hydrogen evolution reaction (HER). The catalyst is mixed with Nafion ionomer and solvent (DI water and isopropyl alcohol) to prepare the catalyst ink, which is then coated onto the microporous layer (MPL) of a bi-layer carbon gas diffusion material to form a gas diffusion electrode (GDE). The hydrogen gas diffuses from the flow field to the catalyst layer of GDE where the HOR/HER can be catalyzed to generate/consume electrons. The hydronium ions can leave and come to the surface of the catalyst via the ion channel, Nafion ionomer.[31] The GDE is further hot pressed onto a proton exchange membrane to provide continuous H^+ pathway between the catalyst layer of hydrogen electrode and the membrane. While a catalyst like Pt is required on the hydrogen electrode for HOR/HER catalysis, the bromine/bromide reaction on the positive electrode only needs carbon material to provide reaction sites since the exchange current density of Br^-/Br_2 on carbon is quite decent even without any catalyst.[32,33] The specific surface area of carbon paper as a positive electrode determines the number of active sites for the redox reaction between Br^-/Br_2. Great progress to increase the specific surface area of carbon paper as a positive electrode of H_2-Br_2 fuel cell has been made in Dr. Nguyen's research group.

1.4.2.2 Membrane

The hydrogen electrode and the bromine electrode are separated by a proton exchange membrane which is also used in the H_2-O_2 fuel cell. The most commonly used proton exchange membrane is Nafion first discovered in the late 1960s by DuPont. The chemical structure of Nafion can be found in Figure 1.5. Nafion's capability to transport protons is a result of the sulfonate groups

(−SO_3H) attached to a tetrafluoroethylene (Teflon) backbone. The protons can 'hop' from one acid site of sulfonate group to another. Theoretically speaking, the anions are excluded in the proton exchange membrane while some neutral and non-H^+ cations may transfer via the ion channels in Nafion.[34] In practice, it is found that bromide anion and bromine can penetrate the Nafion membrane to cross-contaminate the hydrogen electrode.[35] The Nafion membrane can be free of almost all chemical attacks, which makes it an appropriate component for the application in the corrosive Br^-/Br_2 environment.

The membrane and two electrodes are assembled as the core component of a fuel cell, membrane electrode assemblies (MEA), which is shown can in Figure 1.6. The hydrogen electrode and the bromine electrode are hot pressed on the membrane.

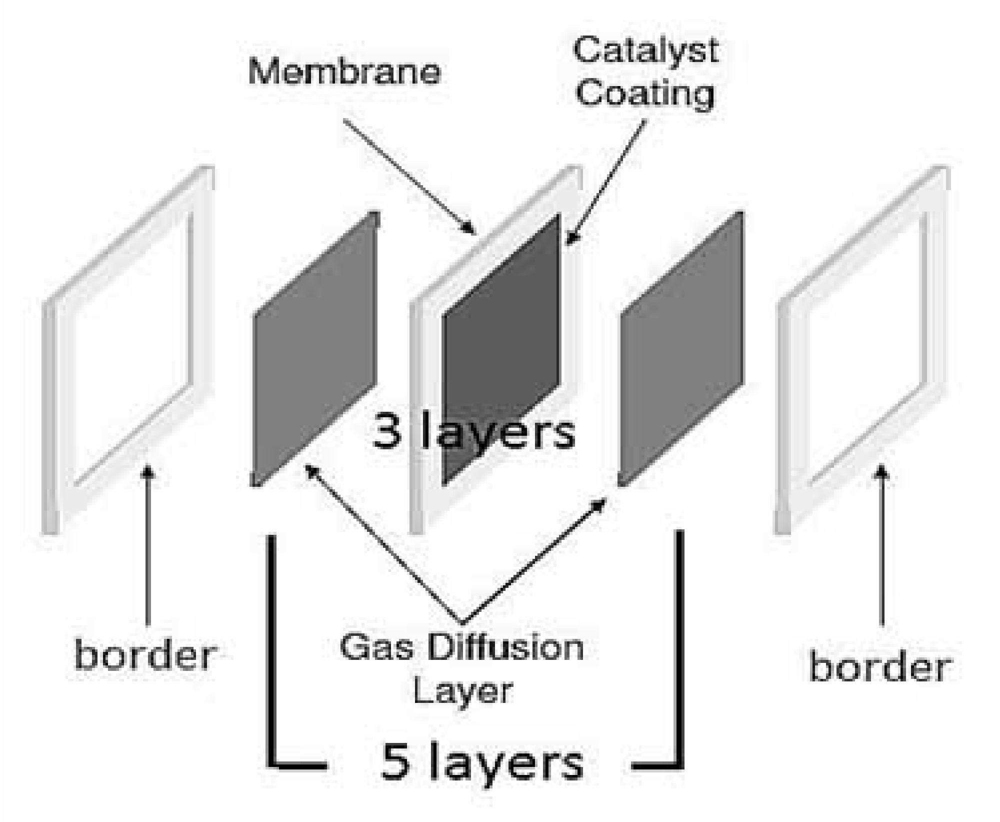

Figure 1.6. Schematic structure of MEA (Reprinted from Courtesy of Lilium Energy)

1.4.2.3 Bipolar plate

A significant part of a fuel cell stack is the bipolar plates which account for about 80% of the weight and 45% of stack cost.[36] It is designed for the multiple purpose including uniform distribution of reactants on the MEA, collection of current from the electrodes, and prevention of leakage of reactants. The plates must be cost-effective, lightweight and easily manufactured. The materials investigated so far for the bipolar plates are graphite, metals including coated/non-coated, and composites such as polymer-carbon/polymer-metal. In the early-stage of development of H_2-O_2 fuel cell, the graphite bipolar plates were used due to the chemical stability at the high voltage. However, the gaseous hydrogen and oxygen may leak through porous structure of graphite plates, which requires the graphite plates to be very thick. Then the gold-coated metal plates are used to reduce the weight and thickness of flow field. The gold is stable at the high voltage and liquid water environment. In the application of hydrogen-bromine fuel cell, tantalum and niobium are the only two materials that can withstand the corrosive Br_2 environment. In the future, the graphite or cheap metal coated by a thin layer of tantalum or niobium may be a choice as the bipolar plate for H_2-Br_2 fuel cell.

The flow fields carved on the bipolar plates are designed to provide an adequate amount of the reactants (hydrogen and HBr/Br_2) to the gas diffusion layer (GDL) and catalyst surface while minimizing pressure drop.[37] Serpentine, parallel and interdigitated flow are the most popular flow field configurations. Among those flow fields, interdigitated flow field design promotes forced convection while other designs only rely on the diffusion from the flow channel to the GDL.[38] The flow channels of the interdigitated flow field are not continuous from the plate inlet to the plate outlet. The dead-ended flow channels force the reactant flow to convect to the catalyst layer (CL) under pressure. All of the flow fields used in this dissertation are interdigitated ones because it can outperform conventional flow field designs in the transportation and distribution of reactants.

1.5 Electrocatalyst Research in the Hydrogen-Bromine Fuel Cell

Electrocatalyst for the HOR/HER on the hydrogen electrode (negative electrode) is the primary focus of this dissertation, and also viewed as the core problem in developing and commercializing H_2-Br_2 fuel cell.

1.5.1 Requirements for the Electrocatalyst in the Hydrogen-Bromine Fuel Cell

Carbon electrode without catalyst can be used for the bromine reaction at the positive electrode, while the hydrogen oxidation reaction (HOR) and hydrogen evolution reaction (HER) at the negative electrode require a catalyst. Though the membrane used in the fuel cell is called proton exchange membrane, the Br^- anion and the bromine still can penetrate the Nafion membrane in practice. The Br^-/Br_2 have been proved to be corrosive to the pure metal materials. Then the primary consideration to the electrocatalyst on the hydrogen electrode is its stability in the corrosive environment. In an isolated environment like a three-electrode system with an aqueous electrolyte, more catalysts can provide better catalysis performance. In the fuel cell, however, the thicker catalyst layer can result in the higher mass transfer resistance since the gaseous reactant, H_2, has to diffuse to the catalyst sites in the electrode for the HOR/HER.[39] To reduce the mass transfer resistance of H_2 and ion transport resistance of H^+ in the catalyst layer (CL) and provide more active sites for the HOR/HER catalysis, the catalyst nanoparticles on the carbon surface are supposed to have high mass-specific surface area and highly active crystal structure for catalysis. In a fuel cell, HOR/HER only occur on the catalyst surface covered by Nafion ionomer which provides the ionic transportation channel as shown in Figure 1.5. The Nafion ionomer on the catalyst layer connects the catalyst sites and the fuel cell electrolyte membrane, which transfer the proton from/to the catalyst surface to/from the positive electrode during discharge/charge reactions. Without coverage of Nafion ionomer, the H^+ cannot go to or leave from the catalyst surface at a sufficiently high rate for high power output. HER and HOR are not able to be accomplished without the supply and the remove of H^+ respectively.[40] Thus, it can be concluded that the average catalyst particle size determines the mass-specific surface area of the catalyst, while the distribution of ionomer on the carbon surface decides the effective area that can catalyze HOR/HER in the fuel cell. The requirements for the electrocatalyst in the H_2-Br_2 can be summarized below:

1. Stability in the HBr/Br_2 solution
2. High mass specific surface area
3. High activity of HOR/HER catalysis
4. High electrolyte-covered catalyst area

Due to the usage of the noble metal as the catalyst in the H_2-Br_2 fuel cell, the cost of electrocatalyst attracts intensive concerns from the public and the industry. The cost of electrocatalyst in the whole H_2-Br_2 fuel cell, however, only accounts for 3% of the fuel cell cost, while the bipolar plates contribute 45% and the membrane contributes 21%.[41] So, the cost of the catalyst is a smaller issue than its effectiveness.

1.5.2 Current Electrocatalyst and Its Problems

The commonly used HOR/HER catalyst, platinum, is highly susceptible to corrosion by bromine/bromide crossed over from the positive electrode. Based on our previous studies, the rhodium sulfide is a promising catalyst candidate for the HOR/HER in the corrosive environment since it has the acceptable activity for the HOR/HER and excellent stability in the HBr/Br_2 solution. There are three types of rhodium sulfide crystal phases, shown in Figure 1.7(a) (replotted from Mukerjee et al.[42]), Rh_2S_3, Rh_3S_4 and $Rh_{17}S_{15}$. Among these crystal structures, Rh_2S_3 is not active while Rh_3S_4 and $Rh_{17}S_{15}$ are active phases for catalysis of HOR/HER. The conversion from Rh_2S_3 to Rh_3S_4 and $Rh_{17}S_{15}$ is by thermal reduction to release some sulfur from Rh_2S_3 as shown in Figure 1.7(b).[43]

In the crystal structures of Rh_xS_y, it can be seen that there are two major types of Rh atoms, rhodium atoms bonded with neighboring Rh, and rhodium atoms coordinated with neighboring

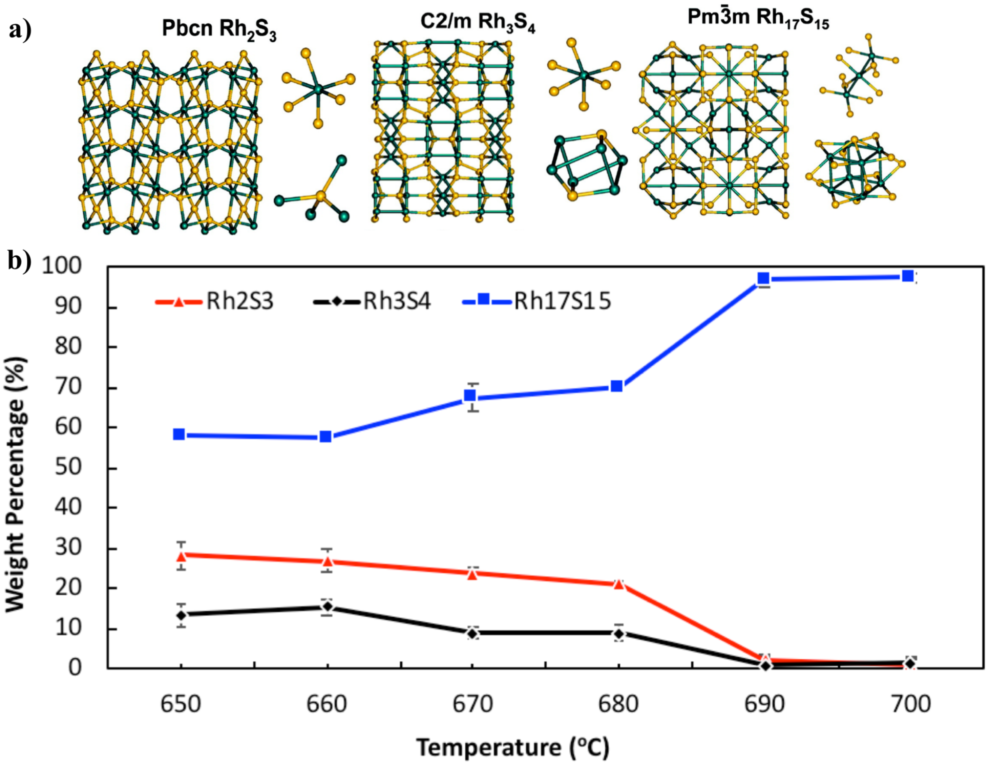

Figure 1.7. Crystal structures(a) and temperature-phase composition (b) of rhodium sulfide

S. The active centers of Rh_xS_y for the HOR catalysis is Rh with neighboring Rh which shows the metallic property. Besides the Rh centers, the sulfur sites can also be used to catalyze HER. Consequently the Rh_xS_y can be viewed as a bi-functional catalyst with better HER catalysis capability. Based on the density functional theory (DFT) calculation, the highest activity for the catalysis of HOR/HER is achieved by Rh_3S_4.[44] The reasons may be due to the different Rh-Rh bond energies in different crystal structures. The Rh-Rh bond length of metallic Rh, Rh_2S_3, Rh_3S_4 and $Rh_{17}S_{15}$ is 2.731, 3.208, 2.730, and 2.635 Å respectively.[45] The Rh-Rh bond length of Rh_3S_4 is closest to that of metallic Rh, which indicates that the HOR-active Rh center of Rh_3S_4 has most similar electronic density with that of metallic Rh. The $Rh_{17}S_{15}$ shows stronger Rh-Rh bond with shorter length due to the $Pm\bar{3}m$ group of a crystal structure. Based on the Hammer-Norskov model,[46] the electron density of active sites should be appropriate for the adsorption and desorption of reactant and product. The higher electron density of Rh center in $Rh_{17}S_{15}$ may be preferable for the adsorption of H^+ and subsequent catalysis of the HOR. However, the desorption of product, H_2, may be obstructed by the extra electron density in Rh center of $Rh_{17}S_{15}$.

In sum, the current catalyst suffers from two main drawbacks, the low mass-specific surface area, and activity crystal phase. The low mass-specific surface area is due to the large average particle size and poor distribution of particles on the supporting carbon, while the low activity crystal phase mainly comes from the lack of active crystal structure Rh_3S_4.

1.5.3 Characterizations in the Research of Electrocatalyst

A series of techniques including physical and electrochemical ones are used to characterize electrocatalysts in the research. The physical characterization technologies like transmission electron microscopy (TEM), X-ray diffraction (XRD), X-ray photoelectron spectroscopy (XPS), and Fourier Transform Infrared Spectroscopy (FT-IR) are used in the determination of the morphology, size, crystal structure, composition of nanoparticles, and the types of functional groups of supporting carbon materials. Electrochemical characterizations including cyclic voltammetry, multiple-step chronoamperometry, electrochemical impedance spectroscopy (EIS), and fuel cell polarization curve measurement can directly show the electrochemical performances of the catalyst.

1.5.4 Electrocatalyst Performance in the Fuel Cell

The Gibbs free energy of an electrochemical reaction (ΔG_r) determines the equilibrium voltage of the reaction, which is the maximum voltage a battery can output. If there is a current generated, the voltage has to be reduced to overcome the energy barrier to make the electrochemical reaction happen. The most common method to evaluate the electrocatalyst performance in the fuel cell is the measurement of the polarization curve. The polarization curve reveals the relationship between the voltage and current density. By slowly 'stepping up' or 'stepping down' the voltage on the potentiostat, the current response of the fuel cell can be determined. Alternatively, the current density is controlled, and the voltage output is measured.

There are three distinct regions of a fuel cell polarization curve, 1) activation loss region at the low current density, 2) ohmic loss region at the medium current density, and 3) mass transfer controlled region at the high current density. A typical polarization curve is shown as Figure 1.8.

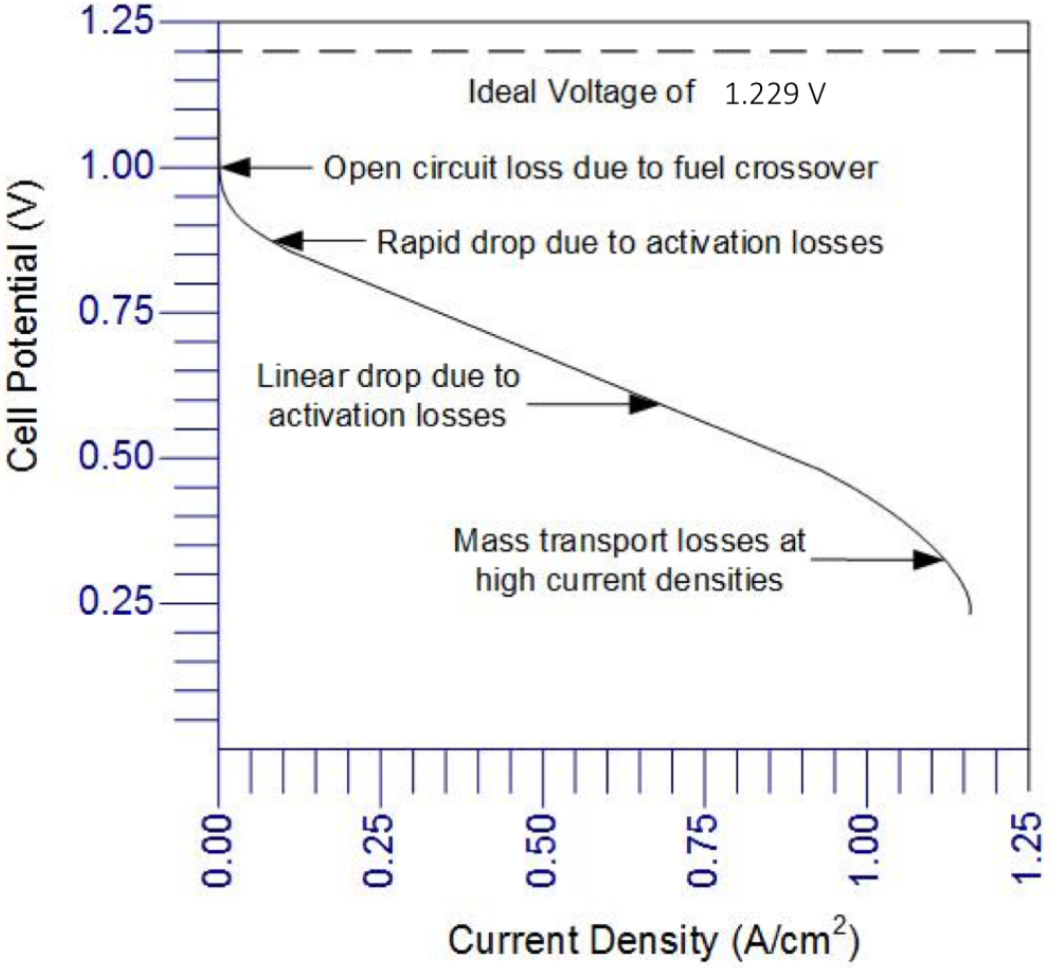

Figure 1.8. Typical example of polarization curve for the H_2-O_2 PEM fuel cell

Similar to the energy barrier in a chemical reaction, the activation energy of the electrochemical reaction is overcomed by a voltage loss. Also, the more active sites of a catalyst can provide, the smaller voltage loss is required to generate a given temperature. The ohmic resistance always exists. It comes from the electrical resistance in the cell and the ionic transportation resistance of the membrane. The mass transfer loss region reveals the effect of mass transport on the voltage loss in the cell. A fuel cell must be supplied continuously with fuel and oxidant to produce electricity. Products must also be continually removed to maximize fuel cell efficiency. If the fuel cell has a higher resistance of mass transport to/from the electrode surface, the overpotential (voltage loss) in the mass-transfer-controlled region at the same current density will be more significant.

1.6 Roadmap to Solve the Current Problems in the Electrocatalyst Research

As mentioned in Section 1.5.2, there are two main drawbacks for the current electrocatalyst of HOR/HER, low mass-specific surface area and lack of active crystal phase. A roadmap was designed and applied to develop electrocatalyst with high mass-specific surface area, highly active crystal phase, and high Nafion affinity in the catalyst layer. The whole roadmap is summarized in the Figure 1.9.

The core-shell structure was first proposed to improve the mass-specific surface area. A cheap metal can be used as the core material, while a thin shell of Rh_xS_y is loaded on the core material to reduce the amount of expensive rhodium material. In the preliminary research, Pt/C commercial product with well distributed and small nanoparticle size was used to verify the concept. It is found that not all of the Rh_xS_y shells are complete. The exposed Pt or other cheap metal core can be corroded by the corrosive solution, which finally results in the disappearance of the core-shell structure. When the cheap metal cores like nickel and cobalt were tried to replace the expensive Pt core material, they are dissolved in the acidic $RhCl_3$ solution which makes the formation of core-shell structure impossible. This part will be discussed in Section 3.1.

Functionalization of supporting carbon material was then tried to control the nanoparticle size and enhance the particle distribution on the carbon surface. In the research, it is found that the type of functional groups created on the carbon surface can affect the rhodium cation adsorption at the certain pH, and the subsequent Nafion electrolyte distribution on the catalyst carbon support surface. It has been shown that the carboxylic group on the carbon surface is not good for adsorbing Rh^{3+} but has good affinity for the distribution of Nafion polymer electrolyte on the catalyst surface, while the ketone group is good for adsorbing Rh^{3+} cation but shows poor affinity to the Nafion polymer electrolyte.[47] The efforts to improve the mass-specific surface area of electrocatalyst through the functionalization of carbon material and maintain good its affinity to the Nafion electrolyte will be discussed in Section 3.3 and Section 3.5.

The second drawback of the current catalyst is from the low activity crystal phase of rhodium sulfide catalyst. There are two possible methods to adjust the composition of crystal phases of rhodium sulfide, adjusting the temperature of the thermal treatment process or introducing different types of sulfur sources. Due to the narrow temperature window between Rh_2S_3, Rh_3S_4 and $Rh_{17}S_{15}$, the adjusted temperature may result in the existance of corrodible Rh metal or inactive Rh_2S_3. Applying new type of sulfur sources was then tried to improve the composition of Rh_3S_4 in Rh_xS_y. The mechanism of crystal phase modification using this approach will be discussed later in Section 3.4. To my best knowledge, this is the first work to modify the crystal phases of rhodium sulfide by different sulfur sources. This work will be discussed in Section 3.4.

The performance of the electrocatalyst in a real H_2-Br_2 fuel cell from the functionalized carbon material which can adsorb Rh^{3+} effectively and distribute Nafion ionomer uniformly on the surface, application of new sulfur source which increases the Rh_3S_4 in Rh_xS_y, and the diffusion-controlled nanoparticle growth model will be discussed in Section 3.5.

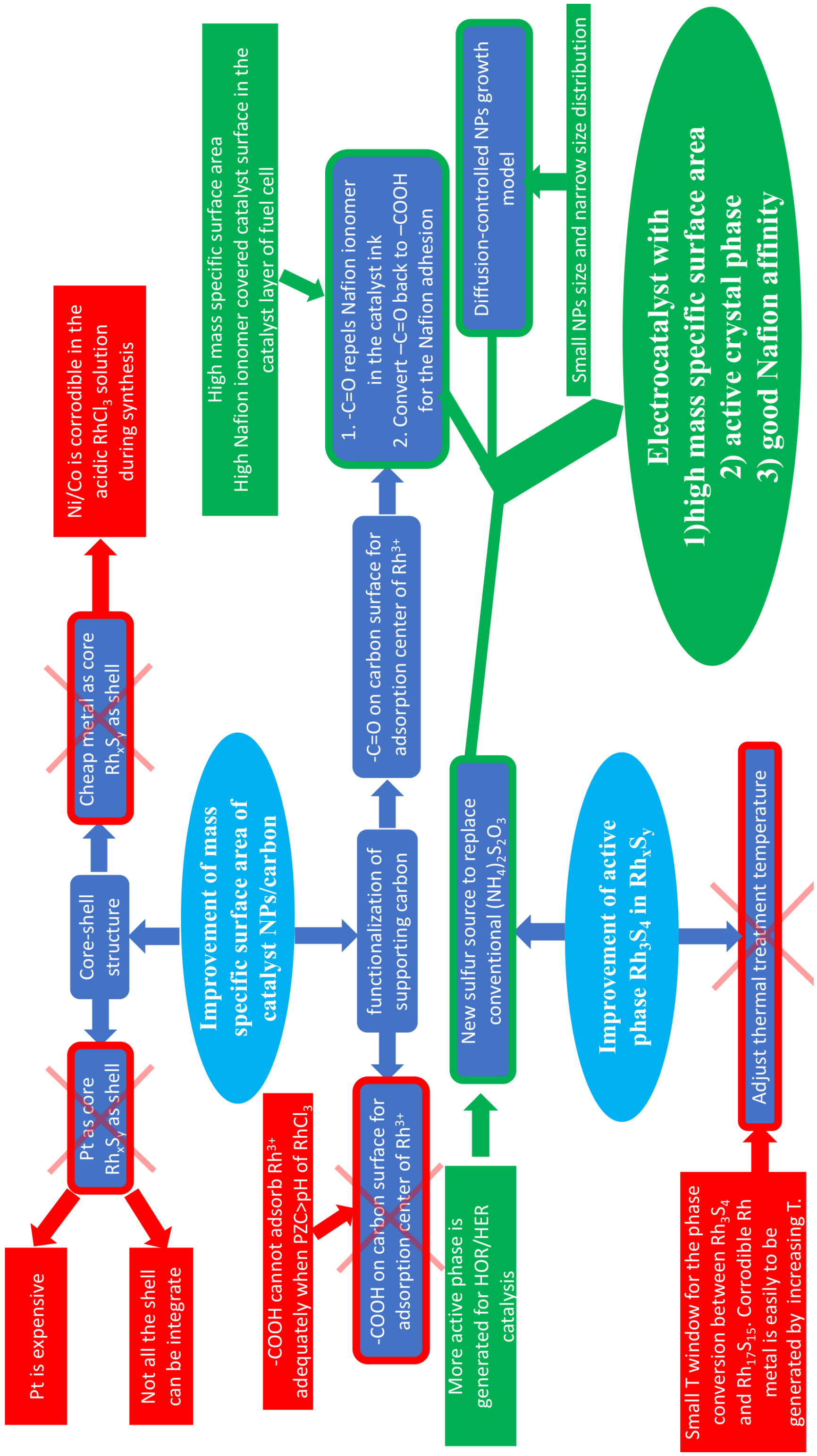

Figure 1.9. Roadmap to develop electrocatalyst with high mass specific surface area, highly active crystal phase, and high Nafion affinity in the catalyst layer

Chapter 2

Materials and Experimental Methods

2.1 Synthesis of Core-shell Rh_xS_y

2.1.1 Synthesis of Pt-core and Rh_xS_y-shell Nanoparticle

The rhodium sulfide precursor synthesis process by Gulla and Allen was used to synthesize Rh_2S_3 precursor shell.[48] The rhodium (III) chloride hydrate ($RhCl_3 \cdot 3\,H_2O$) (Alfa Aesar) was dissolved in deionized water (DI water) and refluxed at 100°C for 2 h. Pt/C powders with different percentage of Pt (5%, 10%, and 20%) were then added to the solution. The 5% Pt/C material comes from Alfa Aesar, and its carbon substrate is made of activated carbon. The 10% Pt/C material also comes from Alfa Aesar and uses graphite carbon substrate. The 20% Pt/C coming from E-TEK uses XC72R, a widely used graphite carbon substrate for fuel cell catalyst, as carbon substrate. The weight ratio of rhodium to platinum was 1.7:1. The mixture was sonicated for 2 h to disperse the solid. The sulfur source, $(NH_4)_2S_2O_3$, was added to the mixture, and the solution was refluxed at 100°C for 2 h. During this time, Rh^{3+} cation and S^{2-} anion, which was generated from the dissociation of ammonia thiosulfate, precipitated on the Pt cores. The Pt core-Rh_2S_3 shell precursors on carbon support were washed in DI water and dried at 100°C overnight. Then it was converted to active phases by thermal treatment under argon purge. The temperature of the thermal treatment was 675 °C. Two sets of temperature ramp were explored as the Table 2.1.

Table 2.1. Fast/slow temperature ramp for the thermal treatment of core-shell catalyst

	Temperature Range_°C	Temperature Ramp_°C/min	Time_min
Fast Heating/Cooling Down	20-650	10	65
	650-675	2	13
	675-675	-	180
	675-20	uncontrolled	60
Slow Heating/Cooling Down	20-300	5	56
	300-675	2	187
	675-675	-	180
	675-20	-2	327

2.1.2 Synthesis of Ni-core and Rh_xS_y-shell Nanoparticle

$RhCl_3 \cdot 3H_2O$ was dissolved in deionized water (DI water) and refluxed at 100°C for 2 h. 20% Ni/XC72R powders which were provided by Prof. B.J. Hwang of National Taiwan University of Science and Technology were then added to the solution. The weight ratio of rhodium to Ni was 1.7:1. The mixture was sonicated for 2h to disperse the solid. $(NH_4)_2S_2O_3$ was added to the mixture, and the solution was refluxed at 100°C for 2 h. After the precipitation reaction between the Rh^{3+} and S^{2-} on the surface of Ni NPs. The Ni core-Rh_2S_3 shell precursors on carbon support were washed in DI water and dried at 100°C overnight. Then it was converted to active phases by thermal treatment under argon purge. The temperature of the thermal treatment was 675°C with the slow temperature ramp mentioned in the section above.

2.2 Synthesis of Pt-doped Rh_xS_y

The general method to synthesize rhodium sulfide catalyst with Pt doping is also from the patent of Gulla and Allen. The $RhCl_3 \cdot 3H_2O$ with H_2PtCl_6 (5% of Rh amount) was dissolved in deionized water (DI water) and refluxed at 100°C for 2 h. It was then mixed and sonicated with the activated carbon, XC72R, for 2 h at 40°C. The weight ratio of precious metal to carbon was 1:3. The mixture of solid and metal salt was refluxed to 70°C. When the temperature was stable, the sulfur source, $(NH_4)_2S_2O_3$, was added to the mixture via three equivalent aliquots. After the $(NH_4)_2S_2O_3$ solution was added, the mixture was finally refluxed at 100°C for 2 h. The conversion from the precursor to the catalyst was accomplished by the thermal treatment as well. Since the core-shell structure is not involved in this rhodium sulfide synthesis, the fast temperature ramp was used to save time.

2.3 Functionalization of Carbon Material

The carbon material, XC72R, was functionalized by oxidation in a concentrated HNO solution, reduction by H_2 and overnight air exposure. First, 1 gram of XC72R was oxidized in 20mL of concentrated HNO_3 (68% wt) at 80°C for 8 h to create carboxylic groups on the surface. This material was named XC72R-HNO_3. The oxidized XC72R was washed, filtered to remove the acid, and then dried in an oven at 90°C overnight. Second, the XC72R-HNO_3 was reduced in a quartz reactor at 300°C while being purged with 20% H_2/argon for 3 h. Last, the reduced XC72R was sealed in an air-filled vial overnight for oxygen exposure. The carboxylic groups generated in the first step were converted into ketone groups after the air exposure. After this step, the material was named XC72R-HNO_3-H_2-Air, and it will be called the pretreated carbon in the rest of the dissertation. The pretreated carbon was used the following day in the synthesis of the precursor of Rh_xS_y catalyst.

2.4 Synthesis of Rh_xS_y from $(NH_4)_2S_2O_3$ on Functionalized Carbon

The synthesis process designed by Gulla and Allen was used to synthesize the rhodium sulfide precursor Rh_2S_3 on the functionalized carbon. Rhodium (III) chloride hydrate ($RhCl_3 \cdot 3\,H_2O$) from Alfa Aesar was dissociated in DI water and refluxed at 100 °C for 2 h. The solution was removed from the reflux column, and pretreated carbon XC72R powder was added to the solution after the solution was cooled to 40°C. The weight ratio of rhodium to carbon was 1:3. The mixture was sonicated at 40°C for 2 h to disperse the solid and returned to the reflux column. The mixture was then heated up to 70°C. The sulfur source, $(NH_4)_2S_2O_3$, was added to the mixture when the temperature was stable at 70°C, and the solution was refluxed at 100°C for 2 h. During this time, the decomposition of $(NH_4)_2S_2O_3$ generated S^{2-} anions that precipitated the Rh^{3+} ions on the pretreated carbon. The carbon supported precursor Rh_2S_3/C was washed in DI water and dried at 90°C overnight.

The conversion of the precursor to rhodium sulfide catalyst was accomplished by thermal treatment with argon purge in a quartz reactor, during which sulfur atoms were removed and the precursor was converted to the active phases, Rh_3S_4 and $Rh_{17}S_{15}$(called here Rh_xS_y because it is a mixture of both). The thermal treatment was done at 700°C for 3 h. The temperature ramping rates were: 1) room temperature to 650°C at 10°C/min, 2) 650-675°C at 2°C/min, and 3) 675-700°C at 1°C/min. The cooling down process was not controlled.

2.5 Synthesis of Rh_xS_y from Na_2S on Functionalized Carbon

The rhodium (III) chloride hydrate ($RhCl_3 \cdot 3H_2O$) (Alfa Aesar) was dissociated in DI water and refluxed at 100°C for 2 h. Pretreated carbon powder, XC72R, was then added to the solution. The weight ratio of rhodium to carbon was 1:3. The mixture was sonicated for 2 h to disperse the solid. Na_2S was dissociated into DI water in weight ratio of 6.84 gram of water to 1 gram sulfide ion. Then the solution was added to the rhodium chloride/carbon mixture at 100°C by a peristaltic pump in 2 h (3 mL/h). The dissociation of Na_2S generated S^{2-} anion which precipitated Rh^{3+} on the pretreated carbon. The precursor, Rh_2S_3, was washed in DI water and dried at 90°C overnight.

The conversion from precursor to active catalyst was accomplished by thermal treatment with argon purge, during which sulfur atoms are removed and the precursor was converted to the active phases, Rh_3S_4 and $Rh_{17}S_{15}$. The thermal treatment was done at 700°C for 3 h. The temperature ramp rate was: room temperature to 650°C at 10°C /min; 650-675°C at 2°C/min; 675°C-700°C at 1°C/min.

2.6 Material Characterizations

The morphology and chemical compositions of the samples were determined by an FEI Tecnai F20 XT Field Emission Transmission Electron Microscope (TEM) coupled with an energy-dispersive X-ray spectrometer (EDX) at an acceleration voltage of 200 kV. The line-scans for the core-shell particles were measured during HAADF-TEM. The step intervals of the line-scans were 0.662 and 0.263 nm, respectively, and the resolutions of HAADF-TEM were 20 and 10 nm, respectively. X-ray powder (XRD) patterns were obtained using monochromated Cu-Kα radiation (λ = 1.54178Å) on a Bruker Proteum diffraction system equipped with Helios high-brilliance multilayer optics, a Platinum 135 CCD detector and a Bruker Microstar microfocus rotating anode X-ray source operating at 45 kV and 60 mA. The scanning was done from 5-90° (2θ) with step size of 0.5°. In the XPS measurements, the prepared catalysts were analyzed by a PHI 5000 Versa Probe II electron spectrometer with Monochromated Al as the X-ray source. The XPS binding energies were measured with a precision of 0.2 eV. The analyzer pass energy was set to 23.5 eV. The take-off angle is 45° and the beam size is 100 microns. For each measurement, the XPS spectra were corrected to the internal reference spectra of C 1s at 284.5 eV to compensate for electrostatic charging. The carbon surface functional groups were analyzed by Fourier Transform Infrared Spectroscopy (FT-IR) using a VERTEX 80 from Bruker. In these measurements, the carbon samples were ground to fine powder and then mixed with KBr by a weight ratio of 100:1. The mixture was used to prepare KBr pellets for analysis. The IR spectrum was obtained over a frequency range of 400 to 4000 cm^{-1}. The FT-IR background signal was measured using pure KBr pellet and subtracted from the subsequent measurements.

2.7 Baeyer-Villiger Reaction and Ester Hydrolysis

After the thermal treatment of the catalyst synthesized with the pretreated carbon, the main functional group on the carbon surface is the ketone group, which can be converted into the carboxylic group by the Baeyer-Villiger reaction. 86.8 mg rhodium sulfide catalyst powder and 13.4 mg Baeyer-

Villiger reaction catalyst (9-Mesityl-10-methylacridinium perchlorate) were mixed with 54.2 mL solvent (water or methanol) and 441.2 μL oxidant (30% H_2O_2). The mixture was refluxed at 55°C for three days. The solid was washed and centrifuged by seven times. Then it was dried overnight at 100°C. The final product of the Baeyer-Villiger reaction is the ester group which needs to convert into the carboxylic group by the hydrolysis. 1 mg solid was mixed with 1 mL 36% HCl solution and refluxed at 77°C for 8 h. The product was washed and centrifuged until the pH of the washing solution reached to 7. It was dried overnight at 100°C.

2.8 Electrochemical Measurements

2.8.1 Electrode Preparation

A gas diffusion layer (GDL) was used as the support for the catalyst for the cyclic voltammetry test. The GDL (SGL-10AA) was cut into a 2 cm by 1 cm piece and then soaked in the 2M HNO_3 solution to make it hydrophilic. After rinsing it with DI water, the GDL was dried in an oven at 80°C overnight and then weighed. A catalyst ink was prepared by sonicating a mixture of Rh_xS_y /C catalyst powder and isopropanol alcohol (IPA), 4 mg catalyst powder and 2 mL of IPA. The catalyst ink was applied onto one of the surfaces of the GDL with a brush. The gas diffusion electrode (GDE) was dried at 80°C for 1 h and weighed. The weight difference between the GDE and GDL is the weight of the catalyst coated on the electrode. The advantage of using a GDE as a working electrode instead of the conventional glassy carbon rotating electrode (RDE) is the ability to obtain an accurate measurement of the mass of the catalyst; this was needed in order to calculate the mass-specific surface area accurately. Finally, 2%-wt Nafion ionomer solution was applied on the surface of the catalyst layer. The Nafion ionomer was used as a binder for the catalyst layer. The GDE with Nafion coating was annealed at 135°C for 5 min and allowed to cool to room temperature.

2.8.2 Cyclic Voltammetry (CV)

2.8.2.1 CV for electrochemical surface area of catalyst

All electrochemical measurements were made with a Gamry Instrument (G300 Potentiostat/Galvanostat/ZRA). Electrochemical measurements were carried out in a glass beaker filled with 1M H_2SO_4 with the GDE made in the above-mentioned procedure as the working electrode, and a Pt wire as the counter electrode. The working electrode was held by the fixture shown in Fig 2.1. Nitrogen gas was passed through the solution continuously during the CV scan. All measurements were at room temperature unless otherwise states. Each CV contained five cycles from 0-0.425 V vs. RHE. The last cycle was plotted. The electrochemical active surface area (ECSA) of the catalyst is calculated in comparison with Pt. The equation used to calculate the Pt equivalent ECSA is,

$$ECSA = Q_H/0.21 \tag{2.1}$$

where QH (mC) is the charge from the oxidation of adsorbed hydrogen, 0.21 mC/cm^2 is the electrical charge associated with a monolayer of absorbed hydrogen on Pt. The charge from the oxidation of hydrogen was corrected for double-layer charging.

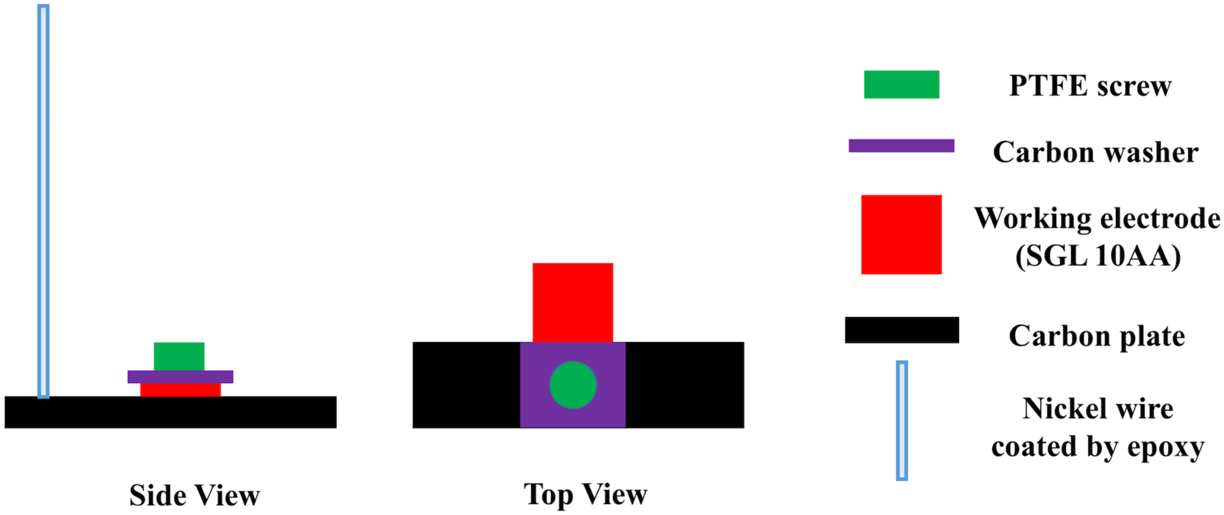

Figure 2.1. Schematic of fixture of working electrode

2.8.2.2 CV for the oxidation potentials of the carbons with different functional groups

The carbons with different functional groups were scanned from 0.4 to 1.1 V vs. RHE in a glass beaker filled with 1M H_2SO_4. The three-electrode system is a glassy carbon plate coated with carbon powder as a working electrode, a saturated calomel electrode as a reference electrode, and a Pt wire as the counter electrode. The working electrode was connected to the Gamry potentiostat through an epoxy-coated nickel wire. Nitrogen gas was passed through the solution continuously during the scan.

2.8.3 Multiple-Step Chronoamperometry

2.8.3.1 Activity measurement in H_2SO_4 solution

The exchange current density (i_o) is an important kinetic parameter representing the catalytic activity of a catalyst. The Butler-Volmer equation can be simplified to a linear relationship when the value of η is sufficiently small ($|\eta| < 25\ mV$). In this small η range, the effect of ohmic and mass transport is negligible allowing one to measure the kinetic property of the catalyst directly using the equation below:

$$i = a i_o \frac{nF}{RT} \eta \tag{2.2}$$

where i represents the measured current density in A/cm^2 of geometric area, a is the catalyst area per geometric area, i_o is the exchange current density in A/cm^2 of catalyst area, F is Faraday's constant, R is the universal gas constant, T is temperature, and $\eta = E - E_{eq}$ is the overpotential. Thirty microliters (30 µL) of the catalyst ink, prepared as mentioned above, were dropped on the surface of glassy carbon RDE. Then 10 µL of 0.1% wt Nafion solution was dropped on the catalyst layer. The RDE with loaded catalyst was dried at 90°C for 30 min and cooled to RT. Before the activity test, the ECSA of the loaded catalyst was measured by CV in the nitrogen-saturated 1M H_2SO_4 solution without rotation. The HOR/HER activity was measured in hydrogen saturated 1M H_2SO_4 solution with RDE rotating speed as 2400 rpm. After the activity test, the ECSA was measured again in the nitrogen-saturated 1M H_2SO_4 solution to correct for any loss of catalyst by electrode rotation during the activity test. The ECSA reported was an average of the initial and final ECSA values. Only the data in the kinetics-controlled region were used to calculate the activity.

2.8.3.2 Activity measurement in HBr solution

The electrolyte was changed from 1M H_2SO_4 to 2M HBr to keep the same concentration of H^+ ion. The salt bridge prepared as below was used to protect counter electrode from the corrosion of HBr solution. The working electrode and the reference electrode (saturate calomel electrode, SCE) were placed in a flask filled with 2M hydrogen-saturated HBr solution, while the counter electrode (Pt) was placed in another flask filled with 1M hydrogen-saturated H_2SO_4 solution. The two flasks were connected with a salt bridge for the ionic connection. The measurement operation was similar to the activity measurement in H_2SO_4 solution.

The salt bridge was prepared as follow,

1. Prepare 1M KCl solution
2. Take 40 mL of prepared KCl solution and mix it with 2 gm Agar.
3. Heat the mixture with stirring bar until bubble forms.
4. Meanwhile, take 4 pipes and clean them with DI water.
5. Draw the Agar solution into the pipes as soon as possible. And then keep the pipes into KCl solution.

2.8.4 Durability Test of Catalysts

After the initial test by the cyclic voltammetry in the N_2 saturated 1M H_2SO_4 solution, the GDEs with core-shell catalysts and commercial catalyst were soaked in 1M HBr solution at room temperature. The first soakings were 24 hours for the commercial catalyst and 35 hours for the core-shell catalysts. Then the GDEs were washed by the hot DI water (80°C) to removed adsorbed bromine/bromide and retested by the CV. The same GDEs were soaked in HBr solution, washed by hot DI water and tested by the CV after 80 hours and 135 hours. The CV scanned from 0 to 0.425V and scan rate was 10 mV/s.

2.8.5 Fuel Cell Cycling Test

Fuel cell cycling was used to evaluate the durability of Rh_xS_y and platinum catalysts. It was conducted with 1 cm^2 electrode with closed catholyte and recirculated hydrogen. Three plain gas diffusion layers (SGL-10AA) pretreated by 2M HNO_3 solution were used as the Br_2 positive electrode. Bi-layer carbon gas diffusion media (SGL-25BC) coated with various types of Rh_xS_y/C and Pt/C were used as the hydrogen negative electrode. The GDE of the negative electrode was prepared by painting a solution of Rh_xS_y/C, Nafion ionomer and 50:50 DI water: isopropyl alcohol on the microporous layer (MPL) of the bi-layer carbon gas diffusion medium with a brush. The weight ratio of catalyst to Nafion ionomer was 1:10. The catalyst loading in the hydrogen electrode was approximately 0.5 mg/cm^2. This number is the total mass of the catalyst containing catalyst and carbon support. The membrane electrode assemblies (MEAs) were made with commercially available Nafion 212 membranes. Interdigitated flow fields were used for all the experimental studies. The catholyte was 1M HBr/0.9M Br_2 solution. The Br_2 pump flow rate was 1.5 cm^3/min. The hydrogen pressure was held at 122 kPa. A humidified bottle was used to saturate hydrogen with water vapor to facilitate hydration of the ionomer phase in the hydrogen electrode. Because of crossover and leakage, 10% of catholyte was replenished every 24 hrs. It can be improved by reducing the permeability of the membrane and better sealing of the fuel cell in the future. The fuel cell cycling test was terminated when a stable discharge capacity was achieved. Then the polarization curve was measured. In the cycling test, the fuel cells with catalysts RhxSy@10%Pt/C, RhxSy@20%Pt/C and 30% Pt/C were discharged at 80 mA until the voltage dropped to 0.3 V. Then the fuel cells were fully charged back at 80 mA to recover the active materials. For the RhxSy@5%Pt/C and commercial BASF catalyst, the discharge current and cut-off voltage of 20 mA and 0.3 V were used respectively. The charge current was 60 mA. The different discharge and charge current were used to account for the lower active areas of these two catalysts. All the experiments were conducted at room temperature unless otherwise specified.

2.8.6 Fuel Cell Polarization Curve Measurement

2.8.6.1 Fuel cell polarization curve measurement for the core-shell catalysts

The fuel cell testing was used to evaluate the catalyst performance in a real H_2-Br_2 fuel cell. The polarization curves were obtained with the same fuel cell used for the fuel cell cycling test. The flow rate of catholyte and pressure of hydrogen were kept the same as in the cycling test. At the end of each experiment, the internal impedance resistance of the fuel cell was acquired using Electrochemical Impedance Spectroscopy (Gamry EIS 300, Amplitude: 5 mV and Frequency range: 0.1 Hz to 100 kHz).

2.8.6.2 Fuel cell polarization curve measurement for Rh_xS_y/pretreated carbon from $(NH_4)_2S_2O_3$

Three layers of 1.5×1.5 cm plain SGL carbon (10AA) gas diffusion layer (GDL) pretreated in 2M HNO_3 solution were used as the Br_2 electrode, and a bi-layer carbon gas diffusion medium (SGL 25BC) coated with various types of Rh_xS_y/C catalyst was used as the hydrogen electrode. Two mixtures of Rh_xS_y/C and Nafion ionomer ink (1:1 and 10:1 as wt ratio respectively) were prepared and stirred overnight. The catalyst ink was painted on the microporous layer (MPL) of the bi-layer carbon gas diffusion medium with a brush. The catalyst loading in the hydrogen electrode was approximately 2.3 mg/cm^2. This number represents the total mass containing catalyst and carbon support. The membrane electrode assemblies (MEAs) were made with commercially available Nafion 212 membranes. A 1M HBr/0.9M Br_2 electrolyte mixture was fed to the Br_2 electrode in the H_2-Br_2 fuel cell experiments.

The following operating conditions were used in the H_2-Br_2 fuel cell tests. H_2 gas at 122 kPa was recirculated through the H_2 electrode. Excess Br_2 solution circulated at 13 cm^3/min was used to ensure the Br_2/Br^- concentration remained constant during the discharge and charge tests. Interdigitated flow fields were used in all fuel cell experiments. Also, a humidified bottle was used in the hydrogen recirculation loop to facilitate and maintain hydration of the ionomer phase in the hydrogen electrode. All the experiments were conducted at room temperature (22°C) unless otherwise specified. At the end of each experiment, the internal ohmic resistance of the fuel cell was acquired using Electrochemical Impedance Spectroscopy (Gamry EIS 300, Amplitude: 5 mV and Frequency Range: 0.1 Hz to 100 kHz).

2.8.6.3 Fuel cell polarization curve measurement for Rh_xS_y/pretreated carbon with surface functional group conversion from $(NH_4)_2S_2O_3$ and Na_2S

All the measurement operations were same with that for Rh_xS_y/pretreated carbon from $(NH_4)_2S_2O_3$ except the wt ratio of Rh_xS_y/C and Nafion ionomer in the catalyst ink was 1:1.

2.9 pH Measurement

The $(NH_4)_2S_2O_3$ was dissociated into DI water with same weight ratio mentioned in the synthesis of Rh_2S_3. A pH meter and temperature sensor with glass tube were inserted into the vial with $(NH_4)_2S_2O_3$ solution. The initial pH was recorded when the reading was stable. Then the vial was heated to 100°C. During the heating, the temperature and pH were recorded every 30 s. After the temperature reached 100°C, the pH was continuously recorded every 1 min for 1 h.

2.10 Computational Methods

A theoretical calculation with density functional theory (DFT) of the electrostatic potential (ESP) on the Nafion ionomer and carbon clusters with different chemical groups was calculated by the Gaussian 03 software. The fullerene-related structure was chosen for the theoretical model of activated carbon. The model is a $C_{45}H_{15}$ cluster containing one pentagonal and fifteen hexagonal rings. The structures of Nafion ionomer and carbon clusters were firstly optimized by semi-empirical method PM6 and then calculated for the single point energy by B3LYP/6-31g of DFT.

The definition of ESP for the molecular system is,

$$V_{tot}(r) = V_{nu}(r) + V_{ele}(r) = \sum \frac{Z_A}{| r - R_A |} - \int \frac{\rho(r')}{| r - r |} dr \qquad (2.3)$$

where Z is the charge of nuclear charge and R is the coordinates of the atomic nucleus. ESP is composed of the positively charged atomic nucleus and negatively charged electrons. The ESP is always positive in the neighboring region of the atomic nucleus which does not play a significant role in the chemical reaction and physical property of the molecule. The contribution of electrons can balance the effect of the atomic nucleus. The inhomogeneous distribution of electron density on the surface of molecules leads to the positive/negative ESP. The negative ESP often shows on the regions with the lone pair of electrons, and π electronic cloud due to the high electron density.

Chapter 3

Results and Discussion

3.1 Core-Shell Rhodium Sulfide Catalyst for Hydrogen-Bromine Reversible Fuel Cell

Due to the unavoidable crossover of HBr/Br_2 with the current proton exchange membrane, the commonly used HOR/HER catalyst, Pt, cannot be used in the hydrogen-bromine fuel cell. Rh_xS_y catalysts have been found to be stable in the HBr/Br_2 environment and shown similar specific areal activity as platinum.[49,50] However, due to the large particle sizes and broad particle size distributions (12-40 nm), commercial Rh_xS_y catalysts have low mass-specific ECSA (<10 m^2/g) and activity for HOR.[51,52,53,54] The core-shell approach was explored to increase the mass-specific ECSA of these Rh_xS_y catalysts to address this problem. The core-shell structure has been applied to various fields like catalysts, industrial and biomedical applications.[55] One of the advantages in the core-shell structure is to increase the utilization of expensive metal material since the relatively cheaper material can replace the expensive one in the interior of nanoparticles which is not utilized for the heterogeneous catalysis reaction. The mass-specific surface area of a core-shell catalyst can be improved hugely if the shell thickness is well controlled. To synthesize rhodium sulfide catalyst with core-shell structure, the commercial Pt/C with small average particle size and narrow size distribution, was used as the core material for the preliminary research to prove this concept. Then a cheaper metal, Ni/C, was used as the core material to reduce the cost of electrocatalyst in the hydrogen-bromine fuel cell.

3.1.1 Selection of Fast/Slow Temperature Ramp for Thermal Treatment of Core-Shell Nanoparticle

The core-shell structure on inorganic nanoparticles (NPs) is often created by the aqueous reduction, sol-gel method, and electrodeposition at low temperature. For instance, Pt@Au was synthesized by two steps.[56] The $AuCl^-$ was reduced to Au nanoparticles by sodium citrate at 80°C. Then the Au seeds were mixed with the platinum source H_2PtCl_6. The ${PtCl_6}^{2-}$ was then reduced by ascorbic acid with 80°C heating. From the description above, it can be found that the highest temperature of the whole synthesis process is 80 °C. In the synthesis of rhodium sulfide catalyst with core-shell structure, the core materials are provided by the Pt or Ni metallic nanoparticle loaded on the activated carbon powders. Then the shell material, rhodium sulfide, is coated on the surface of core NPs in the form of the precursor, Rh_2S_3, which is not active in catalyzing HOR/HER. The way to reduce the Rh_2S_3 into active phases is the thermal reduction at the high temperature, around 700°C. For the wide temperature range, the different expansion and contraction rates of core and shell material may create cracks in the shell which can expose the corrodible core material to the corrosive environment. Two sets of temperature ramps were designed to explore the relationship of the integrity of shell and fast/slow temperature ramp.

In the Figure 3.1, the core-shell catalysts with fast/slow temperature ramp in the thermal treatment were measured by cyclic voltammetry after 150 h HBr soaking. It can be seen that the core-shell catalyst with fast temperature ramp in the thermal treatment (purple curve with triangle markers) completely lost the capability to catalyze the HOR/HER, while the core-shell rhodium sulfide catalyst with slow temperature ramp (blue curve with round markers) still shows the current peaks for the HOR and HER. The disappearance of HOR/HER peak in the CV of the core-shell catalyst with fast temperature ramp indicates that all the shells were broken and the whole core-shell catalyst NPs are corroded during HBr soaking. The different performances in the durability of catalysts with fast/slow temperature ramp can be attributed to the difference of the thermal expansion rate of the core and shell material. The linear temperature expansion coefficient for the Pt is $9\times10^{-6}\mathrm{m/(m\,K)}$, while there is no reported data for rhodium sulfide.[57] The nickel and copper

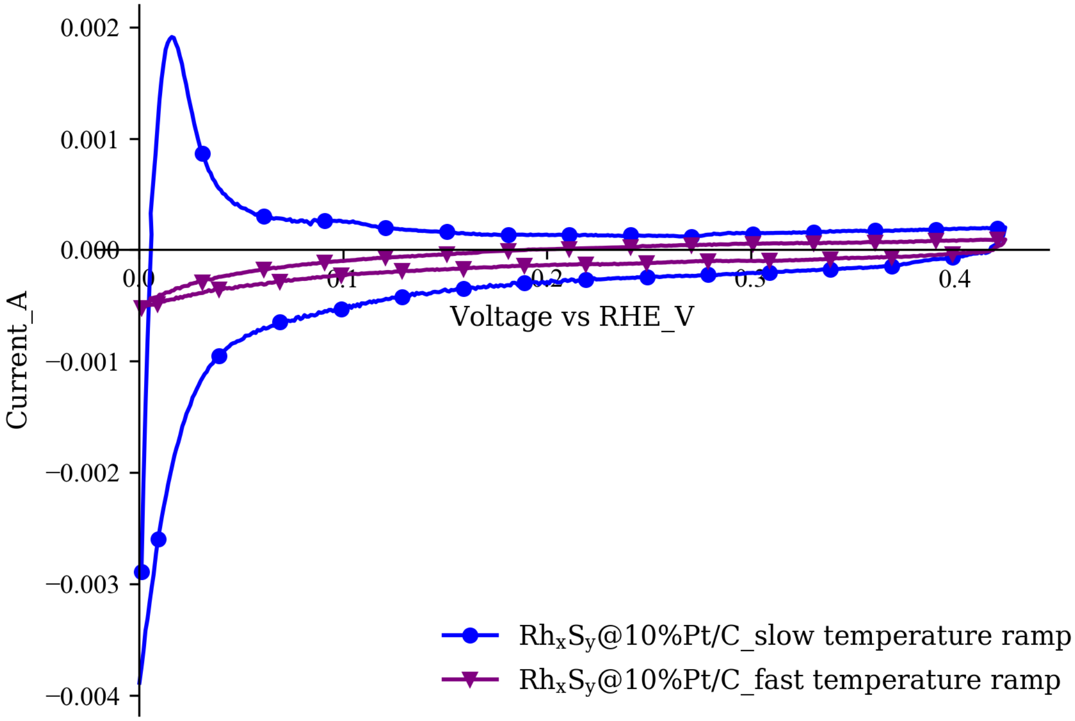

Figure 3.1. Cyclic voltammograms of Rh_xS_y@10%Pt/C with fast and slow temperature ramp after 150 h HBr soaking (electrolyte: 1M N_2-saturated H_2SO_4 solution, working electrode: catalyst-coated GDE, counter electrode: Pt foil, reference electrode: SCE, scan rate: 10mV/s)

sulfide with the linear temperature expansion coefficient of 15 and $20.6 \times 10^{-6} \mathrm{m/(m\,K)}$ respectively may provide some references.[58] In the heating process, the rhodium sulfide shell with a higher thermal expansion rate detaches from the Pt core material with a lower thermal expansion rate. Then the detached shell contracts faster in the cooling process, which results in the cracking of the shell and exposure of metallic cores to HBr/Br_2.

From Figure 3.1, the fast temperature ramp, shown in the Table 3.1, is responsible for the cracking of the shell. The slow temperature ramp of thermal treatment helps to protect the integrity of the shell. Based on the durability test, the slow temperature ramp for the thermal treatment is selected for all the catalysts synthesis mentioned later.

3.1.2 Characterizations of Core-shell Structure, Nanoparticle Size and Distribution

3.1.2.1 XRD

The XRD result of the core-shell catalyst with 10% Pt/C is shown in Fig 3.2. The XRD curve of core-shell catalyst shows the mixed crystal structures of $Rh_{17}S_{15}$ and Pt. There are two possible reasons for the mixture of crystal phases. The first possible explanation is the depth of detection of XRD is larger than the thickness of the shell. The penetration depth of XRD can vary from 4 nm to 10 nm which is larger than the thickness of the Rh_xS_y shell on the Pt core. The shell thickness is discussed later in TEM pictures in Figure 3.3. The second possible reason is that some of the platinum cores are exposed by the partially formed shell of rhodium sulfide, and XRD detected the exposed platinum core. The discussion of partially covered platinum cores is covered later in Figure 3.4.

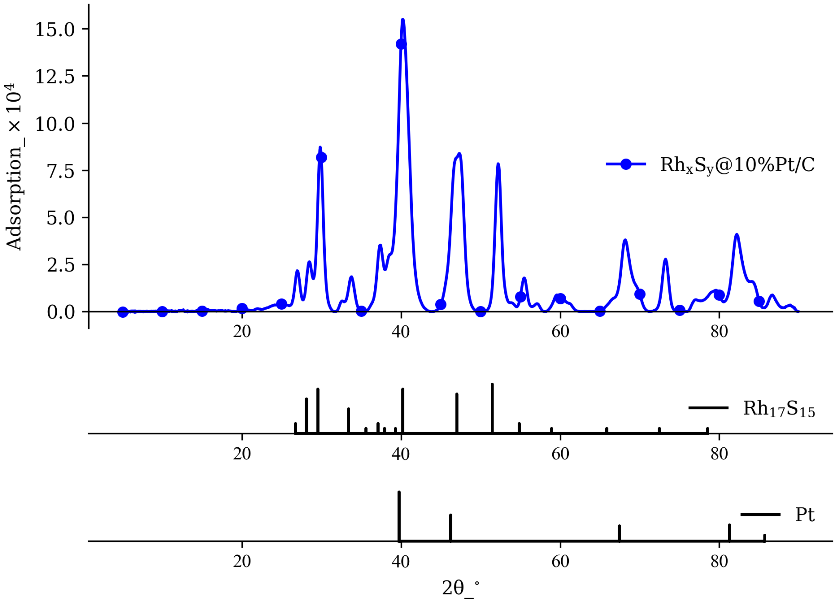

Figure 3.2. XRD of core-shell catalyst with 10% Pt/C (JCPDS for Pt: 001-1194, JCPDS for $Rh_{17}S_{15}$: 073-1443)

3.1.2.2 TEM

As mentioned earlier, by using smaller metal cores with narrow particle size distributions as seeds to create rhodium sulfide shells, rhodium sulfide catalysts with smaller particle sizes and narrower size distributions was synthesized to increase the mass-specific area, activity and rhodium utilization. Figure 3.3 shows the particle sizes of various catalysts and their core materials (Pt/C). The conventional rhodium sulfide catalyst (Figure 3.3(a)) shows large particle sizes, 13 nm, while the core-shell catalysts synthesized with 5% Pt/C (Figure 3.3(c)) and 10% Pt/C (Figure 3.3(e)) show much smaller particle sizes, 4 nm. From the TEM micrographs of the core and core-shell catalysts in Figure 3.3(b) and Figure 3.3(d), the smaller core-shell rhodium sulfide catalyst size can be credited to the well-distributed and small size of Pt nanoparticles. The average shell thickness calculated from the average size of Pt seeds and core-shell catalysts (average thickness of shell = average diameter of core-shell catalyst – average diameter of core material)/2) is about 1 nm for core-shell catalyst with 5% and 10% Pt/C. This shell thickness is near the optimal rhodium sulfide shell because the thickness of a single supercell of $Rh_{17}S_{15}$ is about 0.9 nm.[45,59] A supercell is needed to ensure the integrity of the crystal structure for stability in HBr and Br_2 solution. A thicker shell is undesirable because it results in lower utilization of rhodium in the catalyst. The core-shell rhodium sulfide synthesized with 20% Pt/C (Figure 3.3(g)) shows large particle size and very broad size distribution. This is attributed to poor Pt nanoparticle distribution at higher Pt loading, having many Pt particles in near proximity to one another, which leads to large rhodium shells covering multiple Pt cores and consequently large core-shell particles. The poor Pt nanoparticle distribution claim is supported by the TEM picture shown in Figure 3.3(f). The average shell thickness for this kind of core-shell catalyst is 2 nm, which also demonstrates the fact that multiple Pt cores are covered by the same shell.

The particle distribution of core-shell catalyst with 10% Pt/C is shown in Figure 3.3(h). From these results, one can see that more than 70% of core-shell catalyst particles made with 10% Pt/C is below 5 nm. Compared with non-core-shell catalyst, core-shell catalysts have much smaller average particle size and narrower size distribution.

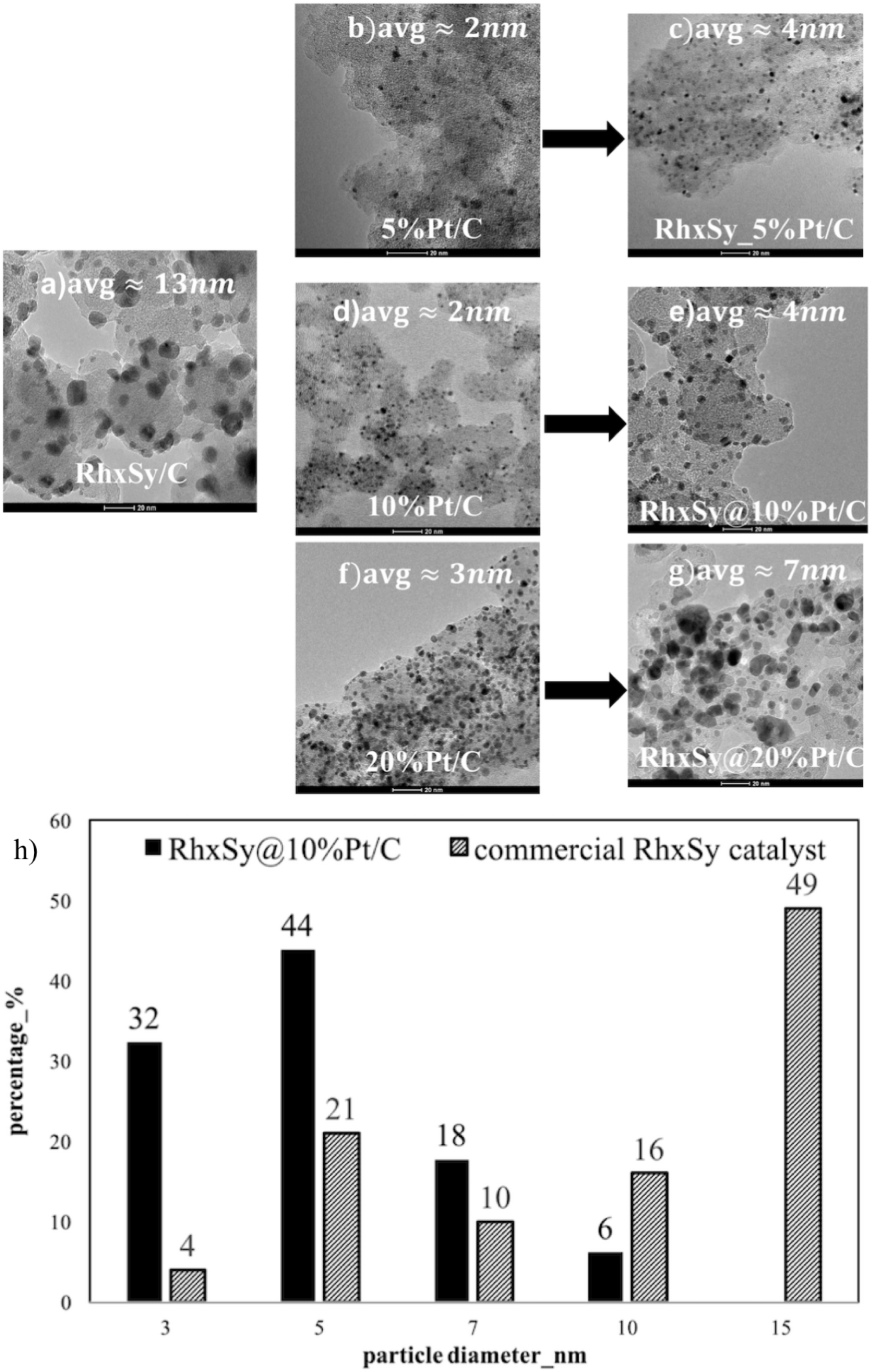

Figure 3.3. TEM picture of non-core-shell and core-shell catalyst (scale bar: 20 nm)

Next, the core-shell structure was investigated by TEM-EDX. The results are presented in Figure 3.4. For bright field TEM, the heavier elements will appear in a darker shade. Platinum with atomic number 78, versus Rh with atomic number of 45, will appear in the darker shade in these figures. In Figure 3.4(a), one can see that the darker Pt core is fully covered by the lighter Rh sulfide shell. In the 2nd TEM micrograph in Figure 3.4(a), one can see two adjacent Pt particles covered by the same rhodium sulfide shell. This picture shows that when platinum nanoparticles are not well dispersed, large core-shell particle can result, as supporting evidence for the large core-shell particles observed with the rhodium sulfide catalyst synthesized with the low dispersion 20% Pt/C material. The TEM micrograph in Figure 3.4(b) shows a partial core-shell catalyst particle synthesized with 10% Pt/C. One can see that there is a spot where Pt is not covered by rhodium sulfide. Line scan TEM-EDX was also used to investigate the core-shell structure. From the elemental distribution in Figure 3.4(c), one can see three platinum cores based on the intensity of the platinum line (line with circle symbol) and that these three platinum cores are completely covered by rhodium sulfide shells by the continuous intensity line of rhodium over the platinum intensity line at these platinum core locations. Similarly, the TEM-EDX line-scan shown in Figure 3.4(d) indicates the existence of partial core-shell structure for the three platinum cores highlighted by the arrows in the figure, as well as the presence of rhodium sulfide particles formed directly on the carbon substrate.

Full Core-Shell Catalyst (RhxSy@10%Pt/C)

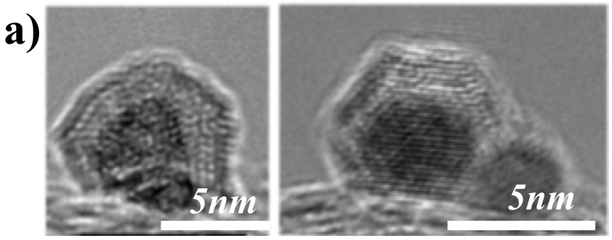

Partial Core-Shell Catalyst (RhxSy@10%Pt/C)

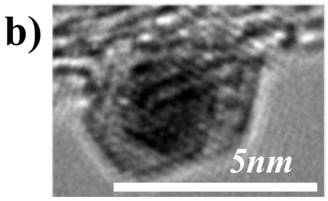

Full Core-Shell Catalyst (RhxSy@5%Pt/C)

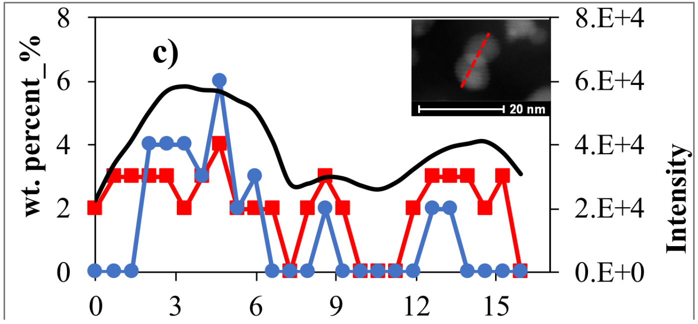

Partial Core-Shell Catalyst (RhxSy@5%Pt/C)

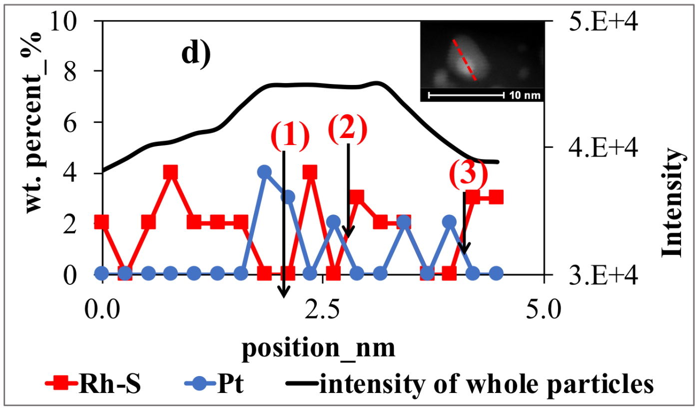

Figure 3.4. TEM micrographs and elemental profile by EDX for the core-shell structure

3.1.3 Rh_xS_y Catalyst Tests in Three-electrode System

While TEM can be used to determine the presence, or not, of core-shell catalyst, it cannot be used to determine the fraction of core-shell structure in the entire catalyst. For this, cyclic voltammetry was used to determine the electrochemical active surface area (ECSA) of the catalyst before and after soaking in an HBr solution, which will dissolve the platinum cores of catalyst particles with imperfect, or partial rhodium shell.[60] A new set of holder for the working electrode was developed. The traditional method to measure CV is by a rotating disk electrode (RDE).[61] By the RDE method, the weight of catalyst coated on the glassy carbon electrode can never be measured precisely because of the 4-order difference in the weight of a RDE (around 15 g) and the catalysts (less than 1 mg). The mass coated on the RDE often is calculated by the volume of the catalyst ink placed on the RDE, which is based on the assumption that the catalyst ink is perfectly uniform.[62,63] Another issue for the RDE method is its unsuitability for the durability test. The smooth surface of RDE cannot hold the catalyst powder for a long time. Thus, the decrease of ECSA in the durability test can be difficult to be differentiated as the corrosion or the falling-off effect of the coated solid catalyst. By the holder and GDE setup shown in Figure 2.1, these two drawbacks of the RDE method can be solved. First, the mass of catalyst coated on GDL can be measured accurately because of the low mass of the GDL, which provides the foundation to calculate the precise ECSA per mass of rhodium element. Second, the porous structure of GDE can minimize the effect of catalyst falling-off during the long duration of the durability test, making the durability test possible.

In this study, the initial ECSA of the catalyst coated on a GDL was measured. The GDE was then soaked in a 1M HBr solution at room temperature for a specified duration (35, 80 and 152 hrs), washed in hot DI water (this was found to be an effective way to remove the adsorbed bromide), and then retested for ECSA. The durability test can give us the sustainability of core-shell rhodium sulfide catalysts and exclude the unstable activity of exposed Pt core material to the catalysts. The results are shown in Figure 3.5. In Figure 3.5(a), for the CV of commercial Rh_xS_y catalyst, which is believed to be pure $Rh_{17}S_{15}$, a slight decrease in ECSA can be seen from the CV. This shows that the falling-off effect still exists though it has been significantly minimized. From the cyclic voltammetry in Figure 3.5 one can see that the ECSA of the core-shell catalyst decreases significantly after 35 and 80 hrs of soaking in HBr and that no significant decrease was observed between 80 hrs and 135 hrs. This observation can be explained as follows. The high initial ECSA can be attributed to the exposed platinum nanoparticle cores. The double oxidation peaks are also the signature of platinum surfaces.[64,65] After 80 hrs of soaking in HBr in which exposed platinum cores were removed, the remaining and stable ECSA can be attributed to the catalyst consisting platinum core/full rhodium sulfide shell particles.

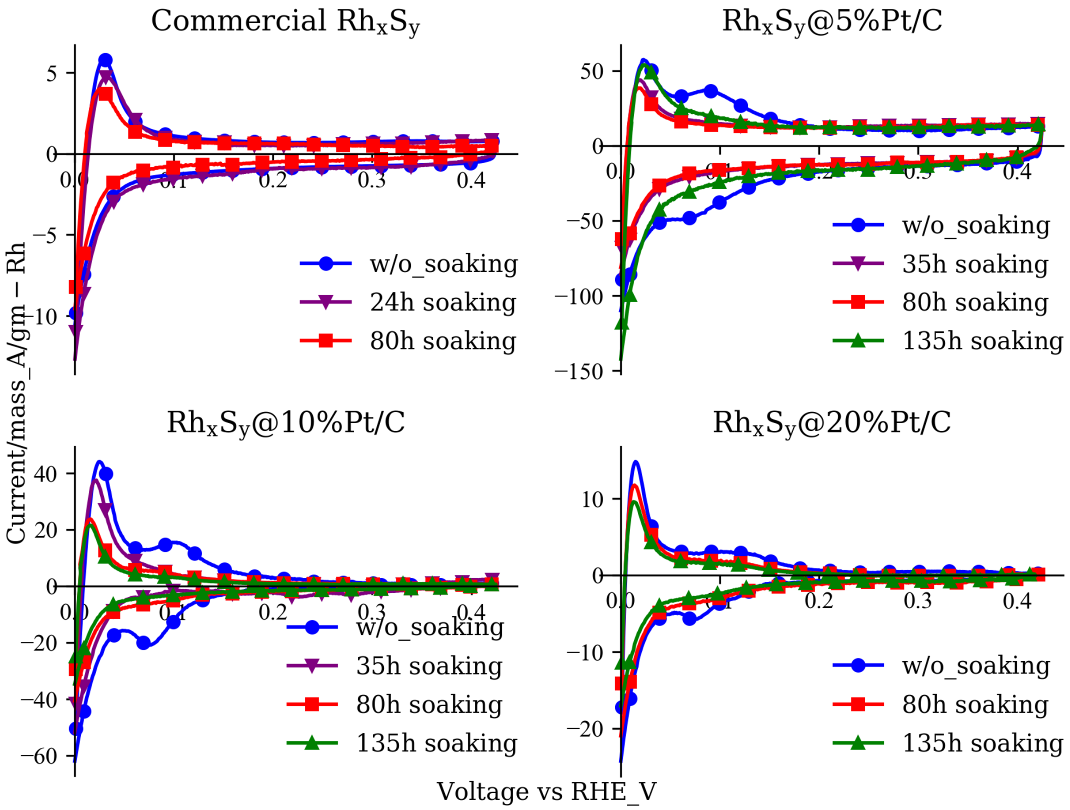

Figure 3.5. Durability test of core-shell catalyst and commercial catalyst by cyclic voltammetry (electrolyte: 1M N_2-saturated H_2SO_4 solution, working electrode: catalyst-coated GDE, counter electrode: Pt foil, reference electrode: SCE, scan rate: 10mV/s)

As mentioned in the experimental section, the ECSA is calculated as Pt equivalent. The mass-specific ECSA results given in Table 3.1 show that the core-shell rhodium sulfide catalysts have much greater mass specific active area than the commercial rhodium sulfide catalyst. The best group, the core-shell catalyst with 10% Pt/C, has more than 7 times the specific active area of the

Table 3.1. Mass-specific ECSA of core-shell and commercial rhodium sulfide catalysts

After 80hr 1M HBr soaking	ECSA_m^2/gm – Rh
Rh_xS_y@5% Pt/C	41
Rh_xS_y@10% Pt/C	50
Rh_xS_y@20% Pt/C	23
Commerical Rh_xS_y	6.9

commercial catalyst. This significant increase can be attributed to the small particle sizes of the core-shell catalyst that was achieved by using small and well-dispersed platinum core nanoparticles. The CV of different catalysts can be seen from Figure 3.6. The higher ECSA / mass of core-shell catalyst with 10% Pt/C compared to that with 5% Pt/C is due to the formation of more core-shell structures as more core materials are added, instead of forming the thicker shell on few cores and non-core-shell rhodium sulfide nanoparticles. The higher loading of Pt/C (20%), however, showed poor core Pt dispersion in the TEM of Figure 3.3(f), which resulted in increased shell thickness and lower rhodium utilization.

In Figure 3.6, what is worth pointing out is the significantly different capacitive current for different catalysts. Obviously, the Rh_xS_y@5%Pt whose carbon substrate is activated carbon has the highest capacitive current, and other catalysts whose carbon substrates are graphite carbon or XC72R have similar capacity currents. The higher specific surface area of activated carbon contributes to higher capacitive current.

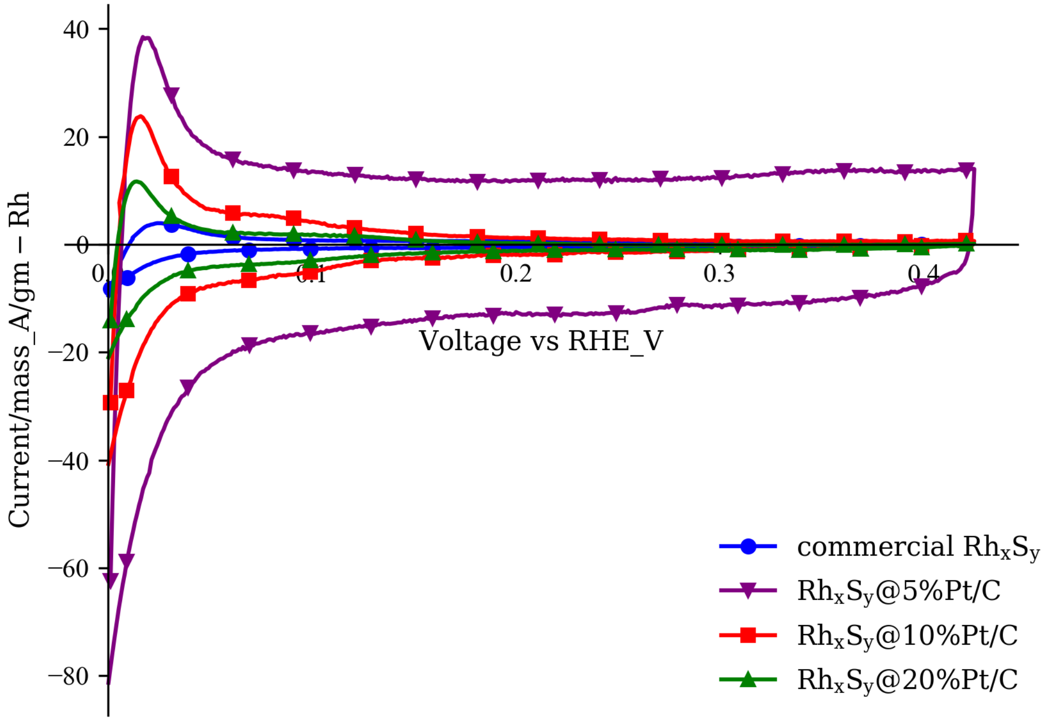

Figure 3.6. Cyclic voltammograms of catalysts after 80 hrs of 1 M HBr soaking (electrolyte: 1M N_2-saturated H_2SO_4 solution, working electrode: catalyst-coated GDE, counter electrode: Pt foil, reference electrode: SCE, scan rate: 10mV/s)

3.1.4 Rh_xS_y Catalyst Tests in H_2-Br_2 Fuel Cell

After the catalysts were tested in the three-electrode system by cyclic voltammetry, the performances of core-shell catalysts were evaluated in the fuel cell. The durability test in Figure 3.5 demonstrates that there are exposed platinum cores and presences of rhodium metal. Thus, the exposed platinum cores and rhodium metal formed during thermal treatment should be removed before the measurement of polarization curves for core-shell rhodium sulfide catalyst. Direct soaking the GDE of the negative electrode in the 1M HBr solution will make gas diffusion layer completely hydrophilic which may lead to water flooding and poor mass transport performance in the negative electrode.

In the fuel cell cycling test, the corrodible components were removed by the crossed-over HBr/Br_2 solution. Figure 3.7 shows the fuel cell cycling test. For rhodium sulfide catalysts with higher mass activities (Rh_xS_y@10%Pt/C and Rh_xS_y@20%Pt/C) and 30% Pt/C, the fuel cells were discharged at 80 mA until the voltage dropped to 0.3 V. The charge current was 80 mA for these three catalysts. Then the fuel cells were charged back to recover the active materials. Due to the mass transfer effects suffered by Rh_xS_y@5%Pt/C, which is shown later in Figure 3.8, a lower discharge current of 20 mA and cut-off voltage of 0.3 V were used. Similarly, for the commercial catalyst, the discharge current and cut-off voltage of 20 mA and 0.3 V respectively were used because of the low discharge current capability of the commercial RhxSy catalyst as shown in the Figure 3.8. The charge current was set at 60 mA for these two low active surface area catalysts.

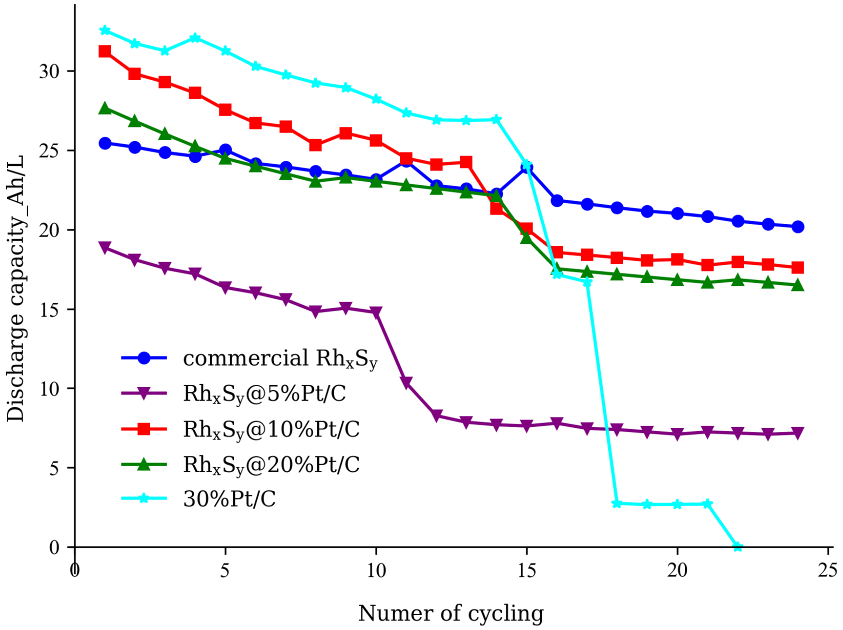

Figure 3.7. Cycling test for the hydrogen-bromine fuel cell (30% Pt/C, Rh_xS_y@10%Pt/C, Rh_xS_y@20%Pt/C: discharge current 80 mA, cut-off voltage 0.3 V; Rh_xS_y@5%Pt/C, commercial catalyst from BASF: discharge current 20 mA, cut-off voltage 0.3 V)

In the fuel cell cycling test, the fuel cell with platinum catalyst shows a sharp decrease in performance and finally dies once the platinum was removed entirely from the negative electrode.

The similar sharp decrease can be observed in the fuel cells with the core-shell catalysts. After the loss of corrodible materials, the fuel cells with core-shell rhodium sulfide catalysts show a stable discharge capacity. Due to the mass transfer effect in the electrode with RhxSy@5%Pt/C catalyst, this fuel cell reaches the cut-off voltage earlier resulting in a lower discharge capacity than those with other core-shell catalysts. The commercial catalyst from BASF consisting of pure $Rh_{17}S_{15}$ shows no initial loss in capacity and achieved a higher discharge capacity mainly because of lower discharge current (20 mA vs. 80 mA of core-shell catalyst) was used. The spikes in the Figure 3.7 are due to the replenishment of the catholyte.

After the discharge capacity reaches a stable state, the polarization curves of the core-shell catalysts were measured, and the results are shown in Figure 3.8. The polarization curves were full IR corrected to remove the effect of all ohmic resistances in the fuel cell including the resistance from the membrane. This full IR correction allows us to study the kinetics and mass transfer effects. Due to the corrosion of platinum in HBr/Br_2 solution, the discharge current of the fuel cell with platinum was near zero, and its results are therefore excluded in the Figure 3.8. For the rhodium sulfide catalyst, the charge performance is better than the discharge performance at the same overpotential. Note that for the HOR on bifunctional rhodium sulfide catalysts in the negative electrode, only the rhodium sites on the surface of the catalyst can catalyze the dissociation and oxidation of hydrogen molecules to hydronium ions. For the HER on rhodium sulfide in the negative electrode, however, both of the sulfur and rhodium sites on the surface can facilitate the catalytic reduction process of hydronium ions to hydrogen molecules.[66,67] The better charge performance can be attributed to the bifunctional characteristics of rhodium sulfide catalysts.

The primary purpose of this study is to select the best core-shell catalyst for future fuel cell optimization. The relatively low current density can be attributed to the very low loading of catalyst and unoptimized operation conditions, which will be optimized in future research.

The polarization curves in Figure 3.8 show that core-shell catalysts with 10% and 20% Pt/C as cores have much better performance in the discharge and charge operations. In the low potential region which is dominated by the kinetics loss, the kinetics performances of core shell catalysts

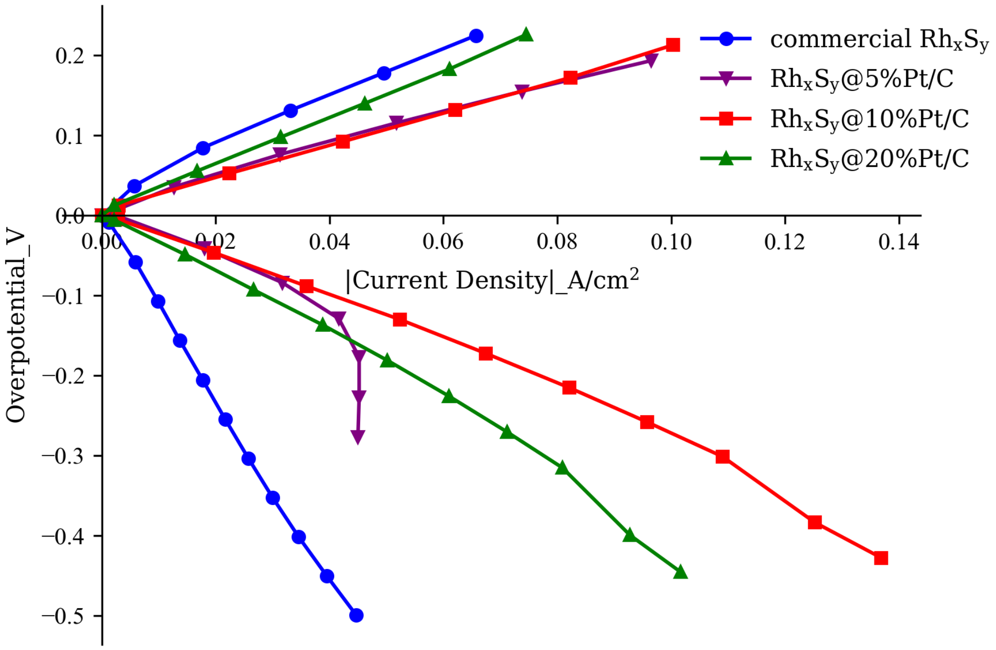

Figure 3.8. Polarization curve after 24 cycles of discharge and charge

from 5% Pt/C core to 10% Pt/C core are best compared with the commercial catalyst. Above 110 mA/cm^2 and 80 mA/cm^2 respectively, the effect of mass transport can be observed in the fuel cells with Rh_xS_y@10%Pt/C and Rh_xS_y@20%Pt/C catalysts. But for the fuel cell with Rh_xS_y@5%Pt/C catalyst, the mass transfer effect starts at about 40 mA/cm^2. The reason may be explained in the Figure 3.9.

The highest capacitive current observed in the cyclic voltammogram of Rh_xS_y@5%Pt/C catalyst in the Figure 3.6 indicates that the activated carbon used in 5% Pt/C has the highest surface area. Uchida et al. highlighted that the microporous structure of supporting carbon could have a negative effect on the catalyst utilization in a fuel cell operation.[68] For high surface area activated carbon, a large amount of catalyst particles is located inside the microporous structure of the catalyst/carbon agglomerates as shown in Figure 3.8 and may not be as accessible for the hydrogen reactions. The long diffusion length for the reactive species in the hydrogen reactions in the micro-channels may result in higher mass transport effect in the fuel cell especially at high current densities. It can be addressed by changing the carbon support from activated carbon to XC72R which has larger pore sizes.

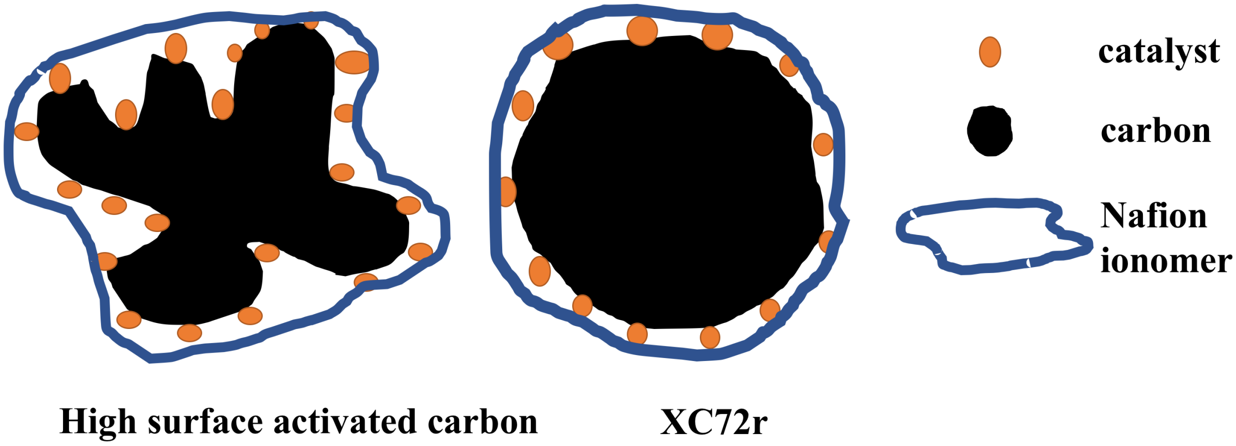

Figure 3.9. Schematic demonstration of distribution of platinum particles on different types of carbon substrate

3.1.5 Cheap Metal Material as Core Material

The concept of the core-shell structure has been validated by Pt as the core material and Rh_xS_y as the shell. It has also proved that the core-shell structure is an effective method to improve the mass-specific surface area though not all the shells are integrated. After the preliminary research, the cheaper metal, Ni/C, was used as a core material to reduce the cost of the catalyst. The nickel NPs on activated carbon were from Dr. B.J. Hwang of National Taiwan University of Science and Technology. The synthesis method of Rh_xS_y@20%Ni/C is similar to that of rhodium sulfide@Pt/C.

After the synthesis, the Rh_xS_y@20%Ni/C was tested by the cyclic voltammetry, and the results are shown in the Figure 3.10. It is obvious that the Rh_xS_y@20%Ni/C has lower HOR/HER activity.

The ECSA/mass calculated from the CV for the Rh_xS_y@20%Ni/C is only 2.3 $m^2/gm-Rh$ which is even lower than that of non core-shell catalyst. The small size of HOR and HER peaks in the CV indicates that the composition of Rh_3S_4 and $Rh_{17}S_{15}$ on the surface is limited.

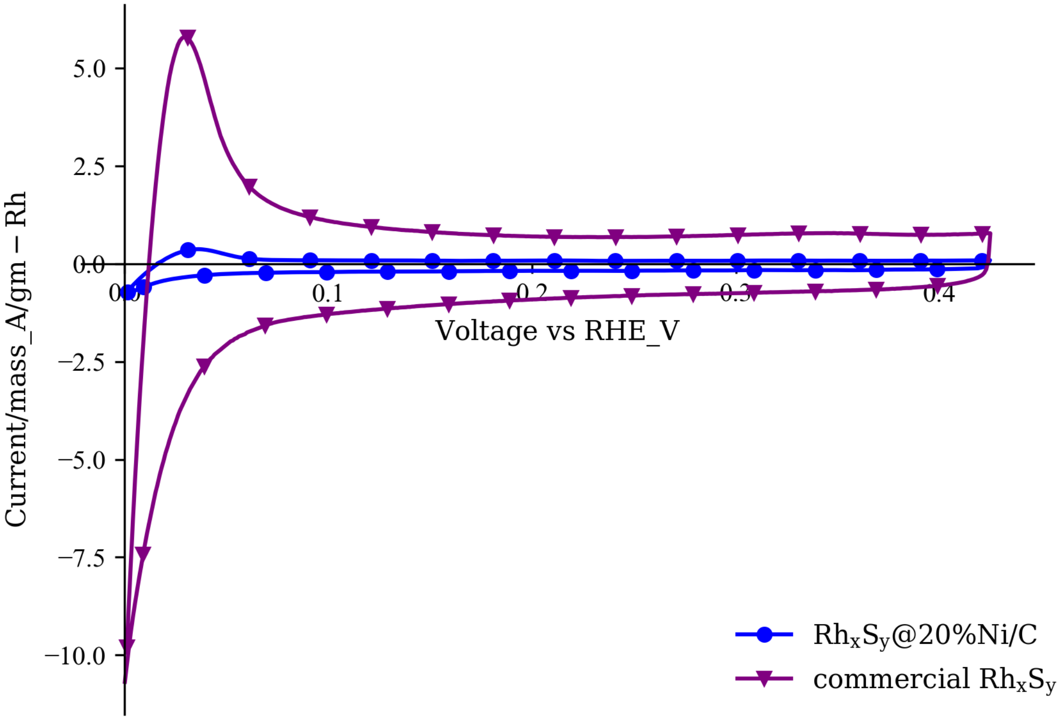

Figure 3.10. Cyclic voltammetry of Rh_xS_y@20%Ni/C (electrolyte: 1M N_2-saturated H_2SO_4 solution, working electrode: catalyst-coated GDE, counter electrode: Pt foil, reference electrode: SCE, scan rate: 10mV/s)

The reason for the low mass-specific of Rh_xS_y@20%Ni/C may be explained in the Figure 3.11. The pH of the $RhCl_3$ solution which is the source of rhodium in the synthesis is determined by the dissociation of the rhodium (III) chloride hydrate ($RhCl_3 \cdot 3\,H_2O$). A Rhodium cation is considered to be a 'soft' coordination center that prefers 'hard' ligand like water and hydroxide.[69,70] The ligand exchange of chloride with water and the subsequent deprotonation of the ligand water make the synthesis solution acidic. The pH of the synthesis solution measured was around 1.2. In an acidic solution, nickel NPs can be dissolved to be Ni^{2+} which can also be precipitated by the S^{2-}

to form NiS. After the precursor synthesis step, the surface of precursor NPs is mixed with Rh_2S_3 and NiS which cannot catalyze the HOR even after the thermal treatment. The instability of cheap metal like Ni and Co in the acidic $RhCl_3$ solution make them impossible to be used as core material. Even the silver which is stable in the acidic solution with the bulk form is corrodible as the form of the nanoparticle. The try to synthesize the Rh_xS_y as shell and cheap metal as core material failed finally. While other cheap metal cores might work, we decided to try a different approach.

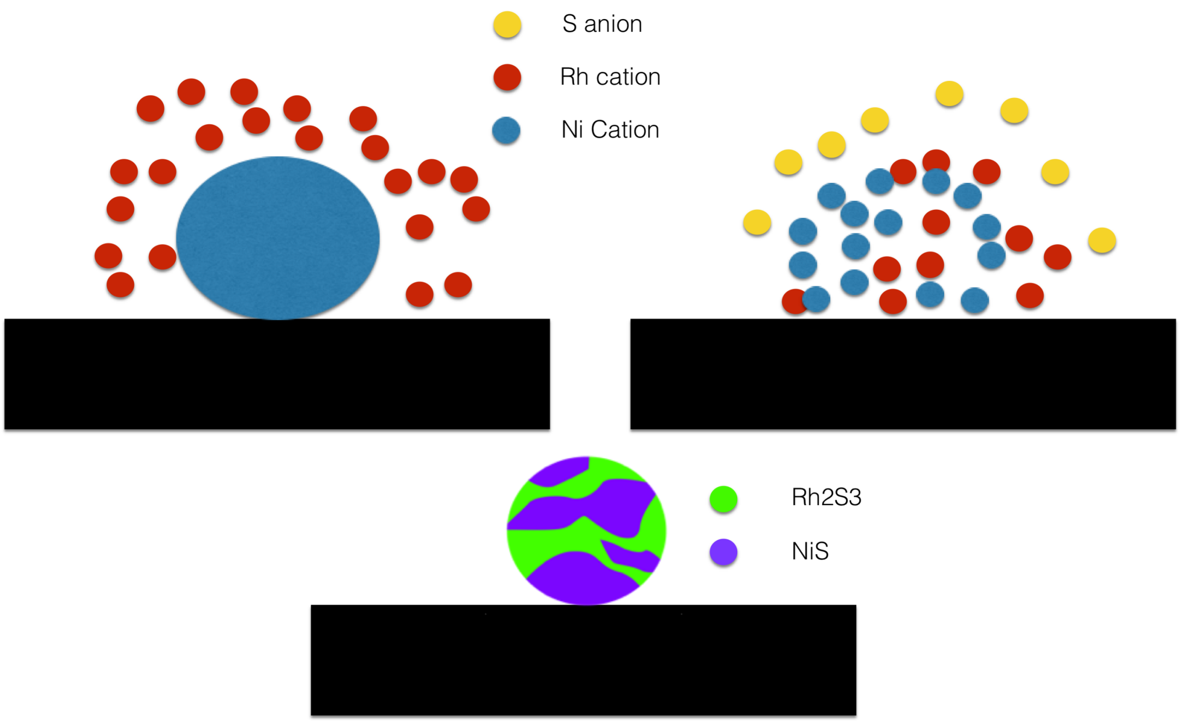

Figure 3.11. Mechanism of Ni as core material and Rh_xS_y as shell material

3.1.6 Summary

Core-shell rhodium sulfide catalysts using platinum nanoparticles on carbon substrate as cores were synthesized. The materials were characterized by XRD, TEM, EDX, and XPS. The durability test for the core-shell catalysts with fast/slow temperature ramp reminds the significance of selection of temperature ramp especially for the core-shell catalyst synthesized with high-temperature thermal treatment. This finding is believed to have a positive enlightenment on the research of other core-shell catalysts. The results of TEM including EDX confirm the formation of core-shell catalysts. TEM results show the existence of platinum cores with both complete and partial rhodium sulfide shells as well as non-core rhodium sulfide catalysts on the carbon substrate. These results were validated by the ECSA results obtained of these catalysts before and after they were soaked in HBr solution, to remove uncoated or partially coated platinum cores, showing a significant decrease in ECSA in the first 80 h followed by a stable ECSA after 80 h. This work shows that high mass-specific surface area core-shell rhodium sulfide catalysts using small and well-dispersed platinum nanoparticles on carbon as a metal core were achieved. The core-shell rhodium sulfide catalyst synthesized with 10% Pt/C has mass specific active area seven times that of the commercial catalyst. A new method based on using a carbon gas diffusion layer as the support and a fixture was also developed to allow accurate mass specific ECSA of solid catalyst to be measured and long-term soaking durability test to be conducted. The stability and improved HOR/HER performance of core-shell rhodium sulfide catalyst were also demonstrated in the reversible hydrogen-bromine fuel cell. In the future study, the same type of carbon substrate with more accessible porous structure will be used for the core material. The cheaper materials like Ni/C instead of platinum as core materials were also explored. The corrodible nature of Ni in the acidic solution, however, makes this attempt unsuccessfully. The Ni NPs were dissolved by the acidic $RhCl_3$ solution and then the Ni cations were precipitated by the sulfide ions at the same time with the precipitation of Rh cations. The nickel sulfide on the surface of the catalyst without HOR/HER catalysis finally decreases the ECSA. Though the attempt to use cheap metal as core material failed, the rhodium sulfide as shell and platinum as the core material is still an excellent choice to improve the mass-specific surface area of electrocatalyst in the hydrogen-bromine fuel cell. Moreover, the price of Pt is around 826 USD/oz while that of Rh is 2,575 USD/oz. The core-shell structure with Pt material still reduces the cost of the electrocatalyst, even though the catalyst does not count for a significant part in the cost of the whole H_2-Br_2 fuel cell.

3.2 Pt-doped Rh_xS_y Catalyst

It has been observed that the atoms in the core material may diffuse to the shell or vice versa.[71] The covalent atom radius of Pt is 128 pm while that of Rh is 135 pm. The similar atom radius provides the possibility to dope Pt atom in the crystal structure of Rh_xS_y. After the doping, Pt may be coordinated with surrounding sulfur atoms which can offer the protection to the corrodible platinum. Moreover, compared to Rh, Pt is more active in catalyzing HOR/HER.[72] Then it is assumed that the Rh_xS_y catalyst may have a better activity for HOR/HER catalysis with some Rh sites replaced by Pt. The improvement in the activity or durability of the catalyst by doping a secondary metal can be found in the development of ORR catalysts like Pt-Ni or Pt-Mo.[73] The core-shell catalyst study mentioned above didn't conduct any research on the diffusion of Pt atoms in the shell material due to the time limitation. Then Rh_xS_y was doped by Pt artificially during synthesis to check whether the activity of HOR/HER can be enhanced or not.

Figure 3.12 shows the CV of Pt-doped rhodium sulfide without and with corrosive HBr soaking. The doublet HOR peak of initial CV of Pt-doped rhodium sulfide indicates the existence of metallic platinum, which is similar with the initial CV of core-shell rhodium sulfide catalyst. The decrease of HOR/HER peak after HBr soaking validates that there is corrodible platinum. After all the detached Pt sites are corroded by HBr, the mass-specific surface area is even lower than that of the commercial Rh_xS_y. The reason is from the calculation method of mass-specific ECSA. The initial mass of catalyst was used for all the ECSA/mass calculation. After the detached Pt was corroded, the mass of catalyst loaded on the GDE was reduced. If the initial mass of catalyst is still used, then the ECSA/mass is supposed to be lower since the denominator is larger than the real mass. The unstable ECSA performance indicates the failure of doping of Pt in the Rh_xS_y catalyst. The segregation of Pt and Rh_xS_y in the crystallization process at high temperature may contribute to the formation of metallic Pt. The similar detachment of Ni and Fe in the nickel-iron oxide catalyst has been reported by Dr. Kevin Leonard's group.[74] In the future, the microwave-assisted method may be applied to convert the precursor Rh_2S_3 to the active phases Rh_3S_4 and $Rh_{17}S_{15}$ without high-temperature thermal treatment.[75,76]

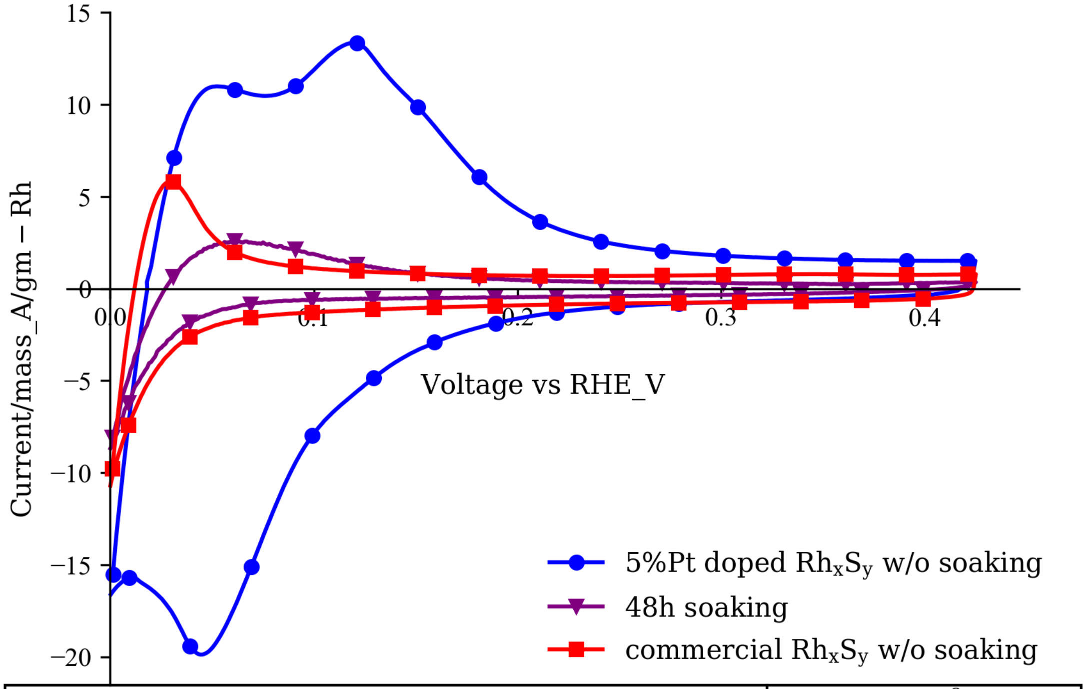

Catalyst	ECSA/mass_m^2/gm − Rh
5%Pt doped Rh_xS_y without soaking	78.1
5%Pt doped Rh_xS_y with 48h soaking	8.7
commercial Rh_xS_y without soaking	9.2

Figure 3.12. Cyclic voltammetry of Pt-doped rhodium sulfide catalyst without and with HBr soaking (electrolyte: 1M N_2-saturated H_2SO_4 solution, working electrode: catalyst-coated GDE, counter electrode: Pt foil, reference electrode: SCE, scan rate: 10mV/s)

3.3 Synthesis and Evaluation of Rhodium Sulfide Catalyst from $(NH_4)_2S_2O_3$ with Functionalized Carbon for HOR/HER in H_2-Br_2 Reversible Fuel Cell

Rhodium sulfide was found to be a suitable catalyst for the HER/HOR in the corrosive HBr and Br_2 solution, yet the rhodium sulfide catalysts used in those studies had low mass-specific specific surface area because of their large catalyst particle sizes. Functionalized supporting materials like carbon have been used to reduce the particle size in the synthesis of other types of catalysts.[77,78] Functionalization can make carbon hydrophilic and create more active sites by introducing basic/acidic functional groups on the carbon surface.[79] The oxygen functional groups shown in Figure 3.13 enhance the adsorption of rhodium cations which can then serve as nucleation sites for the particle growth. Metal cation adsorption on a carbon surface can occur via two types of mechanisms: formation of the surface metal complex (inner-sphere) or ion exchange (outer-sphere)[63] or Cπ interaction.[80,81,82] These mechanisms and how they play a role in the deposition and formation of rhodium sulfide particles will be discussed next.

Although the functionalized carbon can increase the distribution and decrease the particle size of the catalyst, it may impose extraordinary influence on the electrode performance during the fuel cell's operation. Functionalizing carbon introduces new surface functional groups such as carboxylic or ketone groups that have different affinities for the Nafion ionomer used in the catalyst layer of a fuel cell electrode. Figure 3.14 (replotted from the research of Okada et al.[47]) shows the adsorption of organic chemicals with carboxylic and ketone group on Nafion. Quartz crystal microbalance (QCM) is used to detect the mass change of Nafion loaded on the crystal surface. The adsorption is indicated by frequency shift (ΔF). In the Saurbrey's equation,[83] $\Delta F = -2.310^6 f_0^2 \Delta M/A$, where ΔM is the mass change on the QCM. Figure 3.14 indicates that the chemical with the carboxylic group has much higher adsorption on the Nafion at the similar concentration compared to the chemical with ketone group, which proves the excellent affinity between the Nafion and carboxylic group. A good affinity between Nafion ionomer and specific

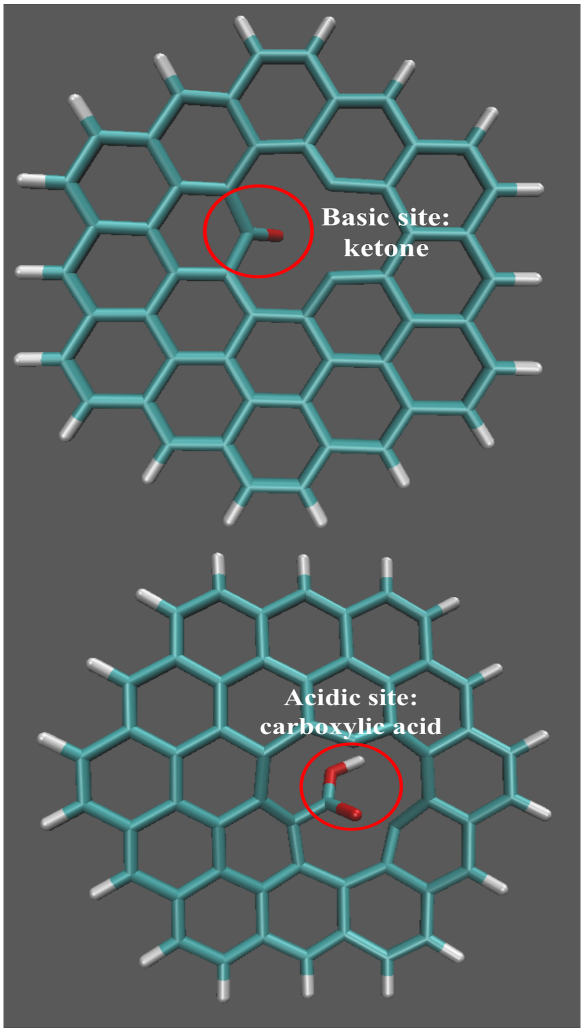

Figure 3.13. Functional groups on the activated carbon surface

surface function group leads to a better distribution of ionomer on the catalyst particle surface. In Xie et al.'s research, the aggregate geometry of the mixture of Nafion ionomer and carbon with Nafion-friendly group is 2.7 times larger than that of the mixture of Nafion and carbon with Nafion-unfriendly functional group.[84] The smaller Nafion-carbon aggregate indicates the worse affinity due to the repulsion between the carbon and Nafion. The performance of fuel cell with catalyst on Nafion-friendly carbon was also improved.[85]

In a fuel cell, HOR/HER only occurs on the catalyst surface that is in contact with the Nafion ionomer which provides the ionic conductivity and connectivity between the different catalyst sites in the electrode and the fuel cell polymer electrolyte membrane. While the average catalyst particle size and catalyst loading determine the number of sites available for reaction, the distribution of electrolytes on the carbon surface determines the catalyst area that is actually utilized during operation in the fuel cell electrode. The catalyst surface that is not accessible to the hydronium ions is not utilized and essentially wasted in a fuel cell.

In the following section, the effects of functional groups to the size of NPs and Nafion distribution are discussed.

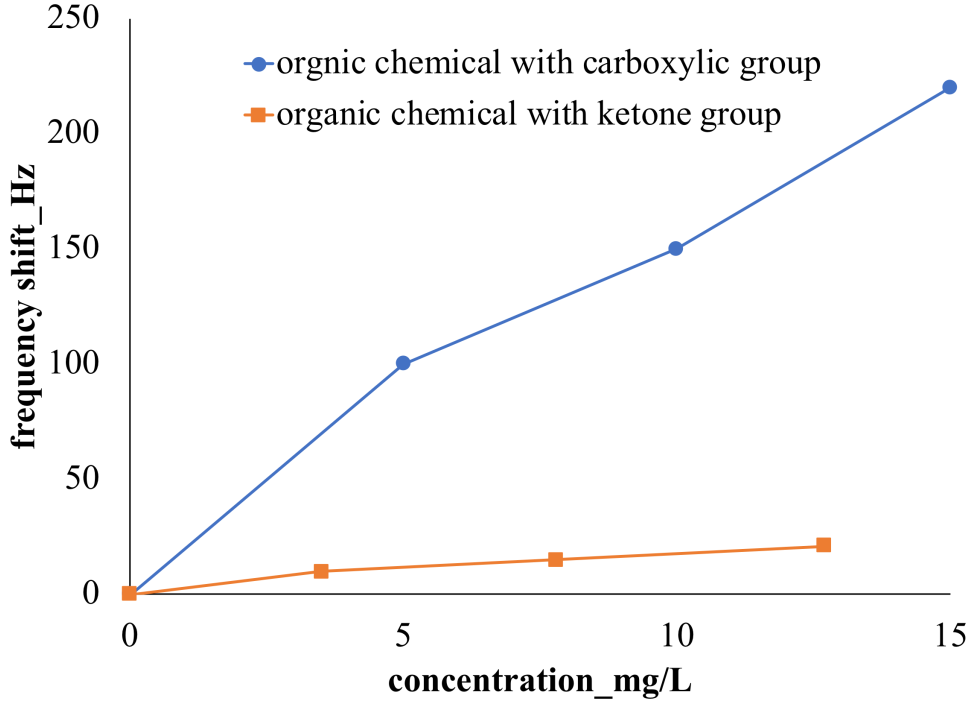

Figure 3.14. Effect of different organic chemicals on frequency response of Naifon-coated quartz crystal microbalance (QCM)

3.3.1 Functionalization of Activated Carbon

3.3.1.1 Functional groups on the carbon surface

Since the functional groups are oxygen-containing groups, the atomic percentage of oxygen can indicate the number of functional groups on the surface of the carbon. Figure 3.15(a) shows the change in the atomic percentage of oxygen during the functionalization process. The initial low value of oxygen percentage in the untreated carbon shows that the surface of the carbon was almost free of the functional groups. After oxidation in the concentrated HNO_3 solution, a large number of carboxylic groups were created on the surface of the XC72R-HNO_3 carbon material. The material's atomic percentage of oxygen increases from 0.88% before treatment to 9.74% after treatment. Reduction in H_2 at 300°C converts the sites with carboxylic groups to oxygen-free sites on the carbon surface. The subsequent air exposure converts these oxygen-free sites to the basic ketone groups.[86] As the functional groups change from $-COOH$ to $-C=O$, the oxygen atomic percentage decreases as shown in Figure 3.15(a). The XPS results in Figure 3.15(a) show that pretreatment creates oxygen functional groups on the carbon surface which will facilitate the Rh cation adsorption by serving as adsorption centers or enhancing the $C\pi$ interaction. The type of chemical functional groups can be analyzed by FT-IR. The main differences between the carbon surface with ketone and carboxylic groups on FT-IR spectra are located at 668 nm and around 2300 nm which can be assigned to the COO^- bending and $O-H$ stretch from strongly hydrogen-bonded $-COOH$ respectively.[86,87] The FT-IR results in Figure 3.15(b) validate that the functional group on the XC72R-HNO_3 carbon material consists of mostly the carboxylic surface group while the surface of the XC72R-HNO_3-H_2-Air carbon material is dominated by the ketone group.

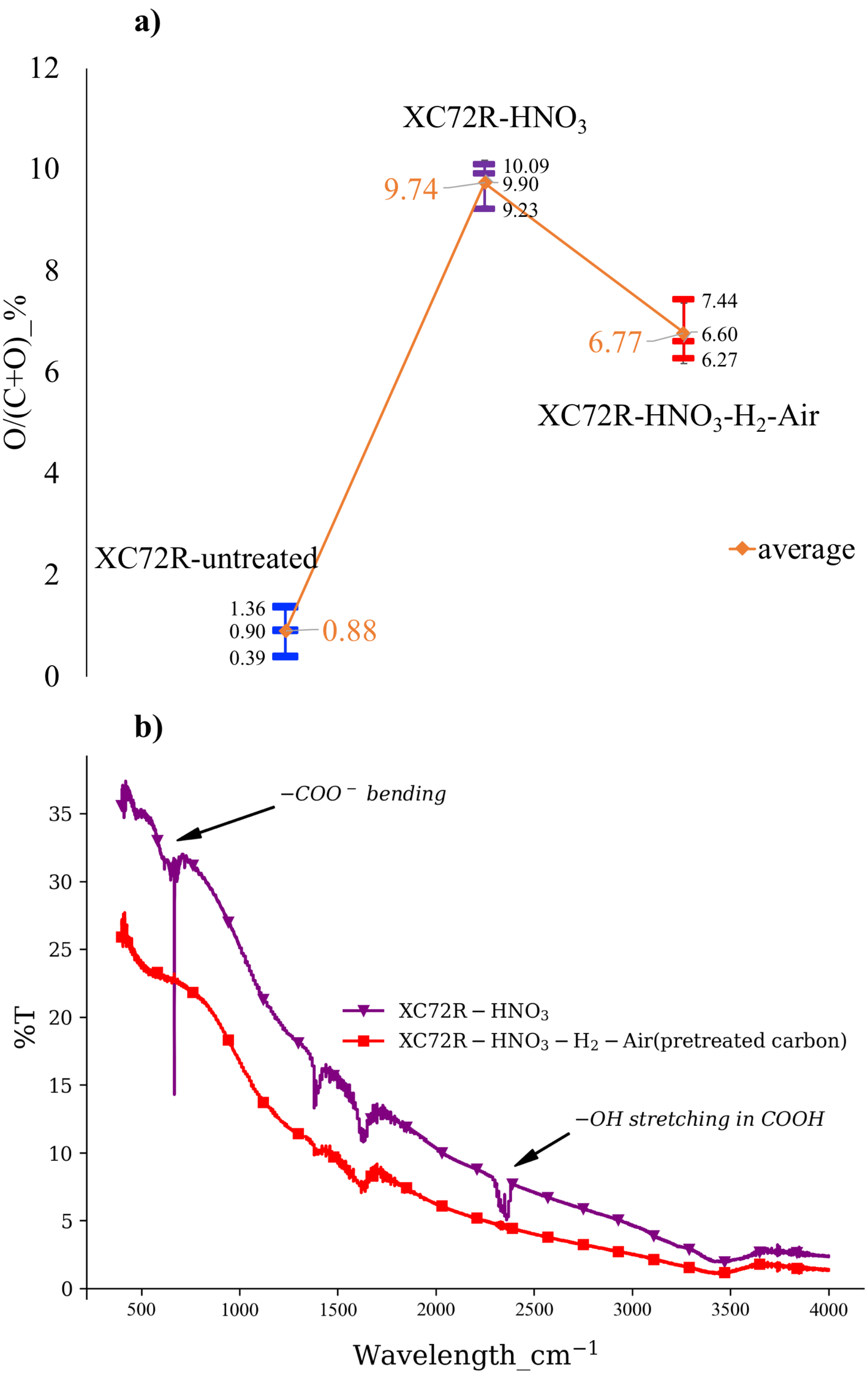

Figure 3.15. Characterizations for the supporting carbon (a) XPS of oxygen atomic percentages for supporting carbons (b) FT-IR spectra of carbon materials with different surface functional groups

3.3.1.2 Types of functional groups vs. functionalization time and oxidation agent

The oxidation agent and time affect the type and amount of surface sites. In the work of synthesis of catalyst on pretreated carbon, 70% HNO_3 was used as an oxidation agent. The activated carbon was heated in the nitric acid for 8 h. The XPS results in the Figure 3.15 show that there is 9.74% oxygen, while the FT-IR reveals the nature of those oxygen-containing group as the carboxylic group. In another research which is not disclosed in this dissertation, different oxidation agent and reaction temperature were used for the graphite carbon functionalization. The graphite carbon which has a similar chemical structure to activated carbon was oxidized in a solution of mixed concentrated H_2SO_4 (98%) and concentrated HNO_3 (70%) at a certain temperature with different oxidation times. The molar ratio of the two acids and the oxidation time are not disclosed here. The XPS results in the Table 3.2 shows that the amount of oxygen functional group is significantly larger than that of activated carbon functionalized in hot nitric acid significantly (9.74% vs. 17.9 % of T+3 h functionalization). Moreover, the nitrogen-containing and sulfur-containing groups are found in the graphite carbon treated by the mixed concentrated acids, which are absent in the carbon with pure nitric acid pretreatment. With the increase of functionalization time in the mixed concentrated acids, the oxygen percentage increases from 8.1% of T+1 h sample to 23.8% of T+4 h sample and then decrease to 19.1% of T+5 sample.

Table 3.2. Compositions of elements in the graphite carbon with different functionalization time by XPS (T is an undisclosed time)

Element	T+1 h	T+2 h	T+3 h	T+4 h	T+5 h
O	8.1	18	17.9	23.8	19.1
N	0.8	0.5	0.8	2.6	1
S	0.3	0.9	0.6	1.1	0.6
C	90.8	80.5	80.8	72.5	79.4

The nitrogen-containing functional group is supposed to be from the nitration reaction as shown in Figure 3.16.[88] The concentrated sulfuric acid serves as catalyst and water adsorber. The typical surface groups on the carbon are the sulfonic acid group, sulfoxide and sulfone groups. In the Table 3.2, the contribution to the total functional groups from the nitrogen-containing and sulfur-containing groups is negligible compared to that from the oxygen-containing group. Then more efforts were invested in the relationship of types of oxygen functional groups and functionalization time.

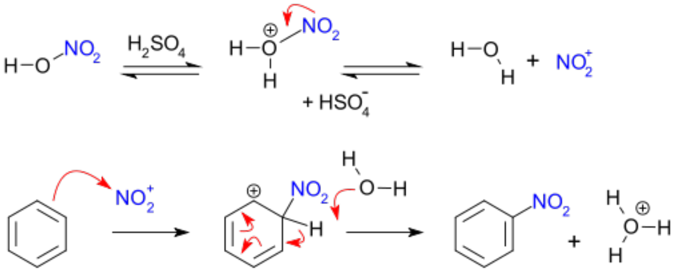

Figure 3.16. Schematic of nitration reaction
(By V8rik at English Wikipedia, CC BY-SA 3.0,
https://commons.wikimedia.org/w/index.php?curid=7890643)

In Figure 3.17, the graphite carbon with T+1 h shows the weak characteristic peaks of ketone group (blue curve with circle symbols), and then the characteristic peaks of the carboxylic group show up on the sample of functionalization with T+3 h (purple curve with triangle markers). Finally, they disappear after another 2 h functionalization (red curve with square symbols). This experiment result shows that the type of functional group on the carbon surface is sensitive to the reaction temperature, oxidation agent, and functionalization time. The ketone group is created on the carbon surface, which serves as the starting point to the carboxylic group by adding one oxygen. The carboxylic group can be further oxidized to CO_2 by losing one H. The generation of gaseous CO_2 indicates the destruction of carbon textural property. Then another round of oxidation from ketone to CO_2 starts on the new surface. The similar founding was also reported in the research of functionalization of multi-wall carbon nanotube (MWCNT).[89] In the future, the mixed concentrated acids may be used as the oxidation agent for the functionalization of activated carbon as supporting material of catalyst to save the reaction time.

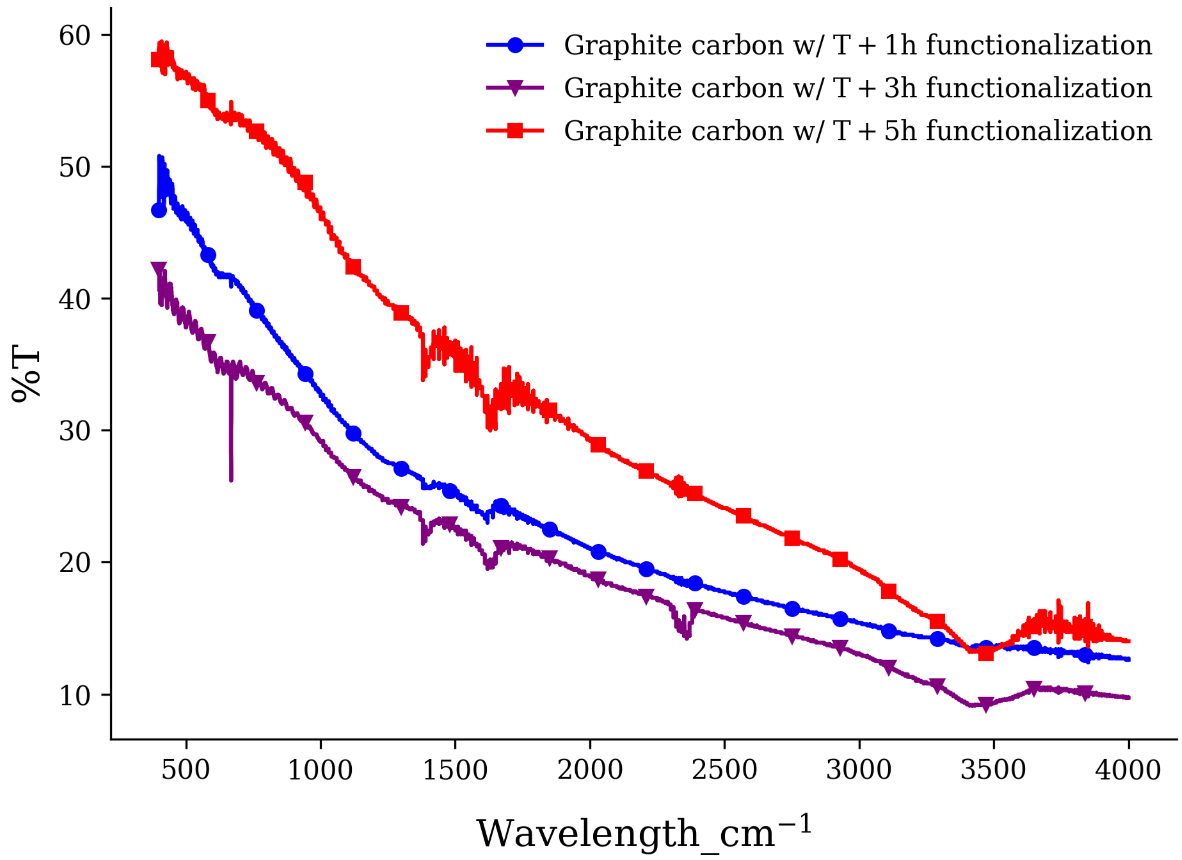

Figure 3.17. FT-IR spectra of carbon material with different functionalization times in mixed concentrated H_2SO_4 and concentrated HNO_3

3.3.1.3 Adsorption mechanisms of cation on different functional groups

The acidic surface functional groups, like carboxylic groups, are the main active sites for either the ion exchange or the formation of surface metal complex, while, by the $C\pi$ interaction, the electron-rich conjugated structures, like aromatic rings on the carbon surface, are the main adsorption sites for the adsorbent with the basic surface functional groups. The prerequisite for the ion exchange and formation of the surface metal complex depends on either the electrostatic affinity between the cations and negatively charged adsorption sites of oxygen functional groups or that between the anions and the positively charged adsorption sites of oxygen functional groups. For the basic functional groups, or after the acidic surface functional groups are converted into the basic groups, the $C\pi$ interaction becomes the main mechanism of adsorption. The $C\pi$ interaction develops from the interaction between the electron-deficient cation and electron-rich carbon surface which is enhanced by the lone electron pair of the basic surface group as shown in Figure 3.18. Because the main adsorption sites are conjugated structures rather than carboxylate ions, the $C\pi$ interaction does not rely on the electrostatic affinity between the ion and the adsorbent. Since the $C\pi$ interaction relies on the enhancement of electron cloud of conjugated structures of carbon surface from the lone electron pair of the basic surface groups, the existence of electron-withdrawing groups like carboxylic groups hurts the density of electron cloud of conjugated structures, which impairs the $C\pi$ interaction. Next, the adsorbent's state of charge is determined by the pH of the solution and the point of zero charge (PZC) of the adsorbent.[90] When the PZC < pH, the surface adsorbent is negatively charged, and, conversely, the adsorbent is positively charged when the PZC > pH. From the two mechanisms above and the relationship between the PZC/surface charge and the solution pH of the adsorbent, it can be inferred that when the surface functional groups are dominated by the acidic groups, Rh cation is attracted to the adsorbent (as carboxylate anion) when it is negatively charged or when PZC < pH. Furthermore, due to the $C\pi$ mechanism, which does not depend on the electrostatic affinity, the Rh cation is attracted to the carbon surface with the basic surface groups regardless of whether the PZC is higher or lower than the solution pH.

Selection of mechanism of cation adsorption is determined by the point of zero charge (PZC) and the pH of the solution. PZC is achieved when the electrical charge density on a surface is zero. PZC is usually given in the literature as the pH value at which an adsorbent submerged in an electrolyte exhibits zero net electrical charge. The PZC of the carbon surface with carboxylic functional groups is 3-4, yet the carbon surface with ketone functional groups is 9-10.[81,82,87,91] The adsorption mechanism of Rh cation is illustrated in the Figure 3.18. The electron cloud density in the Figure 3.18(a) is concentrated by the lone pair of electron of the ketone group, which facilitate the adsorption of electron-deficient rhodium cation. When the carbon surface is negatively charged (PZC < pH), the positively charged metal cation can be adsorbed via the inner-sphere/outer-sphere interaction between the cation and functional group as shown in Figure 3.18(b). The positively charged oxygen-containing functional group obviously repels the metal cation, which plays a negative role in adsorption.

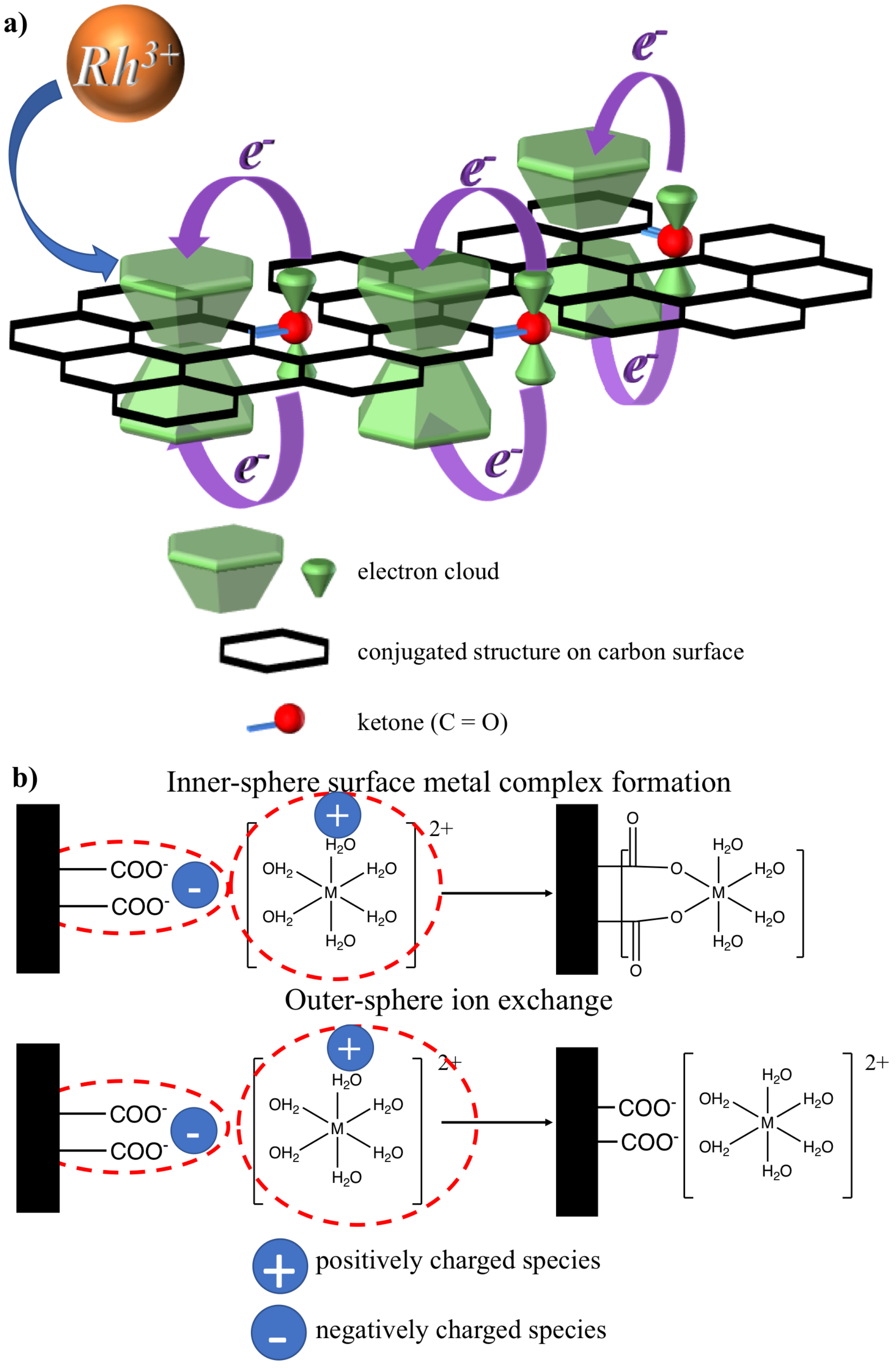

Figure 3.18. The mechanisms of cation adsorption a) with the ketone group on the carbon surface via Cπ interaction where the adsorption sites are the electron clouds of conjugated structures on carbon surface b) with the carboxylic group on the carbon surface via inner-sphere/outer-sphere interaction where the adsorption sites are the oxygen-containing groups

3.3.1.4 Adsorption mechanism for the functionalized carbon in the $RhCl_3$ solution

The main charged sites on the carbon surface are the oxygen functional groups like carboxylic acid and ketone group.[92] The pH of the solution in the synthesis is determined by the dissociation of the rhodium (III) chloride hydrate ($RhCl_3 \cdot 3\,H_2O$). A Rhodium cation is considered to be a 'soft' coordination center that prefers 'hard' ligand like water and hydroxide.[69,70] The ligand exchange of chloride with water and the subsequent deprotonation of the ligand water make the synthesis solution acidic. The pH of the synthesis solution measured was around 1.2. Based on the PZC of the adsorbent and the pH of the solution, it can be inferred that both of the carbon with carboxylic groups and the carbon with ketone groups are positively charged. As discussed in the introduction section, the positively charged carbon surface with the carboxylic group can only adsorb anion while the carbon surface with ketone group can adsorb Rh cation by the $C\pi$ interaction. The interaction between the electron-rich conjugated structures of carbon and the electron-deficient cations is not interrupted by the positively charged functional group sites.

The mass-specific ECSA of the various treated carbon groups in Figure 3.19 confirms this hypothesis. It shows that the ECSA/mass of the rhodium sulfide catalyst with XC72R-HNO_3-H_2-Air carbon is the highest, more than 2 times higher than that of the rhodium sulfide catalyst on untreated carbon. This high mass-specific ECSA can be attributed to more efficient adsorption of the Rh cation on the carbon surface dominated by the ketone group due to the $C\pi$ interaction.The lone pair of oxygen electrons in the ketone group enhances the electron clouds of conjugated structures on the carbon surface, facilitating the adsorption of electron-deficient Rh cation. The mass-specific ECSA of rhodium sulfide on XC72R-HNO_3 carbon substrate is even lower than that of the rhodium sulfide on untreated carbon. This validates that the positively charged carboxylic surface group has a negative effect on the adsorption of the metal rhodium cation. The electrostatic repulsion between the carboxylate ions and the rhodium cations prevents the adsorption of rhodium cation on the sites of oxygen functional group on the carbon surface by the ion exchange and formation of the surface complex. Furthermore, the abundance of carboxylic groups impairs the electron-rich region for the $C\pi$ interaction with rhodium cation due to the electron-withdrawing nature of carboxylic groups compared to the untreated carbon without functional groups. For the remainder of this paper, the terms functionalized carbon or pretreated carbon represent the XC72R carbon with the ketone surface group as the surface dominant functional group.

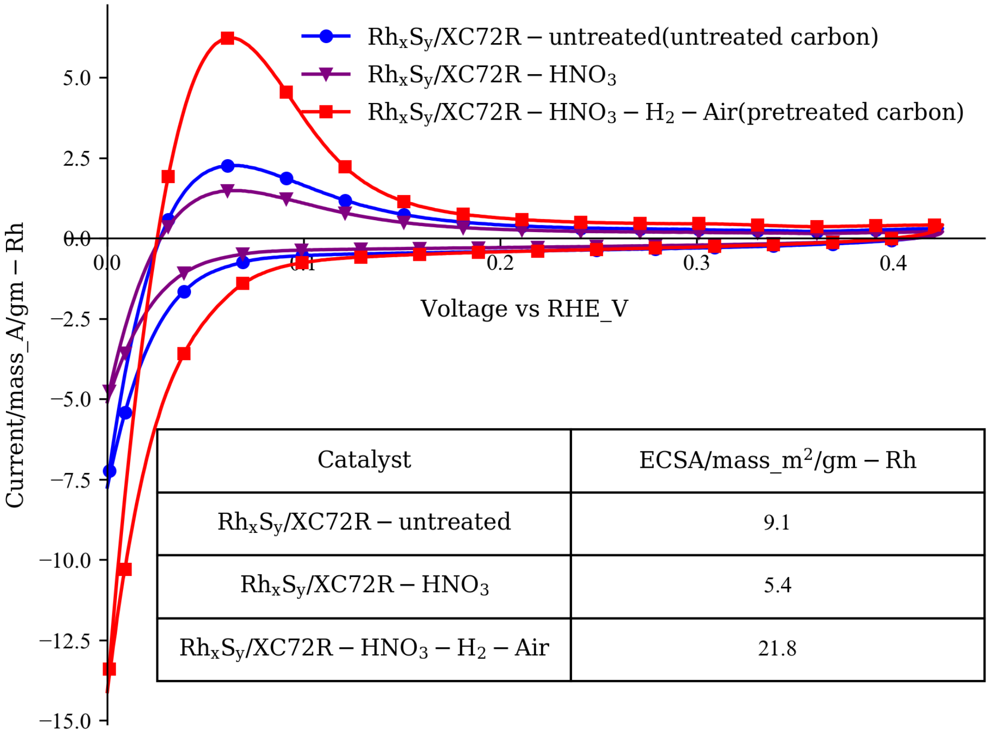

Catalyst	ECSA/mass_m^2/gm − Rh
$Rh_xS_y/XC72R-untreated$	9.1
$Rh_xS_y/XC72R-HNO_3$	5.4
$Rh_xS_y/XC72R-HNO_3-H_2-Air$	21.8

Figure 3.19. Cyclic voltammograms of rhodium sulfide on different carbon substrates (electrolyte: 1M N_2-saturated H_2SO_4 solution, working electrode: catalyst-coated GDE, counter electrode: Pt foil, reference electrode: SCE, scan rate: 10mV/s)

Rhodium cation adsorption on the carbon with the carboxylic surface group may be carried out by increasing the pH of the rhodium chloride solution from 1.2 to a value larger than the PZC of adsorbent. In Figure 3.20(a), the pH of rhodium chloride solution was adjusted to be nearly neutral by the ammonia water. The initial pH (1.1) was increased to around 6 in 30 min. The Rh_xS_y with pH adjustment, however, shows an extremely low mass-specific ECSA in Figure 3.20(b) compared to that of Rh_xS_y without neutralization in the synthesis. The low ECSA/mass of catalyst with neutralization may be attributed to the precipitation reaction of Rh cation and hydroxide anion, which leads to a significant loss of the expensive rhodium source in the solution.[93] Based on this consideration, the conversion of the carboxylic group to the ketone group on the carbon surface rather than the adjustment of pH of the rhodium chloride solution was chosen.

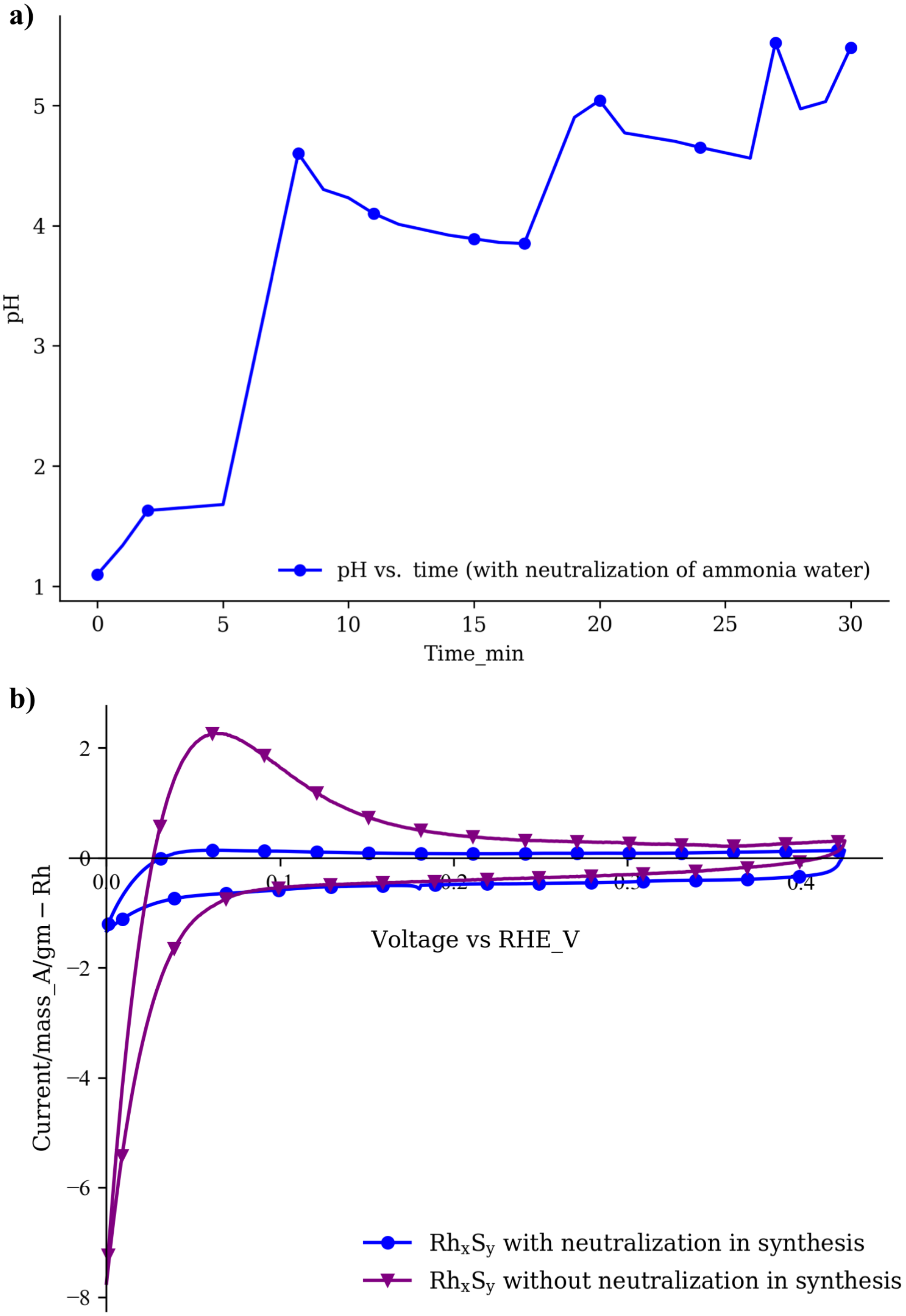

Figure 3.20. pH adjustment in the synthesis of rhodium sulfide catalyst. (a) the pH change vs. time with the adding of ammonia water (b) cyclic voltammgrams of rhodium sulfide catalysts with and without the neutralization in the synthesis

3.3.2 Particle Size and Crystal Structure

TEM was applied to validate the decrease in particle size by the usage of a functionalized carbon substrate. Figure 3.21 shows the particle sizes of various catalysts. By using functionalized carbon, the diameter of rhodium sulfide catalysts decreases from around 13.2 nm to around 7.2 nm. This finding correlates well with the increase in the mass-specific surface area shown in the CV of Figure 3.19.

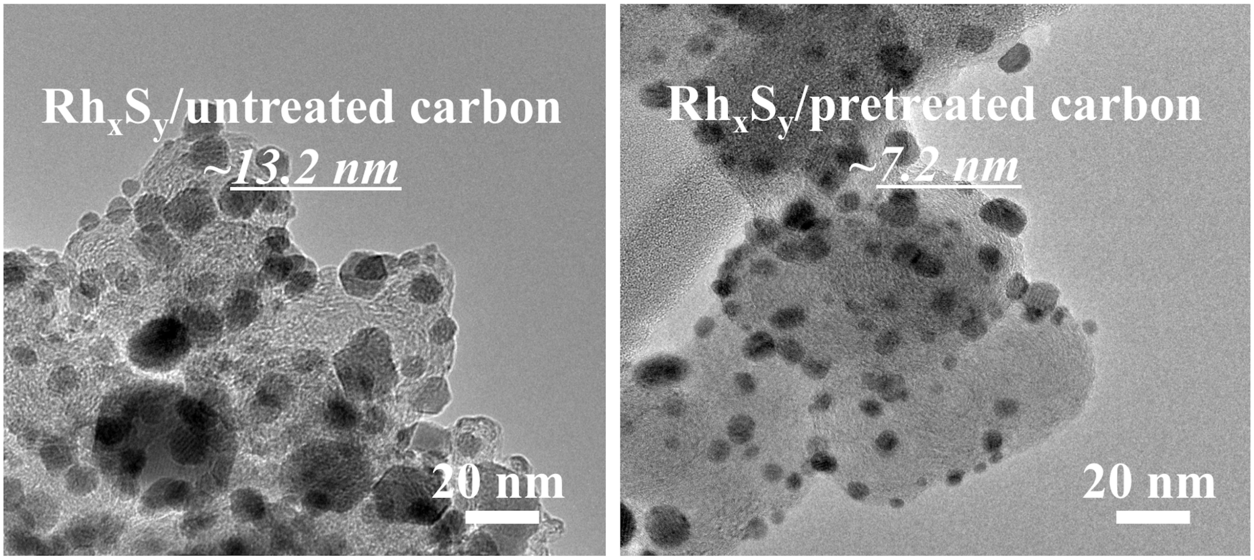

Figure 3.21. TEM pictures of different rhodium sulfide catalysts

The XRD results of the synthesized catalyst on different substrates shown in Figure 3.22 confirmed the main crystal phase of the rhodium sulfide catalyst on the untreated or pretreated carbon is $Rh_{17}S_{15}$. It is noted that the diffraction spectra between 31° to 42° clearly marks the fingerprint region of the $Rh_{17}S_{15}$ phase. The atomic ratio of Rh to S for the two types of catalysts measured by XPS is 1.10, the same as the Rh to S atomic ratio of $Rh_{17}S_{15}$. Thus, the XPS results further confirm the main crystal phase in these synthesized catalysts to be $Rh_{17}S_{15}$.

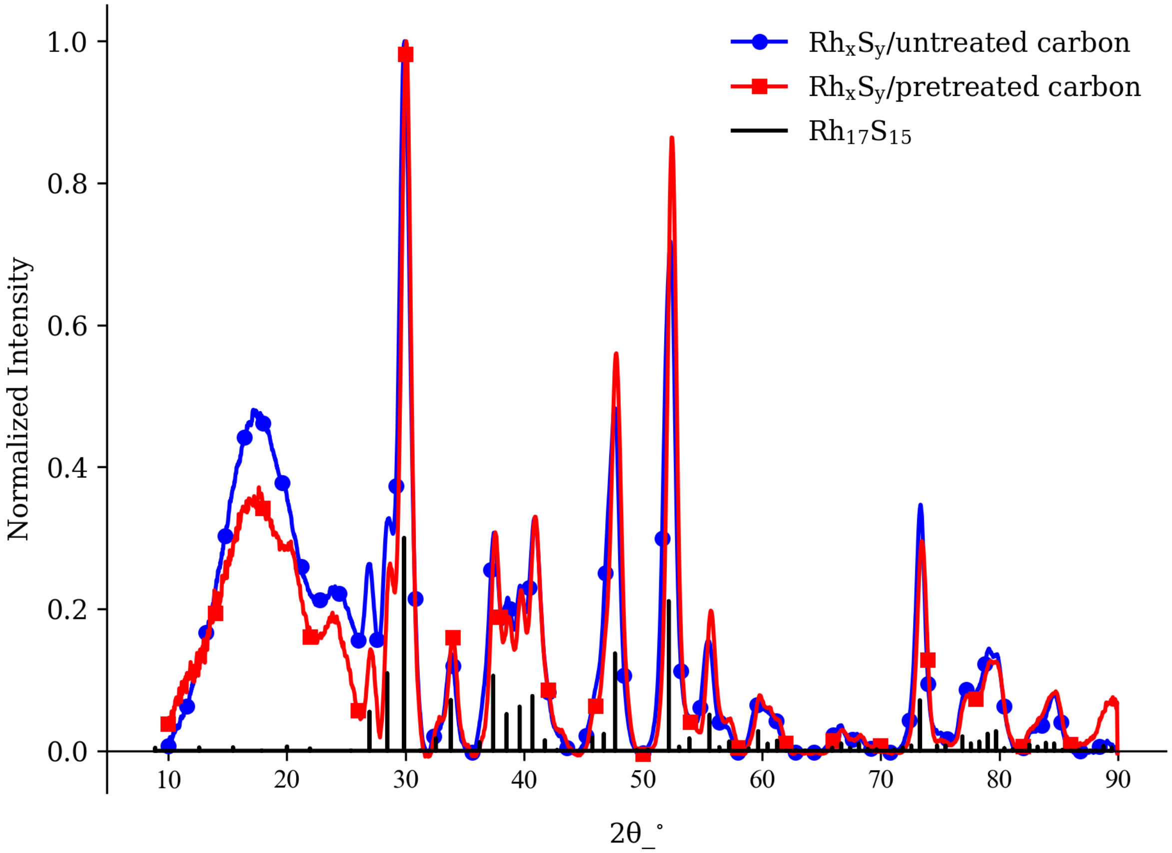

Figure 3.22. XRD for rhodium sulfide catalysts (JCPDS $Rh_{17}S_{15}$ pattern: 073-1443)

3.3.3 Electrochemical Characterizations of Catalyst

Figure 3.23 shows the catalytic activity of the synthesized rhodium sulfide catalysts. The catalysts synthesized on the untreated or pretreated carbon show similar active-area-specific activity further demonstrating that the functionalized support material does not affect the exchange current density of the catalyst. It also proves that the rhodium sulfide catalysts synthesized on different carbon support materials have similar facets and crystal structures. Note that the slope of HOR measured is larger than that of HER for similar catalysts observed in previous studies. This is attributed to the bi-functional catalytic property of rhodium sulfide in the HOR/HER. For the HOR, only the rhodium sites on the surface of the catalyst can catalyze the dissociation of a H_2 molecule and oxidation of H to H^+. For HER, however, both of the sulfur and rhodium sites on the catalyst surface can facilitate the reduction of a hydronium ion to hydrogen.[67] Since the combined number of active sites of Rh and S (i.e. the area "a" parameter in Equation 2.2) is greater than that of active Rh sites alone, the same overpotential (η) value results in a larger measured current density (i) or small η vs. i slope.

Figure 3.24 shows the charge and discharge polarization curves of a H_2-Br_2 fuel cell with rhodium sulfide catalysts synthesized with treated and untreated carbon substrates used in the negative hydrogen electrode. These polarization curves have been corrected for IR losses. A fuel cell polarization curve can be divided into three regions: activation loss region (low current density), ohmic loss region (medium current density), and mass transfer loss region (high current density). The polarization curves were fully IR corrected to remove the effect of all ohmic resistances in the fuel cell, including the resistance from the membrane, which allowed us to study the kinetics and mass transfer effects. Activation polarization is the overpotential required to overcome the activation energy of the electrochemical reaction on the catalytic surface. In this region, a lower overpotential at the same current density indicates that more active sites participated in the reaction. More catalytic sites are active when more catalyst sites have access to the Nafion polymer electrolyte. Catalytic sites that are not in contact with the Nafion polymer electrolyte are not utilized. The mass transfer loss region reveals the effect of mass transport on the voltage loss in the cell, in this case

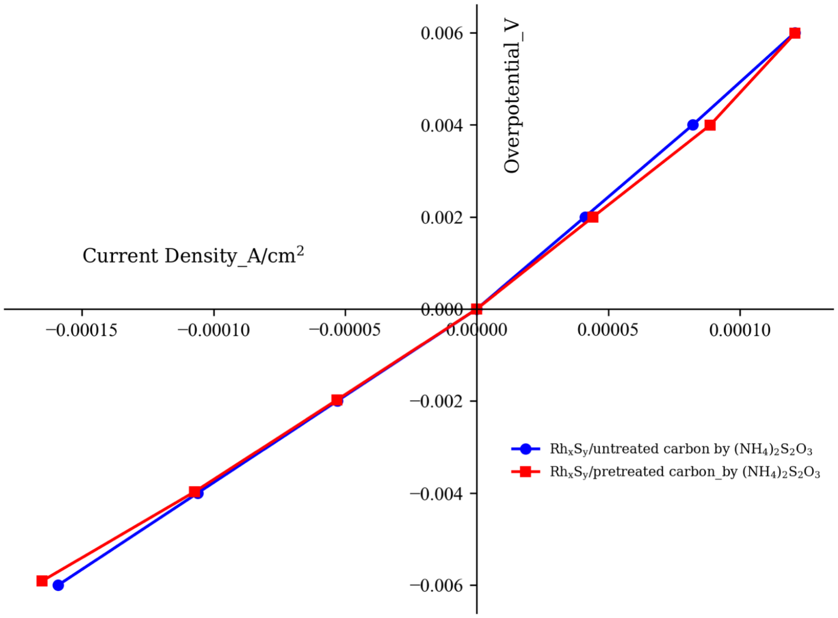

Catalyst	i_o (HOR) _A/cm^2	i_o (HER) _A/cm^2	i_o^*(HOR) _A/cm^2	i_o^*(HER) _A/cm^2
Rh_xS_y/untreated carbon by $(NH_4)_2S_2O_3$	0.47	0.62	0.43	0.56
Rh_xS_y/pretreated carbon by $(NH_4)_2S_2O_3$	0.46	0.64	1.68	2.32

Figure 3.23. Linear polarization curves of rhodium sulfide catalysts (electrolyte: 1M hydrogen-saturated H_2SO_4 solution, rotation speed: 2400rpm, working electrode: RDE, counter electrode: Pt foil, reference electrode: SCE)

due to the voltage loss in the hydrogen electrode. A fuel cell must be continuously supplied with fuel and oxidants to produce electricity. Products must also be continuously removed to achieve maximum fuel cell efficiency. If the fuel cell has a higher resistance of mass transport to/from the electrode surface, the overpotential (voltage loss) in the mass-transfer-controlled region at the same current density will be larger.

Figure 3.24 compares the performance of the fuel cells with the catalysts synthesized on untreated and pretreated carbon at different Nafion ionomer ratios. The bromine electrodes in these fuel cells were identical. The discharge curves of the fuel cell with catalyst on untreated carbon (blue curves with circle and star symbols) displayed similar kinetics performances in the activation polarization region for both higher and lower Nafion to catalyst ratio cases. This indicates that the catalyst area in contact the Nafion polymer electrolyte has reached the maximum value even with

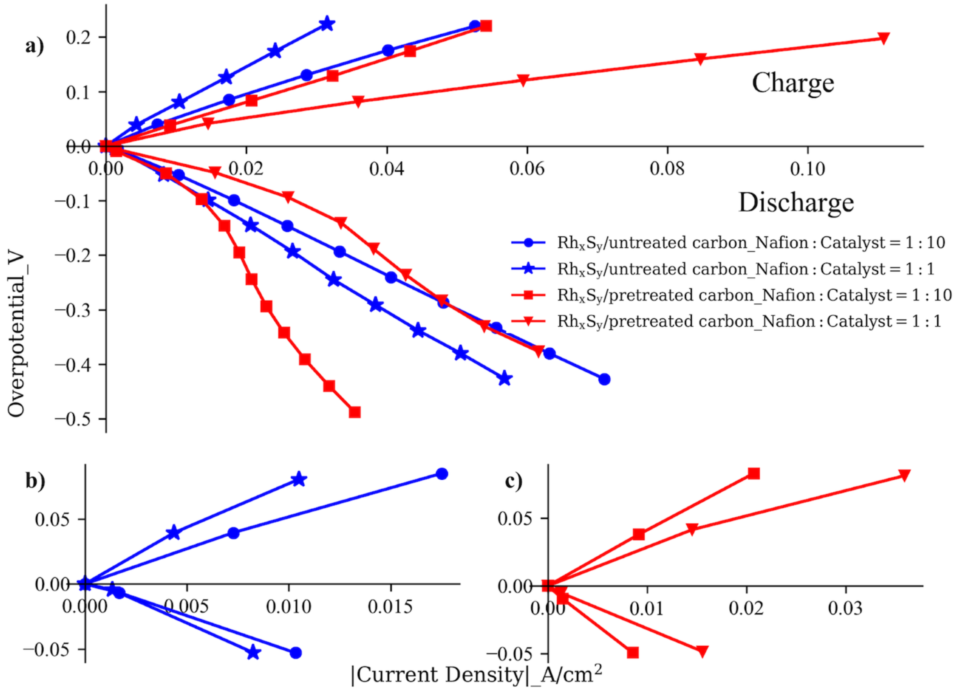

Figure 3.24. H_2-Br_2 fuel cell discharge and charge polarization curves with untreated and treated rhodium sulfide catalysts with different catalyst to Nafion ratios after full IR correction (a) whole polarization curves (b) kinetics-controlled polarization curves of Rh_xS_y/untreated carbon (c) kinetics-controlled polarization curves of Rh_xS_y/pretreated carbon.

the lower Nafion to catalyst ratio. Increasing the Nafion content does not increase the coverage on the catalyst surface, but it instead increases the thickness of the Nafion layer and mass transport resistance in the cell. Consequently, the fuel cell made with the catalyst on untreated carbon with a lower Nafion to catalyst ratio (blue curve with circle marker) produces better charge/discharge performance in the mass transfer loss region due to the reduced mass transfer resistance with thinner Nafion layer. The discharge curves of the fuel cell with the catalyst with pretreated carbon (red curve with triangle and square symbols) that has a higher mass-specific active area, however, show the opposite behavior. Note that the amount of rhodium sulfide catalyst loading in all these fuel cells was the same. The fuel cell with the catalyst on pretreated carbon has obviously better performance in the kinetics-controlled region at higher Nafion ratio which indicates that the higher Nafion content in the catalyst ink increases the Nafion-covered catalyst area. This makes sense since more active sites would require more Nafion content to ensure that all sites have access to the polymer electrolyte. Among all the discharge curves, the catalyst with pretreated carbon (red curve with triangle symbol) shows the best kinetics performance. This can be attributed to the combined effect of more active and accessible catalytic sites in the hydrogen electrode.

While the fuel cells with rhodium sulfide catalyst with pretreated carbon have the best performance in the kinetic region and their performance follows the expectation, the poor performance of these fuel cells in the mass transport dominant region was unexpected since it contradicted the catalyst performance when tested in a liquid electrolyte. Further investigation revealed the cause for this unexpected performance as follows. Since the ketone group on the carbon surface was found to have weak affinity for Nafion ionomer, the carbon substrate with ketone as the surface functional group led to a non-uniform distribution of Nafion on the pretreated carbon surface. Furthermore, it results in an excessively thick Nafion polymer layer in regions where coverage exists. Note that Nafion ionomer thickness in these coverage regions was equal to the volume of Nafion divided by the Nafion-friendly area on the carbon surface. So, for the same amount of Nafion used in the catalyst ink, a thicker Nafion layer can be expected when the Nafion-friendly area on the carbon surface is smaller. In Figure 3.24, mass transfer limitation effects can be observed in the discharge curves of the fuel cells with the catalysts with pretreated carbon and can be attributed to the higher mass transfer resistance of hydrogen to the catalyst surface created by the thicker Nafion layer on the catalyst active surface.

This unexpected mass transport phenomenon was not observed in the charge curves of the fuel cell with the high-surface-area catalyst because HER is not mass transport limited by the transport of hydrogen molecules (see Figure 3.24). The hydrogen evolution reaction rate depends on the concentration of the hydronium ions which are abundant in the hydrogen electrode from the Nafion polymer electrolyte and crossover hydrobromic acid ions. Consequently, fuel cells with a higher active surface area delivered higher charge performance.

Figure 3.24 also shows that the expected performance improvement of the mass-specific surface area and activity of the catalyst was not fully demonstrated in the H_2-Br_2 fuel cell due to the affinity issue between the ketone surface group and Nafion ionomer layer in the hydrogen electrode catalyst layer. An attempt to resolve this issue is underway.

3.3.4 Theoretical Calculation

It is hypothesized that the carbon with the carboxylic group can facilitate the Nafion distribution on the carbon surface, which will increase the area of Nafion-covered catalyst in the CL and then the fuel cell performance. The affinity of carboxylic group with Nafion has been proved by the adsorption test in Figure 3.14. A theoretical calculation with density functional theory (DFT) about the electrostatic potential (ESP) on the Nafion ionomer and carbon clusters with different chemical groups is shown in Figure 3.25. The fullerene-related structure was chosen for the theoretical model of activated carbon. The model is a $C_{45}H_{15}$ cluster containing one pentagonal and fifteen hexagonal rings.[94,95] The structures of Nafion ionomer and carbon clusters were firstly optimized by semi-empirical method PM6 and then calculated for the single point energy by B3LYP/6-31g of DFT. Figure 3.25 shows that the backbone region (PTFE) has almost zero or slightly positive ESP which will not show a strong interaction with the carbon surface. The sulfonate group region is dominated by the negative ESP (blue color) which will be anchored to the functional group with strong positive ESP (red color). The DFT results show that the carbon with ketone has strong negative ESP on the ketone group and the carbon surface due to the increase of basicity, while the carbon with the carboxylic group is dominated by the positive ESP. Moreover, the strong positive ESP also impairs the basicity of the nearby carbon surface which is shown as light red color. When the catalyst layer was hot pressed, the PTFE backbone will fall to the carbon surface due to the vaporization of the solvent in the catalyst ink. Since there is no anchoring point can be located on the carbon surface with the ketone, Nafion will tend to agglomerate together due to the interactions among its own regions with negative and positive ESP. It results in a thick and inhomogeneous distribution of Nafion layer on the Nafion-covered catalyst surface. When the anchoring points can be provided in the carbon with the carboxylic group, a higher Nafion-covered region area can be expected. The initial DFT calculations correspond to the experimental data in Figure 3.14, though the current method of theoretical calculation is not highly accurate.

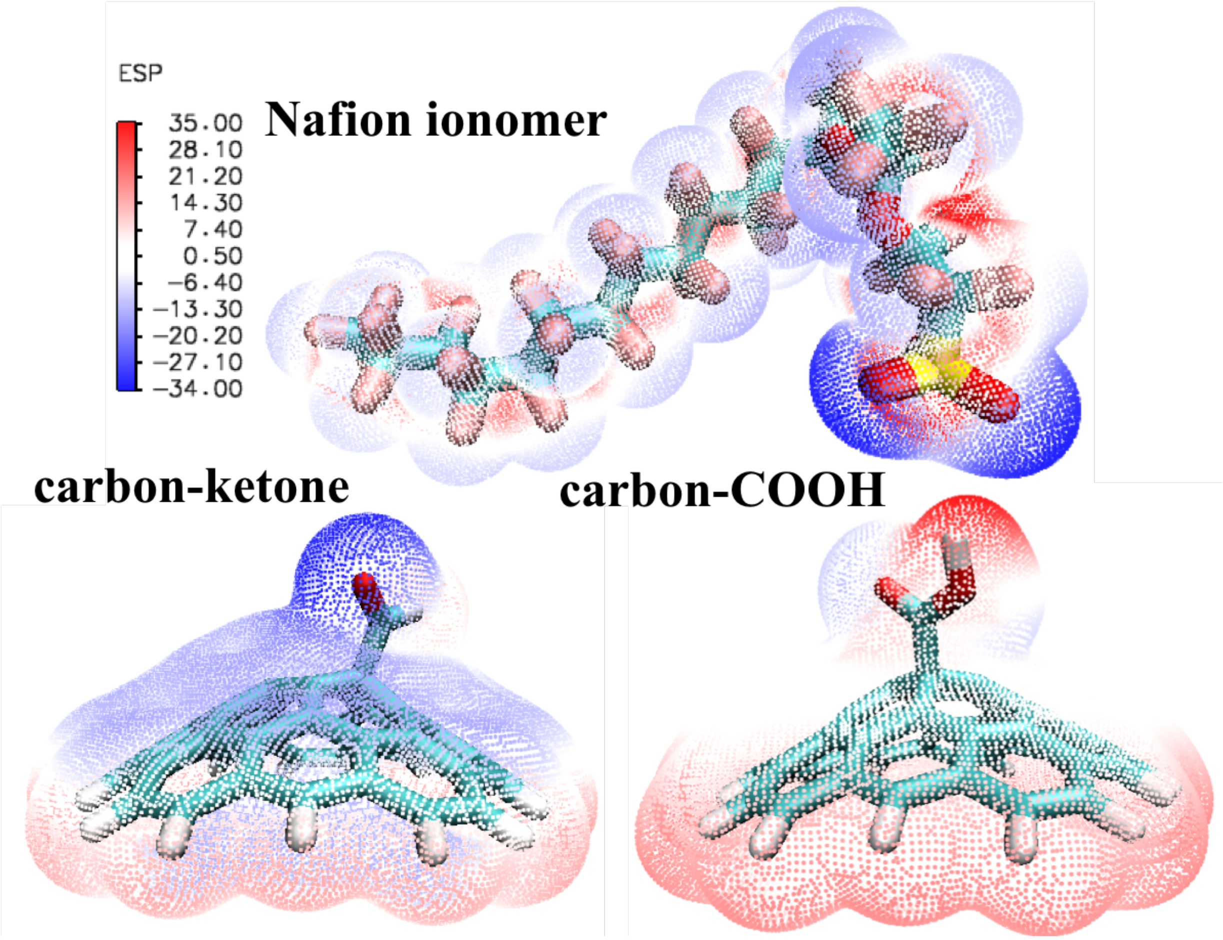

Figure 3.25. Electrostatic potential of Nafion and carbon with ketone/carboxylic group

3.3.5 Summary

A rhodium sulfide catalyst with a high mass-specific surface area was synthesized by functionalizing the carbon support material in this section. High active areas were validated by TEM, and high ECSA/mass was confirmed by cyclic voltammetry. This study proves that carbon with ketone surface groups is preferable for the adsorption of Rh cation when the PZC of the adsorbent is lower than the pH of the synthesis solution, and carboxylic surface groups impair the adsorption of Rh cation in this case. The ketone group on the modified catalyst, however, can influence the performance of this in a H_2-Br_2 fuel cell by changing the affinity between the catalyst and the Nafion ionomer. Consequently, due to the affinity issue between the ketone surface group and Nafion, improvements to the mass-specific surface area and the productivity of the catalyst were not fully demonstrated in the H_2-Br_2 fuel cell. The poor mass transport performance shown in the fuel cell test can be resolved by the conversion from the current ketone group to the Nafion-friendly carboxylic group, which will be discussed in Section 3.5.

3.4 New Process to Synthesize Highly Active and Dispersed Rhodium Sulfide Catalyst from Na_2S with Functionalized Carbon and Diffusion-Controlled Nanoparticle Growth Model for HOR/HER in Corrosive Environment

Transition metal chalcogenides like Rh_xS_y have broad applications as the catalyst in the H_2-Br_2 fuel cell, photochemical decomposition of aqueous sulfide, and electrolysis of HCl/HBr.[66,96,97] In those cases, the commonly used metallic catalyst, Pt, has been shown to be poorly stable in the highly corrosive solutions like hydrochloride and bromine. The performance of Pt catalyst is deteriorated by the corrosion and poisoning of Cl^-, Br^- and Br_2.[98] In contrast, the rhodium sulfide is stable in the corrosive solution and can provide acceptable catalysis performance for HOR, HER, and ORR, which makes rhodium chalcogenides as a promising alternative of the Pt catalyst in the application for the corrosive environment. The application of Rh_xS_y/C as the HOR/HER catalyst in the H_2-Br_2 fuel cell is the primary focus of our group, since it is believed that hydrogen-bromine fuel cell is a promising solution for the highly efficient and cost-effective energy storage method for the intermittent energies like wind and solar power. The activity of Rh_xS_y in the HBr solution was also reported in this section.

As mentioned in the previous sections, the rhodium sulfide catalyst suffers from two main drawbacks, low mass-specific surface area, and low catalysis activity. The low mass-specific surface area coming from the large and broad distribution of nanoparticle size can be solved by the functionalization of the supporting material and diffusion-controlled model of nanoparticle growth. Functionalization of supporting carbon can provide more active sites for the adsorption and dispersion of rhodium ions to control the particle size, which has been reported and discussed in Section 3.3. The relationship between the functional groups on the carbon surface like the basic/acidic group and adsorbed ion was also discussed in the previous section. Besides the functionalization of supporting material, the particle growth model can affect the particle size and distribution as well. The nanoparticles (NPs) growth process can be divided into two steps, 1) the transportation of monomer (the building material of NPs) to the seed surface and 2) the adsorption of monomer to grow the NPs. The diffusion-controlled and adsorption-controlled model of NPs growth can be distinguished based on the velocity of the two steps. The diffusion-controlled model is limited by the first step which synthesize the monodisperse and relatively small NPs, while the adsorption/kinetics-controlled model is limited by the second one which may generate the polydisperse and relatively large NPs.[99, 100, 101] The reasons for the difference in these two mechanisms will be explained later.

The second drawback of the current catalyst is from the low activity crystal phase of rhodium sulfide catalyst. There are three types of rhodium sulfide crystal phases, Rh_2S_3, Rh_3S_4 and $Rh_{17}S_{15}$. Among those crystal structures, Rh_2S_3 is not active while Rh_3S_4 and $Rh_{17}S_{15}$ are active phases for catalysis of HOR/HER. The mixed active phases are called Rh_xS_y in this dissertation. The conversion from Rh_2S_3 to Rh_3S_4 and $Rh_{17}S_{15}$ is by the thermal treatment to release extra sulfur atoms from Rh_2S_3. Based on the density functional theory (DFT) calculation, the highest activity for the catalysis of HOR/HER is achieved by Rh_3S_4. There are two possible methods to adjust the composition of crystal phases of rhodium sulfide, adjusting the temperature of thermal treatment and introducing different types of sulfur sources. The energy window among these three rhodium sulfide crystal phases is relatively small.[102] At lower or higher temperatures of the thermal treatment, one ends up with either Rh_2S_3 or Rh respectively, which are inactive for HOR/HER or corrodible in the corrosive environment. In the meanwhile, different sulfur sources may result in different metal sulfide monomers and final composition.[103] The products of nickel sulfide from sodium thiosulfate and C_2H_5NS under the same synthesis conditions are Ni_3S_4 and NiS respectively. To my best knowledge, this is the first work to modify the crystal phases of rhodium sulfide by different sulfur sources.

3.4.1 Attempt to Improve on the Current Patent of Rhodium Sulfide Synthesis

The synthesis method used in the core-shell rhodium sulfide (Section 3.1) and rhodium sulfide with functionalized carbon (Section 3.3) is based on the patent of De Nora which is a global electrochemistry company, where the source of rhodium is $RhCl_3$ solution and the sulfur is provided by the dissociation of $(NH_4)_2S_2O_3$. The initial purpose to synthesize the rhodium sulfide catalyst by Na_2S was to avoid the intellectual property of De Nora. In the initial try, the rhodium sulfide was synthesized by following the patent of De Nora but only replacing $(NH_4)_2S_2O_3$ with Na_2S. The catalyst supporting material was the untreated XC72R. The thermal treatment temperature and ramp were same with those of the catalyst with $(NH_4)_2S_2O_3$ as sulfur source. The cyclic voltammetry test of the newly synthesized catalyst (purple curve with downward triangle) in Figure 3.26 revealed an interesting fact that it is more active than that synthesized with $(NH_4)_2S_2O_3$. It can be seen that Rh_xS_y/untreated carbon synthesized by Na_2S has more negative potential for HOR compared to that of Rh_xS_y/untreated carbon with $(NH_4)_2S_2O_3$ (blue curve with circle symbols). The negative shift in the potential of the HOR peak indicates that the Rh_xS_y from Na_2S has a smaller overpotential for the HOR. The initial try shows that the usage of Na_2S is not only an approach to avoid the current patent of De Nora in Rh_xS_y synthesis, but also a 'magical' way to increase the activity of rhodium sulfide catalyst.

To explore the natures of the 'magical' improvement of activity of catalysis, sulfide compounds with different cations and anions, K^+, Na^+, S^{2-} and ${S_2O_3}^{2-}$ were used to synthesize rhodium sulfide. By using different cations in the sulfide compounds, the effect of cations to the rhodium sulfide can be excluded or confirmed. When the Na^+ of Na_2S (purple curve with downward triangle symbols) was replaced by K^+ of K_2S (red curve with square symbols), the size and location of HOR peaks of these two catalysts do not change. A similar phenomenon can be observed with the catalysts synthesized by $(NH_4)_2S_2O_3$ (blue curve with circle symbols) and $Na_2S_2O_3$ (green curve with upward triangle symbols), of which HOR peaks are more positive compared to those peaks of rhodium sulfide from Na_2S and K_2S. These two groups indicate that the change of cation does not affect the catalysis performance. It is the anion of sulfide compound that increases the activity of rhodium sulfide catalyst in HOR/HER. Moreover, it shows that the sulfide anions result in the more active catalyst while the thiosulfate anions lead to the less active catalysis performance regardless of the types of cations in the sulfide compounds. The reason for the modification for the rhodium sulfide catalyst from S^{2-} anion will be discussed later.

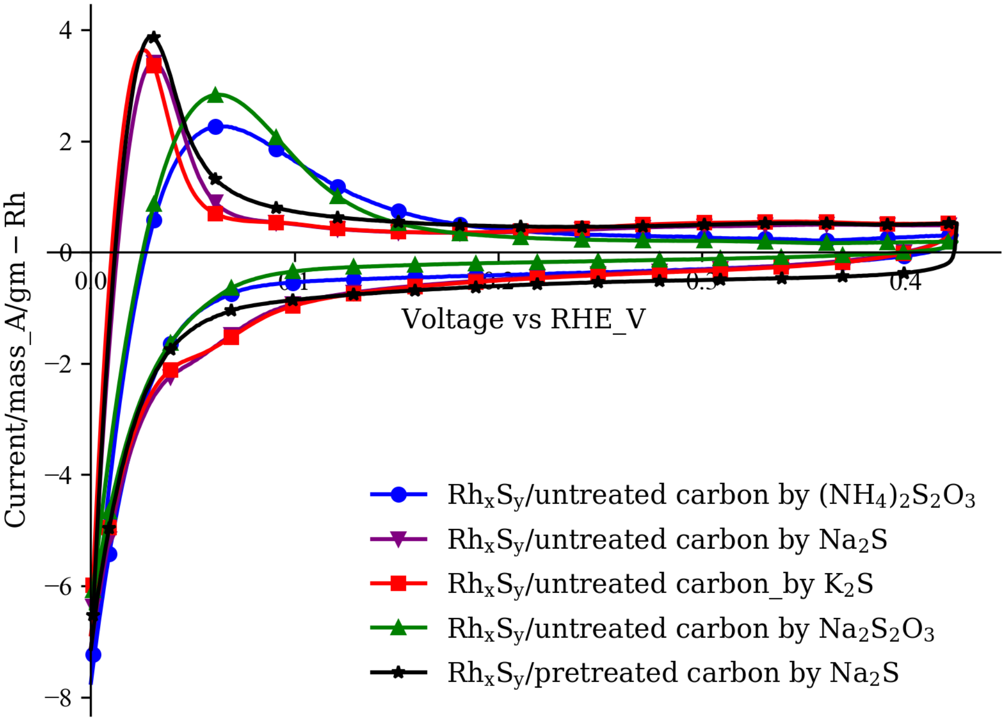

Figure 3.26. Cyclic voltammograms of rhodium sulfide synthesized by the sulfide compounds with different cations and anions (electrolyte: 1M N_2-saturated H_2SO_4 solution, working electrode: catalyst-coated GDE, counter electrode: Pt foil, reference electrode: SCE, scan rate: 10mV/s)

After the improvement of catalysis activity of rhodium sulfide has been attributed to the sulfide anion, the approach of functionalizing the supporting material to increase the mass-specific surface area in the previous section was applied to the rhodium sulfide synthesized by Na_2S. The CV of rhodium sulfide catalyst on pretreated carbon synthesized by Na_2S is shown as the black curve with star symbols in Figure 3.26. It is evident that functionalization of supporting material does not increase the ECSA/mass of catalyst as what it does for Rh_xS_y from $(NH_4)_2S_2O_3$. The nanoparticle growth mechanism discussed in Section 3.4.2 explores the reason of unchanged mass specific surface area with functionalization of carbon material.

3.4.2 Nanoparticle Growth Mechanism

The pH of the solution of $RhCl_3$ at this synthesis is 1.2, which results in a negatively charged oxygen functional sites on the carbon surface. It has been discussed in Section 3.3 that functionalized carbon material with ketone group is preferable for the adsorption of rhodium cation when the carbon surface is negatively charged. The mass-specific electrochemical surface area (ECSA/mass of Rh) of Rh_xS_y was improved from 9.1 $m^2/gm-Rh$ of catalyst on the untreated carbon to 21.8 $m^2/gm-Rh$ of catalyst on the functionalized carbon, while the average particle size was decreased from 13.2 nm to 7.2 nm. In this section, the nanoparticle growth mechanism is discussed, which can facilitate the nanoparticle size control and help to understand the unchanged mass-specific surface area of rhodium sulfide/pretreated carbon synthesized by Na_2S.

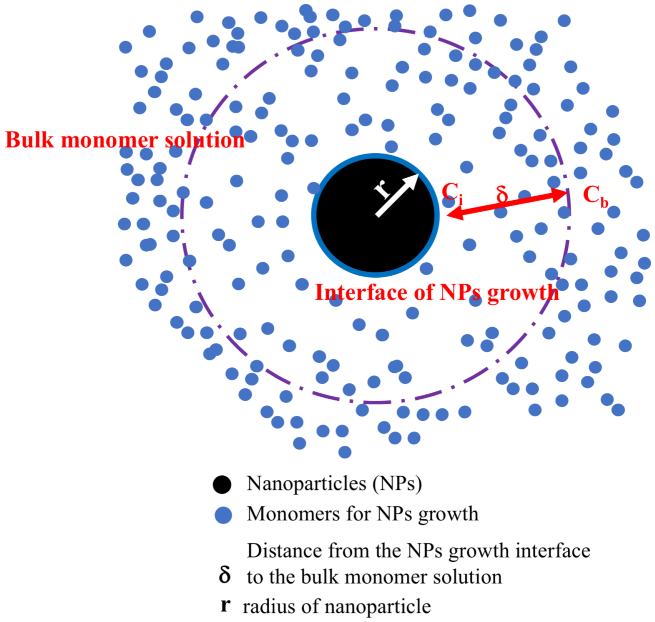

Figure 3.27. Schematic of nanoparticle growth

A schematic of the formation of NPs is shown in Figure 3.27. The monomers, Rh_2S_3 in this case, move to the nucleation center of NP and form the nanoparticle. δ is the distance from the solid interface of NP growth to the bulk monomer solution, and r is the radius of nanoparticle. The C_i is the concentration of monomers on the surface of the nanoparticle (nucleation center), while C_b is the concentration of monomers in the bulk solution. By the Fick's first law, the molar rate of monomer (mol/s) between the bulk monomer solution ($r+\delta$) and the interface of NPs growth (r) in the diffusion-controlled model is,

$$\dot{N} = 4\pi x^2 D\frac{dC}{dx}, \quad r \leqslant x \leqslant r+\delta \tag{3.1}$$

The molar rate of monomer is a constant at the steady state, then integrate equation 3.1 between $r \leqslant x \leqslant r+\delta$ one can get,

$$\int_r^{r+\delta} \frac{\dot{N}}{x^2}dx = \int_{C_i}^{C_b} 4\pi D dC \tag{3.2}$$

$$\dot{N}(\frac{1}{r} - \frac{1}{r+\delta}) = 4\pi D(C_b - C_i) \tag{3.3}$$

$$\dot{N} = 4\pi r(r+\delta)D\frac{C_b - C_i}{\delta}, \quad r \leqslant x \leqslant r+\delta \tag{3.4}$$

where the D is diffusivity of the monomer in the solution. The diffusion can be controlled and limited by either reducing the diffusivity (D) or reducing the driving force of diffusion ($C_b - C_i$). The diffusivity can be reduced by a complexing agent for the monomer or a solution that has a high viscosity. In the case chosen for this study, the C_b of Rh_2S_3 monomer was kept low by slowing addition rate of the sulfur source to control the sulfidation reaction between S^{2-} and Rh^{3+}.

At steady state, the nanoparticle growth rate (left side of equation 3.5) should be the same with the molar flow rate of the monomer to the nucleation center surface (equation 3.4 and the right side of equation 3.5),

$$R_{growth} = \frac{4\pi r^2}{V_m}\frac{dr}{dt} \tag{3.5}$$

where V_m is molar volume of nanoparticle (m^3/mol). In the diffusion-controlled model, all the Rh_2S_3 monomer on the nucleation surface should be consumed immediately after they are transferred to the surface since the kinetics of NPs growth is much faster than the diffusion rate, which means $C_i = 0$. From equations 3.4 and 3.5, one gets

$$\frac{dr}{dt} = (\frac{1}{r} + \frac{1}{\delta})V_m C_b D \tag{3.6}$$

As shown in equation 3.3, it can infer that the particle growth rate decreases in the diffusion-controlled model with the increase of r, which means that the particle size is small and the size distribution is monodisperse if the total reaction time is controlled appropriately. With infinite reaction time, the Ostwald ripening that dissolves the small NPs for the agglomeration into the large NPs becomes uncontrolled which finally results in the super large NPs.[104, 105]

In the adsorption-controlled model, the limiting factor becomes the surface reaction for the monomer adsorption and NPs growth, which indicates that the C_i equals to C_b. Then the molar rate of monomer transfer is determined by the consumption rate of the monomer on the particle surface in the steady state,

$$\dot{N} = 4\pi r^2 k_p C_b \tag{3.7}$$

where the k_p is the rate of surface monomer adsorption and particle growth in m/s.

From the equation 3.5 and 3.7, the radius of NPs growth rate can be written as,

$$\frac{dr}{dt} = V_m C_b k_p \tag{3.8}$$

In the adsorption-controlled model, the particle growth rate,dr/dt, is independent of D, δ, and r which means that the particle size keeps increasing at a constant rate. The higher bulk concentration is, the faster speed of particle growth will be.

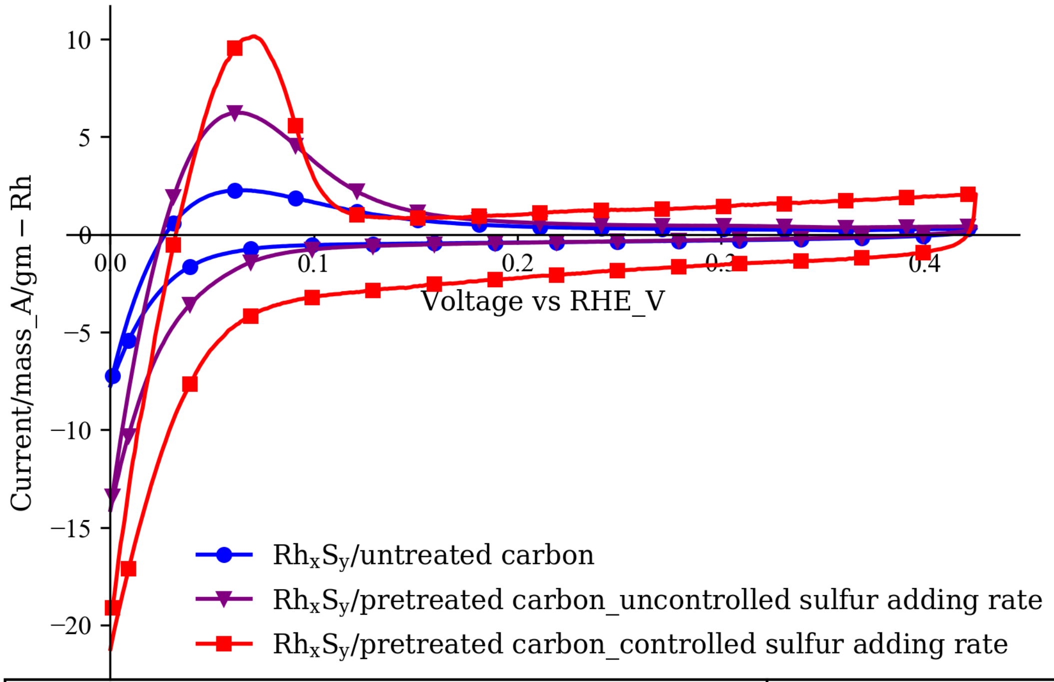

Catalyst	ECSA/mass_m^2/gm − Rh
Rh_xS_y/untreated carbon	9.1
Rh_xS_y/pretreated carbon_uncontrolled sulfur adding rate	21.8
Rh_xS_y/pretreated carbon_controlled sulfur adding rate	36.5

Figure 3.28. Cyclic voltammogram of Rh_xS_y synthesized by different carbon substrates and speed of adding sulfur rate* (electrolyte: 1M N_2-saturated H_2SO_4 solution, working electrode: catalyst-coated GDE, counter electrode: Pt foil, reference electrode: SCE, scan rate: 10mV/s)
* The sulfur source here is $(NH_4)_2S_2O_3$

A series of rhodium sulfide catalysts were synthesized by controlling the rate of adding the sulfur source to prove the numerical model about the particle growth. Here, the conventional sulfur source, $(NH_4)_2S_2O_3$ was used to explore the effect of the adding rate of the sulfur source. In Figure 3.28, the ECSA/mass of Rh_xS_y on the untreated carbon is improved from 9.1 to 21.8 $m^2/gm-Rh$ by using functionalized carbon material. In these two syntheses, the $(NH_4)_2S_2O_3$ solution was added by three equivalent aliquots with 2 min interval. In the third case, the rate of adding sulfur source, $(NH_4)_2S_2O_3$, was controlled at a lower level to create the diffusion-controlled model. The total volume of thiosulfate solution was unchanged, but it was added by fifteen aliquots with 2 min interval. The ECSA of rhodium sulfide catalyst on the pretreated carbon with the controlled sulfur source adding rate is further improved to 36.5 $m^2/gm-Rh$, which proves that the effectiveness of the diffusion-controlled model in controlling the particle size and distribution.

3.4.3 Difference between $S_2O_3{}^{2-}$ and S^{2-}

The numerical modeling and experimental results shown in section 3.4.2 confirmed that the diffusion-controlled model contributes to the small particle size and uniform size distribution, while the adsorption/kinetics-controlled model may result in the large particle size and wide distribution of NPs size. Based on these results, the unimproved mass-specific surface area of the Rh_xS_y/pretreated carbon synthesized by Na_2S may be explained by the NPs growth mechanism. Since the solvent and monomer are same for the rhodium sulfide synthesis from sulfide and thiosulfate compounds, the diffusivity (D) and the rate of surface monomer adsorption and particle growth (k_p) are identical for both cases. The most possible reason resulting in the two different particle growth models for the two sulfur sources may be the concentration of Rh_2S_3 monomer in the bulk solution (C_b).

Starting from this hypothesis, the mechanisms to release sulfide anion from $S_2O_3{}^{2-}$ and S^{2-} were investigated. Na_2S is a strong electrolyte which dissociates into sodium cation and sulfide anion completely and immediately. On the other hand, $(NH_4)_2S_2O_3$ releases the sulfide anion via a two-step dissociation as shown below,

$$(NH_4)_2S_2O_3 \rightarrow 2NH_4{}^{+} + S_2O_3{}^{2-} \tag{3.9}$$

$$S_2O_3{}^{2-} + H_2O \rightarrow SO_4{}^{2-} + S^{2-} + 2H^{+} \tag{3.10}$$

The fact that Na_2S is a strong electrolyte and dissociates quickly and completely decides that the concentration of sulfide anion reaches the maximum value immediately after it is added to the $RhCl_3$ solution. Consequently, the rhodium cations react quickly with sulfur anions to form a high concentration of Rh_2S_3 monomer in the solution. Based on the discussion of NPs growth mechanism, the high monomer concentration, which greatly increase the transport rate of the monomer to the NPs surface, causes the growth of the Rh_2S_3 to be kinetics-controlled, which leads to the larger particle size. Compared to the complete dissociation of Na_2S, the two-step dissociation of $(NH_4)_2S_2O_3$ release sulfide anion slowly as shown in Figure 3.29.

Since the dissociation of $S_2O_3{}^{2-}$ creates H^{+}, the dissociation degree can be measured as the pH of the solution. Two H^{+} cations are created per dissociated $S_2O_3{}^{2-}$ in equation 3.10. Figure 3.29 shows the dissociation level of ammonia thiosulfate versus the temperature. From room temperature to 100°C, which is the reaction temperature for the synthesis of Rh_2S_3, only 0.0025% $S_2O_3{}^{2-}$ is dissociated. Then it can be inferred that the dissociation of thiosulfate in the synthesis of Rh_2S_3 is driven by the precipitation of Rh^{3+}. The equilibrium of reaction 3.10 is continuously driven forward by the Rh^{3+} sulfidation reaction. The incomplete dissociation of $S_2O_3{}^{2-}$ anions determines the low Rh_2S_3 monomer concentration in the solution which causes the NPs growth process to be diffusion-controlled.

For the untreated supporting carbon, the total amount of active sites for the precipitation of NPs is limited. Even the kinetics-controlled NPs growth can still achieve a similar mass specific surface area due to the limitation of total precipitation sites. When the functionalization increases the total amount of precipitation-active sites, a sulfide compound that can release S^{2-} slowly results in NPs

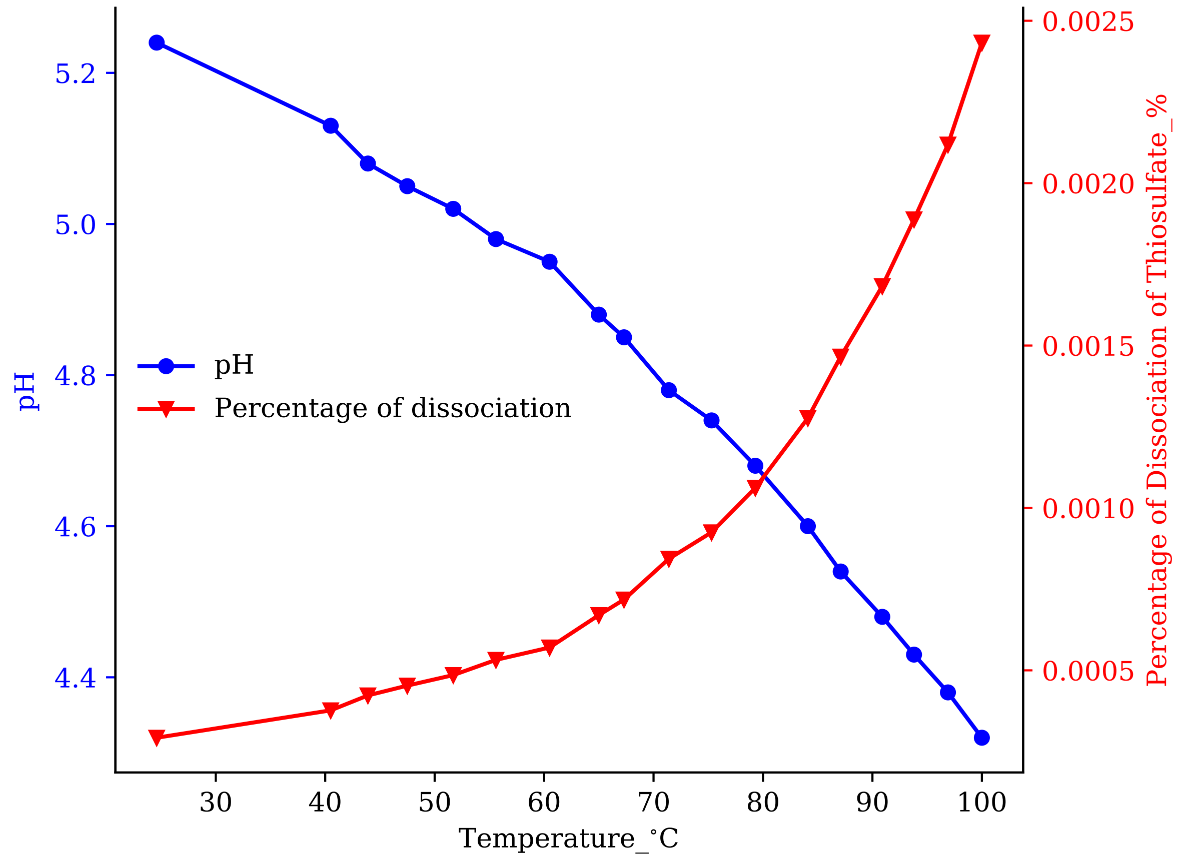

Figure 3.29. Dissociation of thiosulfate versus the temperature

with smaller particle size, as shown in Figure 3.28.

3.4.4 NPs Size Control of Rh_xS_y Synthesized by Na_2S

The investigation of the difference between $S_2O_3{}^{2-}$ and S^{2-} reveals the reason for the unchanged mass specific surface area of Rh_xS_y/pretreated carbon synthesized by the normal Na_2S addition process, which can be modified by slowing the adding rate of Na_2S. In this study, the adding rate of sulfur source was further optimized by using a peristaltic pump that can deliver a slower and continuous addition rate. The Na_2S solution was added within 2 h by the peristaltic pump (3 mL/h). The TEM pictures in Figure 3.30 confirm the decrease of the NPs size by the diffusion-controlled model of NPs growth using this new sulfur source addition approach. With the slow addition rate of sulfur source, the average particle size of Rh_xS_y/pretreated carbon synthesized by $((NH_4)_2S_2O_3$ decreases to 5.2 nm, while the average particle size of Rh_xS_y/pretreated carbon synthesized by Na_2S decreases further to a lower value of 3.2 nm, with the optimized adding rate of sulfur source. Without the diffusion-controlled model, the diameter of Rh_xS_y/pretreated carbon with $((NH_4)_2S_2O_3$ was reported as 7.2 nm in Figure 3.21. Besides the decreased particle size, the narrow size distribution of NPs in the TEM picture of Rh_xS_y/pretreated carbon by Na_2S confirms that the particle growth rate decreases with the increase in radius of NPs (equation 3.6) in the diffusion-controlled model.

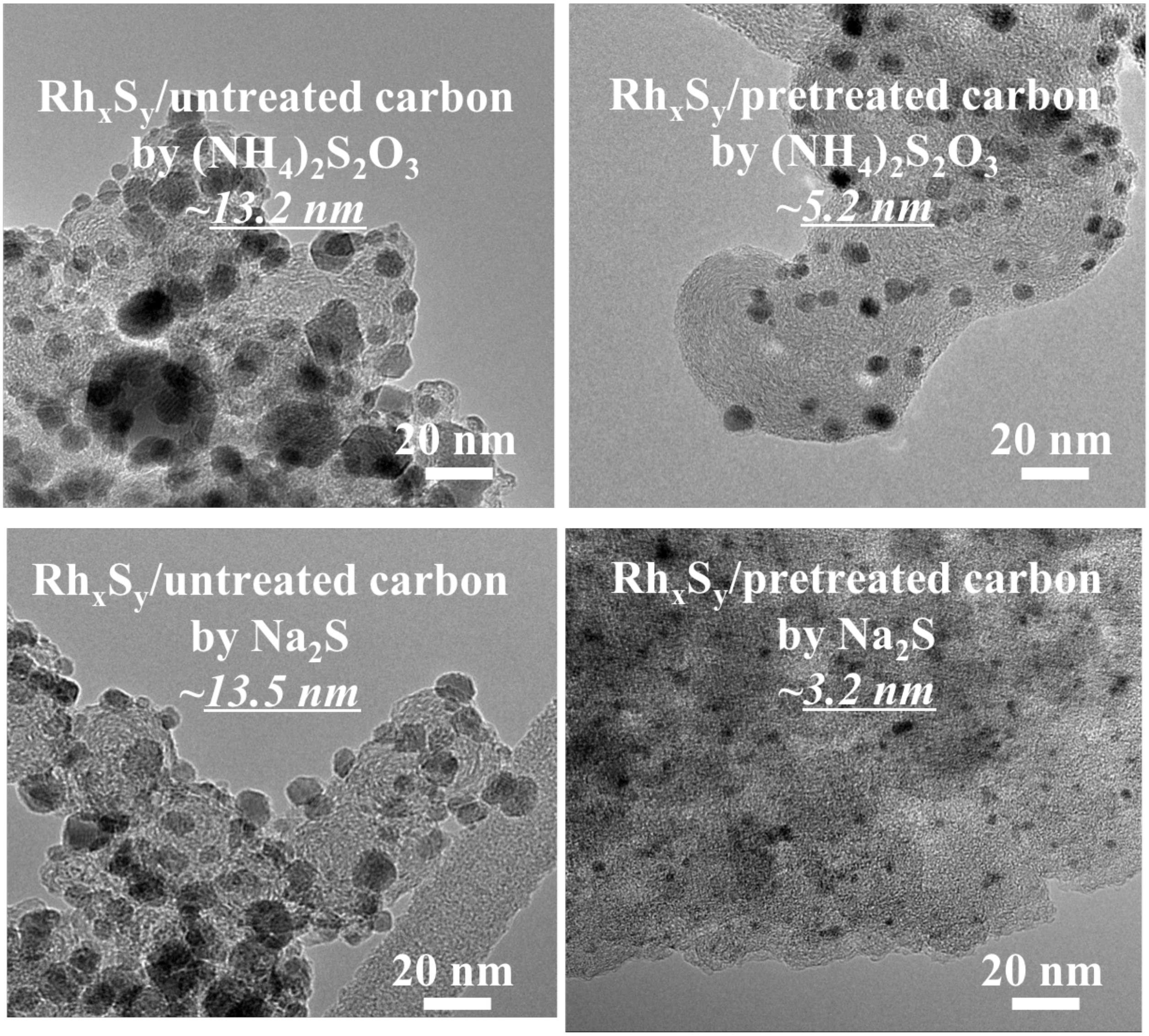

Figure 3.30. TEM pictures of rhodium sulfide catalyst synthesized on different substrates and sulfur sources (catalysts on pretreated carbon were synthesized with controlled addition rate of sulfur source. The TEM pictures of catalyst with faster addition rate of sulfur sources can be checked in Figure 3.21)

Compared to the TEM characterization, the CV method can measure the performance of the catalyst at the milligram level, which gives more accurate and credible results for the evaluation of mass-specific surface area. Figure 3.31 confirms that the mass-specific electrochemical surface area of catalyst synthesized by the Na_2S and pretreated carbon with the diffusion-controlled approach is highest among all the catalysts, which is almost 4 times higher than the conventional catalyst with the untreated carbon material and traditional sulfur source,($(NH_4)_2S_2O_3$. It is also worth noting that the higher activity of Rh_xS_y obtained with Na_2S is not altered by the slow addition rate of sulfur source.

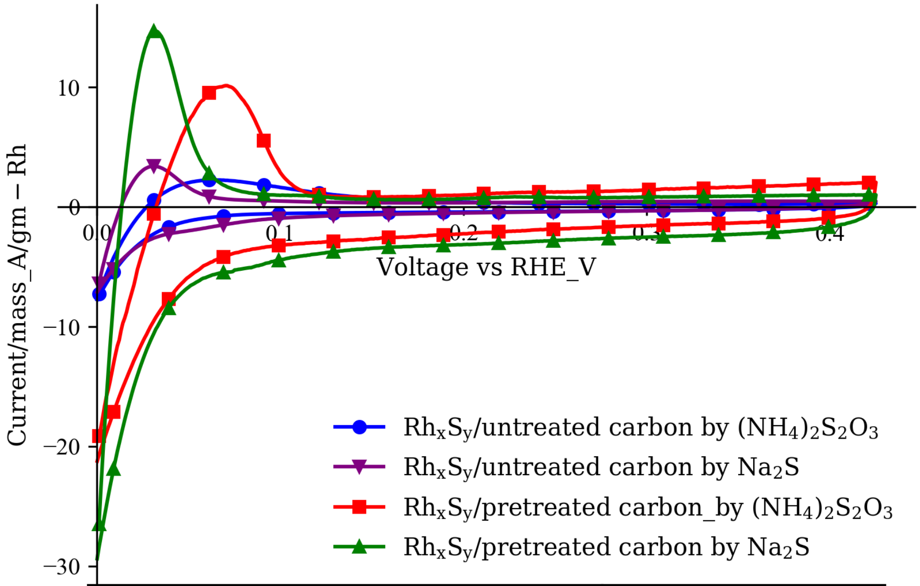

Catalyst	ECSA/mass_m^2/gm − Rh
Rh_xS_y/untreated carbon by $(NH_4)_2S_2O_3$	9.1
Rh_xS_y/untreated carbon by Na_2S	9.3
Rh_xS_y/pretreated carbon_by $(NH_4)_2S_2O_3$	36.5
Rh_xS_y/pretreated carbon by Na_2S	43.0

Figure 3.31. Cyclic voltammograms of rhodium sulfide synthesized by different carbon substrates and sulfur sources* (electrolyte: 1M N_2-saturated H_2SO_4 solution, working electrode: catalyst-coated GDE, counter electrode: Pt foil, reference electrode: SCE, scan rate: 10mV/s)
*catalysts on the pretreated carbon were synthesized with controlled addition rate of sulfur sources

3.4.5 Modification of Crystal Structure of Rh_xS_y Catalyst

As mentioned previously, the major difference observed in Figure 3.31 is the locations of the HOR peaks of catalyst synthesized by Na_2S and $(NH_4)_2S_2O_3$. Moreover, Figure 3.26 points out that the anion in the sulfur source is the key to the change in the activity of rhodium sulfide catalyst. The rhodium sulfide catalyst from Na_2S or K_2S has much smaller overpotential for the HOR compared to the Rh_xS_y by $(NH_4)_2S_2O_3$, which indicates that the rhodium sulfide from Na_2S has a higher catalytic activity for HOR. The activity test from the linear polarization curves in Figure 3.32 also confirms that. The slope in the figure indicates the activity of the catalyst based on the equation 2.2. The larger slope is, the higher activity the catalyst has. No matter on the untreated and pretreated carbon, the rhodium sulfide catalysts from Na_2S have the higher activity for the HOR/HER. Moreover, the catalysts synthesized on the untreated or pretreated carbon show similar active-area-specific activity which demonstrates that the functionalized support material does not affect the exchange current density of the catalyst. It is the sulfur source rather than the carbon substrate functionalization that changes the activity of the catalyst.

To explore the reasons of different activities of the catalysts synthesized by different sulfur sources, the XRD and XPS were used. In Figure 3.33(a), XRD results show that the functionalization does not change the crystal structures. The rhodium sulfide catalysts on the untreated carbon (blue and purple curves) and the pretreated carbon (red and green curves) have the similar XRD pattern, respectively. In the fingerprint region (2nd picture of Figure 3.33), the catalysts from different sulfur sources obvious have different characteristic peaks. For all the catalysts synthesized by the conventional sulfur source, $(NH_4)_2S_2O_3$, on the untreated/pretreated carbon, the sequence of the peak strength is $P4 > P1 > P3 > P2$, while the rhodium sulfide from the new sulfur source, Na_2S on the untreated/pretreated carbon has the $P1 > P4 > P3 > P2$ as the intensity order. The difference in the intensity order for the catalysts synthesized by $(NH_4)_2S_2O_3$ and Na_2S may come from the different crystal facets or the different crystal phases. The highly similar crystal patterns of $Rh_{17}S_{15}$ and Rh_3S_4 (3rd and 4th picture of Figure 3.33(a) respectively) make it difficult to answer this question. Moreover, the Rh_3S_4 phase is difficult to be detected by XRD due to its low crys-

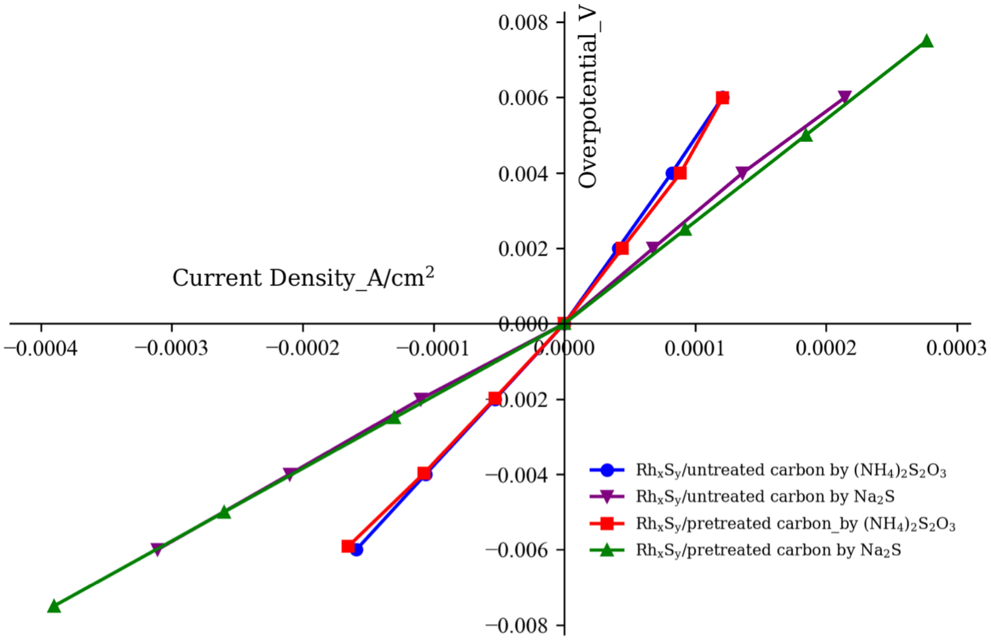

Catalyst	i_o (HOR) _A/cm^2	i_o (HER) _A/cm^2	i_o^*(HOR) _A/cm^2	i_o^*(HER) _A/cm^2
Rh_xS_y/untreated carbon by $(NH_4)_2S_2O_3$	0.47	0.62	0.43	0.56
Rh_xS_y/untreated carbon by Na_2S	0.56	0.81	0.52	0.76
Rh_xS_y/pretreated carbon by $(NH_4)_2S_2O_3$	0.46	0.64	1.68	2.32
Rh_xS_y/untreated carbon by Na_2S	0.58	0.82	2.49	3.51

Figure 3.32. Linear polarization curves of rhodium sulfide catalysts synthesized by different carbon substrates and sulfur sources (electrolyte: 1M hydrogen-saturated H_2SO_4 solution, rotation speed: 2400rpm, working electrode: RDE, counter electrode: Pt foil, reference electrode: SCE)

tallinity which makes the XRD not the proper tool to figure out this question.[53, 106] Synchrotron based XANES (X-Ray Absorption Near Edge Structure) may have enough energy to differentiate these two active phases.

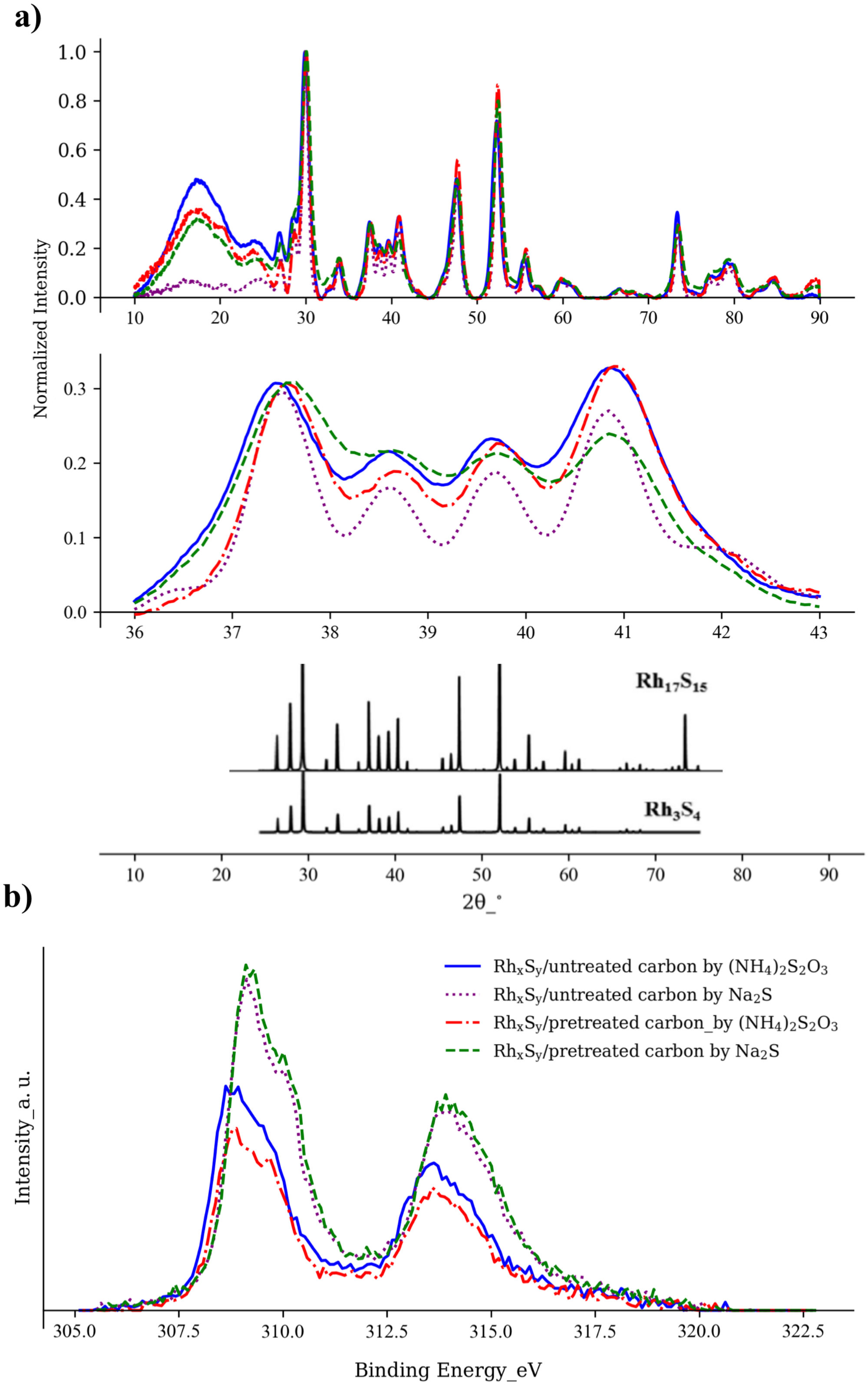

Figure 3.33. The structure chracterizations of rhodium sulfide synthesized by different carbon substrates and sulfur sources (a) XRD (Rh_3S_4 ICDS No. 410813, $Rh_{17}S_{15}$ ICDS No. 410838), (b)XPS of Rh 3d

To gain the insight of HOR/HER activity improvement, XPS was used to figure out the bonding information of the rhodium center. In Figure 3.33(b), the electrons on the Rh 3d orbital of rhodium sulfide on the pretreated/treated carbon from Na_2S have the higher energy (0.25 eV) than those of rhodium sulfide from $(NH_4)_2S_2O_3$, which indicates that the outer electronic structures of Rh are different for these two types of Rh_xS_y. The shifted peak position can be ascribed to the electronegativity of Rh (2.28) and S (2.58). The electrons of the bond tend to concentrate at the atom with the larger electronegativity. The less electron density of Rh 3d orbital (more positive peak in XPS) indicates the Rh atoms are bonded with more S atoms.[107] 50% of Rh atoms in the Rh_3S_4 with the space group $C2/m$ is fully coordinated by six surrounding S atoms, while the 75% of Rh atoms in the $Rh_{17}S_{15}$ with the space group $Pm\overline{3}m$ is only coordinated with four neighboring S atoms.[45,59] Based on this, it is hypothesized that the rhodium sulfide synthesized by Na_2S has more Rh_3S_4 from the positively shifted Rh 3d peak position. As suggested by the DFT calculation, the Rh_3S_4 is more active in catalyzing HOR/HER. Moreover, Rh-Rh bonds in the Rh, Rh_2S_3, Rh_3S_4, and $Rh_{17}S_{15}$ are 2.731, 3.208, 2.730, and 2.635 Å respectively. The similar Rh-Rh bonds lengths of Rh_3S_4 and Rh metal may help to explain the high activity of Rh_3S_4 in the HOR/HER catalysis except for the adsorption energy calculation for the H_2 on the rhodium sulfide cluster in the DFT research. Then the higher percentage of active crystal phase Rh_3S_4 may contribute to the higher activity of rhodium sulfide synthesized by the Na_2S.

The different crystal phase composition in the rhodium sulfide catalysts synthesized by two types of sulfur sources are hypothesized to be attributed to the different mechanisms of providing S^{2-} from $Na_2S/(NH_4)_2S_2O_3$ for the precipitation of Rh^{3+} and the standard Gibbs free energy change (ΔG) of the phase conversion from precursor Rh_2S_3 to the active phases $Rh_3S_4/Rh_{17}S_{15}$. As discussed in the Section 3.4.3, the $(NH_4)_2S_2O_3$ is slowly dissociated to sulfide anion via a two-step process in the aqueous solution. Moreover, the second step of dissociation is incomplete without the sulfidation reaction of rhodium cation and sulfide anion.

20% extra sulfur source was added in the synthesis of precursor to precipitate all the expensive rhodium. After all the Rh cations have been consumed, the 20% of additional thiosulfate anions are supposed to exist mostly in the form of $S_2O_3{}^{2-}$ rather than S^{2-}. In contrast to the slow and two-step dissociation of thiosulfate, the Na_2S is strong electrolyte which dissociates completely and quickly. Then the 20% extra Na_2S exists as S^{2-} form after all the precipitation of Rh^{3+}. The extra S^{2-} may be either left on the precursor surface or incorporated into the amorphous Rh_2S_3 particles due to its small size and affinity with the coordinated sulfur atoms in the precursor.

After the synthesis of Rh_2S_3, the thermal treatment at 700°C was used to convert the non-active phases to the active phases Rh_3S_4 and $Rh_{17}S_{15}$. The molecular formulas of these three rhodium sulfides show that the thermal treatment is a reduction process in which the sulfur atoms are removed. With the extra sulfide ions, the ΔG of conversion from $Rh_{17}S_{15}$ to the Rh_3S_4 is around -85kJ/mol at 700°C which indicates that this conversion is spontaneous.[108] Based on the phase diagram and the dissociation mechanisms, it is hypothesized that the extra sulfide anions provided by extra Na_2S facilitate the formation of active crystal phase Rh_3S_4 in the process of thermal treatment.

Figure 3.34 proves this hypothesis. The rhodium sulfide catalysts from 120% $(NH_4)_2S_2O_3$ and Na_2S have the HOR peaks at 71 and 43mV respectively. When the surplus Na_2S decreases from 120% to 103%, the HOR peak shifts positively from 43 to 55 mV, which indicates lower activity in catalyzing the HOR reaction. This decrease can be attributed to the lack of extra sulfide anions in the thermal treatment to generate enough active phase Rh_3S_4. Though without the experiment with more extra sodium sulfide (>120%), it can be hypothesized that it may have the negative effect on the activity of rhodium sulfide catalyst because the ΔG of conversion from Rh_3S_4 to the Rh_2S_3 is also negative at 700°C.

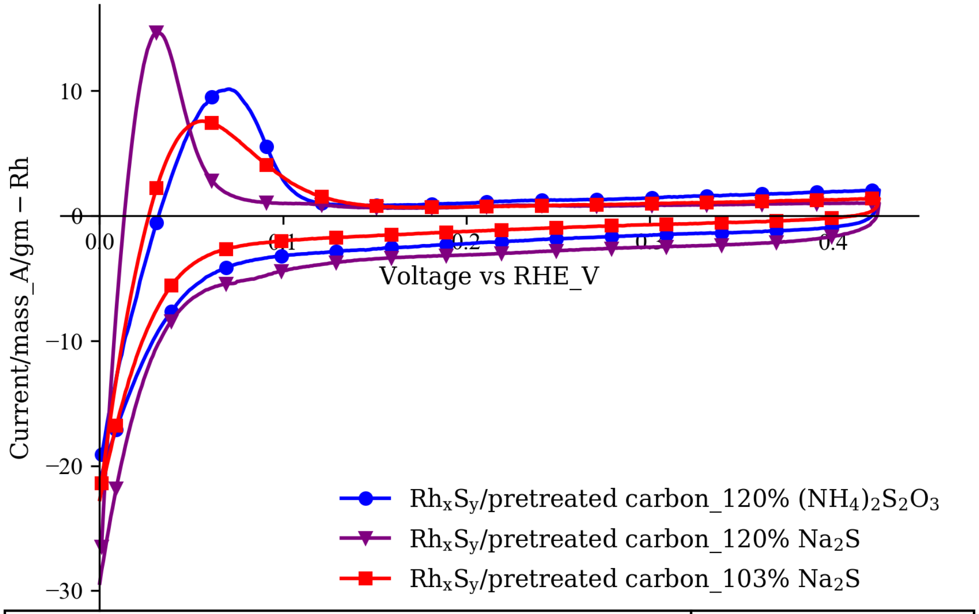

Catalyst	HOR peak_mV
Rh_xS_y/pretreated carbon_120% $(NH_4)_2S_2O_3$	71
Rh_xS_y/pretreated carbon_120% Na_2S	43
Rh_xS_y/pretreated carbon_103% Na_2S	55

Figure 3.34. Cyclic voltammograms of rhodium sulfide catalysts from different surplus sulfur sources (electrolyte: 1M N_2-saturated H_2SO_4 solution, working electrode: catalyst-coated GDE, counter electrode: Pt foil, reference electrode: SCE, scan rate: 10mV/s)

3.4.6 Catalysis Activity of Rh_xS_y in HBr Solution

Rh_xS_y is a promising catalyst for the HBr PEM electrolyzer due to its activity and durability in the corrosive environment. To evaluate the performance of Rh_xS_y in the HBr electrolysis, the multi-step chronoamperometry was measured in the 2M HBr solution. The results are shown in Figure 3.35. The activity of Rh_xS_y in HBr is relatively smaller than that of Rh_xS_y in H_2SO_4 solution, which may be due to the adsorption of Br^- on the active surface. Though the rhodium sulfide catalyst is free from the corrosion of HBr/Br_2, it still suffers from the poisoning of Br^- on the active sites which temporarily blocks them. This contamination is not permanent and can be removed by soaking the catalyst in the hot DI water (around 80 °C) to desorb the bromide or operating in the HER mode.

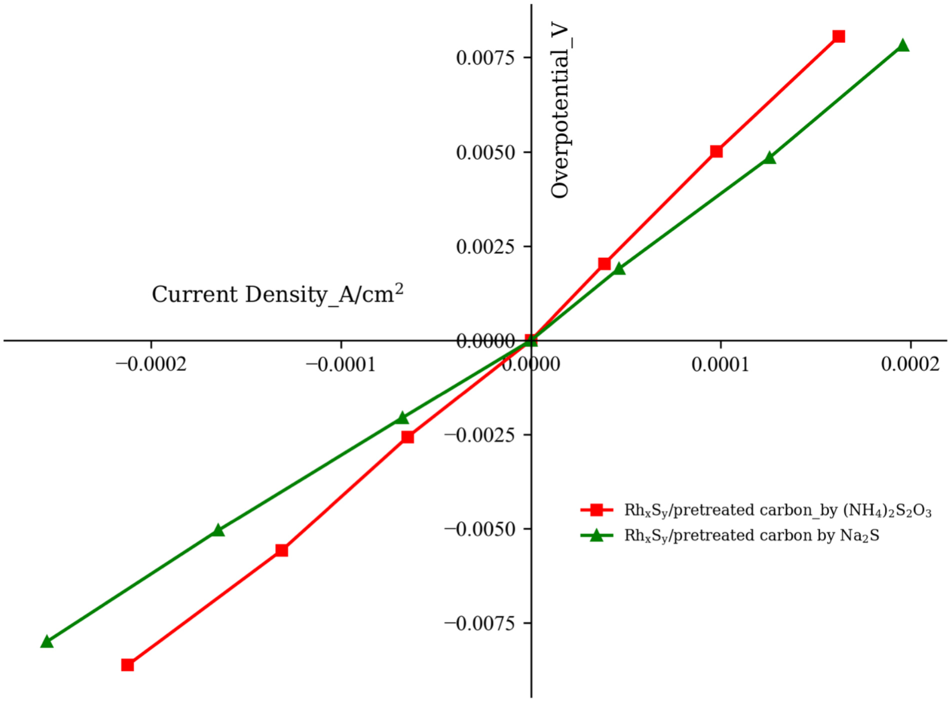

Catalyst	i_o (HOR) _A/cm^2	i_o (HER) _A/cm^2	i_o^*(HOR) _A/cm^2	i_o^*(HER) _A/cm^2
Rh_xS_y/pretreated carbon by $(NH_4)_2S_2O_3$	0.42	0.52	1.53	1.87
Rh_xS_y/pretreated carbon by Na_2S	0.56	0.81	2.15	2.8

Figure 3.35. Linear polarization curves of rhodium sulfide catalysts synthesized by different carbon substrates and sulfur sources in 2M H_2-saturated HBr solution (electrolyte: 1M hydrogen-saturated H_2SO_4 solution, rotation speed: 2400rpm, working electrode: RDE, counter electrode: Pt foil, reference electrode: SCE)

3.4.7 Summary

A rhodium sulfide catalyst with a high mass-specific surface area and active crystal structure was synthesized and characterized in this section. The functionalized carbon material discussed in Section 3.3 was applied to the catalyst synthesis to reduce the size of NPs in this part, while the NPs growth model was optimized as the diffusion-controlled one for the further particle size and distribution control. It has been proven in this section that the diffusion-controlled NPs growth process is preferable for the small particle size and narrow size distribution. Moreover, the rhodium sulfide synthesized by the new sulfur source, Na_2S is found to be more active than the catalyst from the traditional sulfur source,$(NH_4)_2S_2O_3$. The discussion in this section shows that the fast, complete and spontaneous release mechanism of S^{2-} of Na_2S provide the extra S^{2-} in the amorphous Rh_2S_3 precursor which helps to form the active Rh_3S_4 phase in the thermal treatment due to the negative ΔG of conversion from $Rh_{17}S_{15}$ to Rh_3S_4 with the extra sulfur.

3.5 Highly Dispersed Rh_xS_y Catalyst on Carbon Support with High Nafion Affinity for HER/HOR in H_2-Br_2 Reversible Fuel Cell

In Section 3.3, a rhodium sulfide catalyst with the high mass-specific surface area but low Nafion affinity was synthesized and discussed. Its mass-specific activity for HOR/HER catalysis was further improved by using a diffusion-controlled NPs growth model and the usage of the new sulfur source, Na_2S. Then the Nafion affinity issue becomes the only weakness for its application in the H_2-Br_2 fuel cell. In the catalyst synthesis, the ketone functional group was created on the carbon surface to achieve better adsorption and dispersion of rhodium cations when the pH of the solution is lower than the point of zero charge (PZC) of the adsorbent. The existence of the ketone groups on the activated carbon, however, shows a repulsive effect to the Nafion ionomer in the catalyst ink which reduces the effective Nafion-covered catalyst surface area on the negative (hydrogen) electrode. A high mass transportation resistance was observed in the fuel cell test with rhodium sulfide catalyst on the pretreated carbon dominated by the ketone surface group. To solve this problem, a method to synthesize a rhodium sulfide catalyst with high mass-specific activity and Nafion affinity was attempted and will be discussed in this section.

3.5.1 Conversion of Surface Functional Groups

The functional groups on the supporting carbon material can facilitate the adsorption and dispersion of metal ions in the synthesis, which finally leads to a better distribution of nanoparticles. There are two major types of functional groups on the carbon surface, acidic and basic ones. The adsorption mechanisms of metal ions on the carbon surface with these two types of groups are different. The adsorption of metal ions on the carbon surface with the acidic surface groups like carboxylic group mainly comes from the ion exchange (outer-sphere electron exchange) and the formation of the metal complex (inner-sphere electron exchange). The outer/inner-sphere electron exchange locates at the charged oxygen-containing functional groups of which the prerequisite is the electrostatic affinity between the ions and charged adsorption sites at oxygen functional groups.

Then the relationship between the pH of the solution and PZC of the adsorbent determines whether the adsorption of metal ion prefers the carbon with carboxylic groups or not. This topic has been discussed in detail in Section 3.3. The basic surface functional group facilitates the metal ion adsorption by the Cπ interaction between the electron-rich conjugated structures of carbon surface and the electron-deficient metal cation. The electron cloud density of aromatic rings on the carbon surface is enhanced by the lone pair of electrons of oxygen in the ketone group. Since the main adsorption centers are the conjugated structures rather than the oxygen-containing functional groups, the electrostatic affinity is no longer critical for the case of adsorption on the carbon surface. These two mechanisms of metal ion adsorption cannot co-exist due to the electron-withdrawing nature of the carboxylic groups which is supposed to reduce the electron density of the conjugated structures on the carbon surface. The details of the adsorption mechanisms can be found in Section 3.3.

It has been proven that the ketone functional group is preferable for the adsorption of rhodium cation when the pH of rhodium chloride solution is lower than the PZC of the carbon (oxygen-containing groups on the carbon surface are positively charged). However, the Rh^{3+}-friendly surface group, ketone, shows repulsive effect with the Nafion ionomer which serves as the ionic pathway in the fuel cell operation. The repulsion between the ketone groups on the carbon surface and Nafion ionomer reduces the active catalyst surface area and increases the mass transfer resistance. Then the roadmap to solve this problem becomes clear, the ketone group is necessary for the catalyst synthesis stage but has to be removed or converted into the Nafion-friendly carboxylic group before its usage in a PEM-based fuel cell.

When the Nafion-unfriendly ketone groups are removed, the clean carbon surface acts like untreated carbon or at least does not show the repulsion with the Nafion ionomer, as shown in Figure 3.24. The typical thermal decomposition temperature for the ketone group on the carbon surface is from 700 to 900°C, which is higher than the thermal treatment temperature of rhodium sulfide catalyst.[86] The high temperature in the thermal treatment will result in the formation of corrodible metallic rhodium. The addition of hydrogen may allow the conversion of the ketone group at lower temperature but may also reduce the rhodium sulfide to rhodium metal. Then the only possible solution is to convert the ketone group into the carboxylic group. Two approaches have been developed to transform the ketone group to the carboxylic group and will be discussed next.

3.5.1.1 Electrochemical method

The conversion of the ketone to the carboxylic/ester group is an oxidation reaction due to the adding of an oxygen atom in the chemical formula. It was then proposed to accomplish using an electrochemical process. The carbon with ketone group (blue curve) and the carbon with the carboxylic group (purple curve) were scanned from 400 mV to 1.1 V vs. RHE respectively to get their oxidation potentials in Figure 3.36. It is found that the oxidation potential of the carbon with ketone group is around 610 mV while that of the carbon with the carboxylic group is around 650 mV. The difference of the oxidation potentials of the carbon with ketone/carboxylic group proves the functional groups on the carbon surface and their redox reactions are different. Then the carbon with ketone group was held at 1.2 V vs. RHE for 1 h to oxidize the ketone group to the carboxylic group. After the oxidation at 1.2 V vs. RHE, it is found that the oxidation potential shifts positively and becomes closer to the peak of the carbon with the carboxylic group. However, the capacitive current reduces by 50% compared to that of the carbon without the oxidation, which indicates a loss of the surface area of the carbon.[109] It can be inferred that the catalyst on the carbon surface could be lost when the carbon substrate is oxidized from the long oxidation exposure while the surface functional group can be converted to the carboxylic group. So, even though the electrochemical method is green and takes a shorter time to finish, it has to be given up due to the concern of the loss of catalyst.

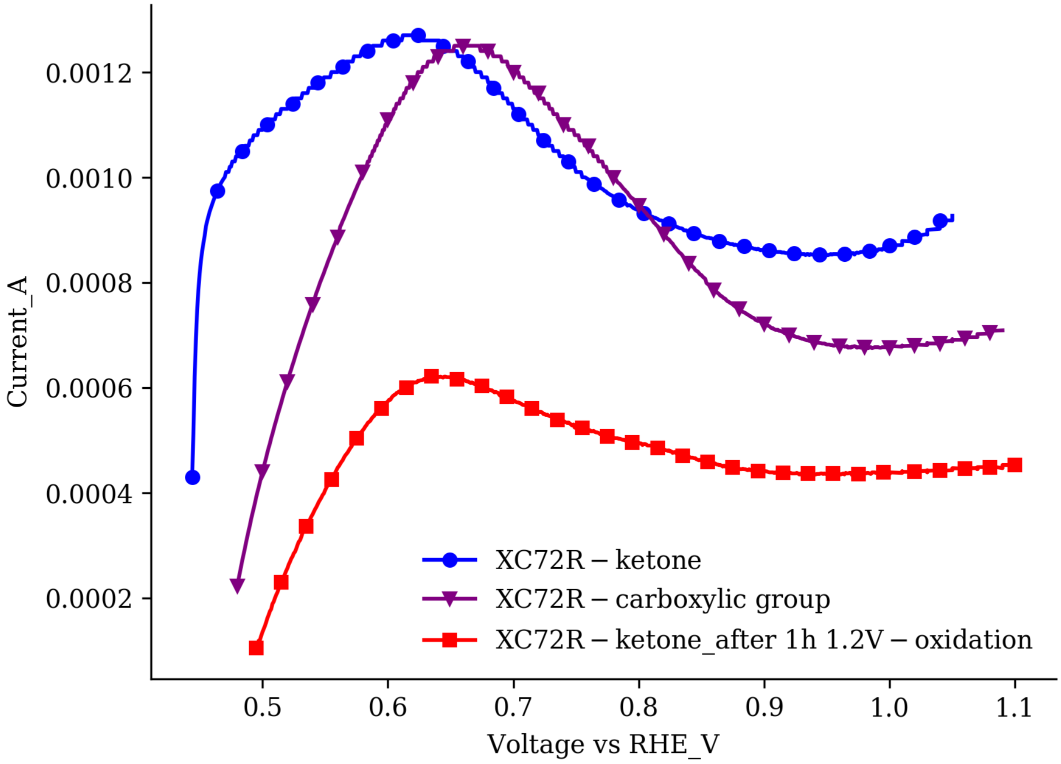

Figure 3.36. Oxidation potentials of carbon with different functional groups (electrolyte: 1M N_2-saturated H_2SO_4 solution, working electrode: catalyst-coated GDE, counter electrode: Pt foil, reference electrode: SCE, scan rate: 10mV/s)

3.5.1.2 Organic method

Since the electrochemical method cannot convert the ketone group into the carboxylic group and maintain the integrity of loaded catalyst particles at the same time, an organic chemical method was developed for the conversion. The Baeyer-Villiger reaction shown in Figure 3.37 can convert the ketone group into the ester group which can be further hydrolyzed to the carboxylic group in the acid.[110] In Baeyer-Villiger reaction, the oxidant is provided by the H_2O_2, and 9-Mesityl-10-methylacridinium perchlorate is used as the catalyst. Two solvents, water and methanol, were explored.

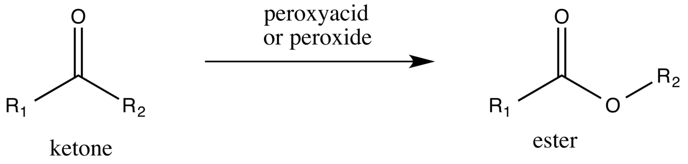

Figure 3.37. Baeyer-Villiger reaction

The carbons with ketone group were mixed with the catalyst and oxidant in the water and methanol, respectively, for the Baeyer-Villiger reaction. Then the carbons were hydrolyzed in the hydrochloride acid to get the carboxylic group. Figure 3.38 shows the FT-IR spectra of carbon using water as solvent (purple) and carbon using methanol as solvent (red) in the Baeyer-Villiger reaction. It is found that the carbon reacted with water as the solvent (purple) is free from the characteristic peaks of the carboxylic group while the carbon with methanol as the solvent (red) shows the two characteristic peaks at 680 and 2300 cm^{-1} of the COO^- bending and O-H of COOH stretching respectively. The FT-IR spectra prove that only the organic solvent, methanol, can help to finish the conversion from the ketone group to the carboxylic group. Figure 3.38 also shows that the carbon after 1.2 V oxidation (black) has small peaks at 680 and 2300 cm^{-1} which proves that the electrochemical method can convert part of the ketone groups into the carboxylic groups.

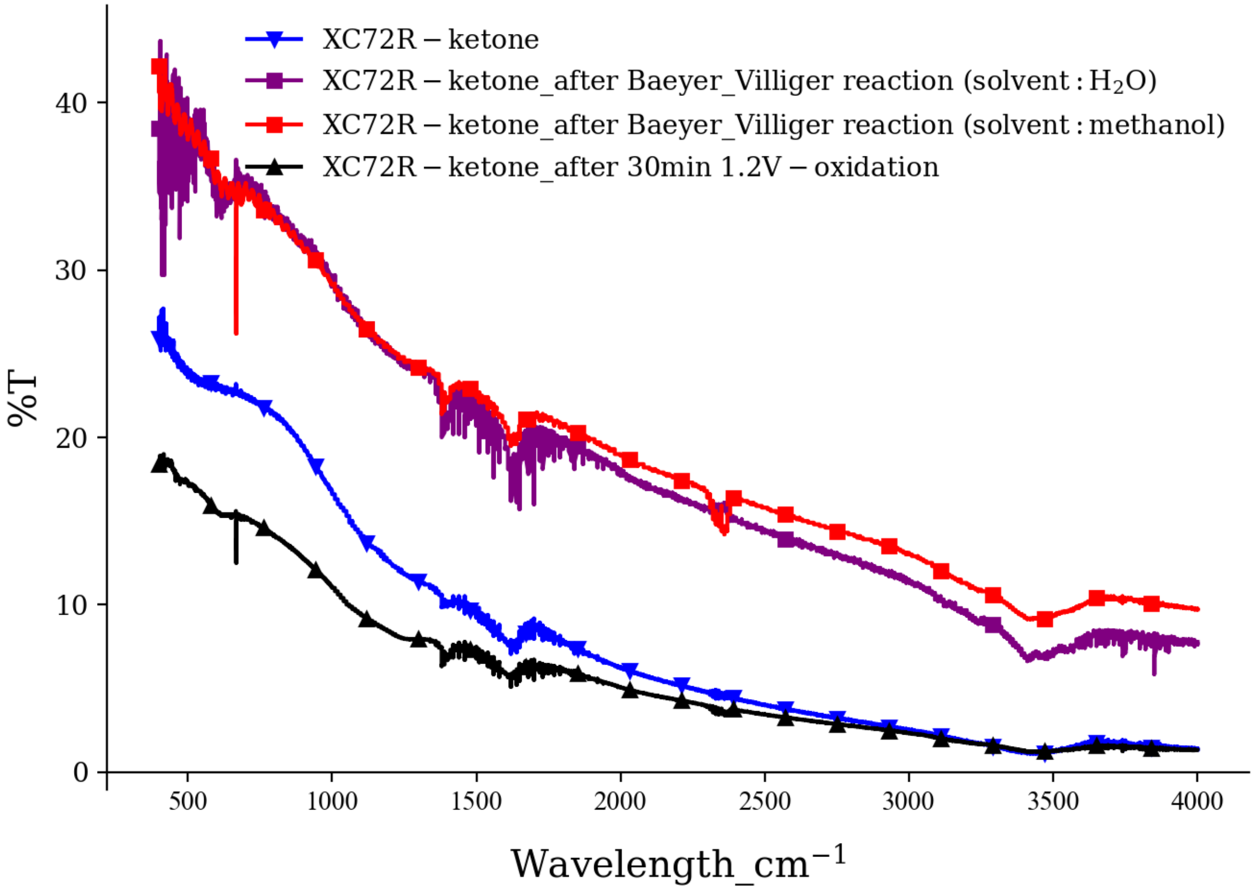

Figure 3.38. FT-IR spectra of different carbons

3.5.2 Characterization of the Catalysts after the Surface Functional Group Conversion

Since Section 3.4 has proven that the rhodium sulfide catalyst synthesized by Na_2S has higher activity in the HOR/HER catalysis, all the characterizations discussed below are about the Rh_xS_y/pretreated carbon synthesized by Na_2S. After the transformation from the ketone groups to the carboxylic groups has been confirmed by the FT-IR, the next concern is whether the organic reactions (Baeyer-Villiger and ester hydrolysis reaction) will affect the loaded rhodium sulfide nanoparticles.

The CV of the Rh_xS_y catalyst/pretreated carbon before and after the organic reactions can answer this question. In Figure 3.39, Rh_xS_y/pretreated carbon before the organic reactions (blue) and the Rh_xS_y/pretreated carbon after the organic reactions (red) show almost exact cyclic voltammograms. The unchanged HOR peak size reveals that the mass-specific electrochemical surface area of rhodium sulfide NPs does not change after the organic reactions. The HOR peak location was used as the indicator of activity which directly relates to the crystal phase of the rhodium sulfide. The shifted peak location may come from the adjusted composition of Rh_3S_4 in the total Rh_xS_y as discussion of Section 3.4. Higher percentage of active Rh_3S_4 in the total Rh_xS_y contributes to the negatively shifted HOR peak position. The unvaried HOR peak positions in Figure 3.39 show the stable composition in the mixed crystal Rh_xS_y phase during the organic reactions. It is also noted that the capacitive currents of both Rh_xS_y/pretreated carbon before and after the organic reactions remain the same which shows that the integrity of the carbon substrate was not affected in the conversion process.

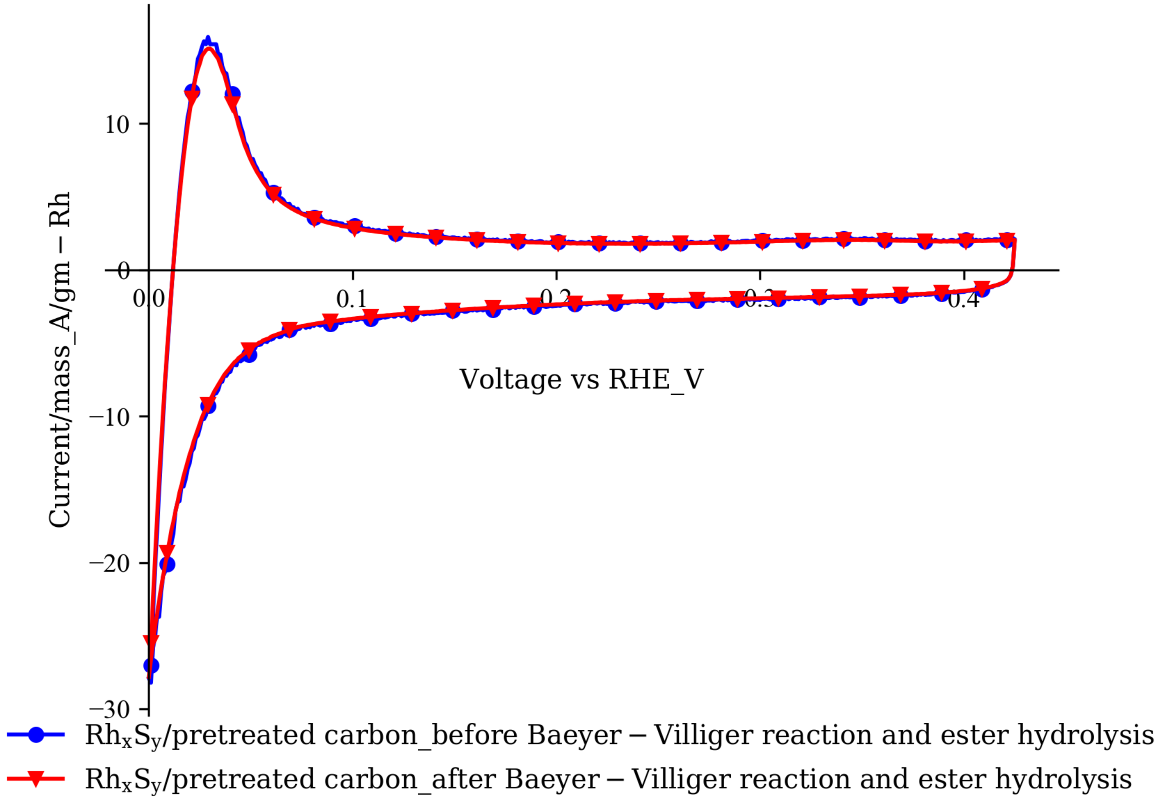

Figure 3.39. Cyclic voltammgrams of rhodium sulfide catalysts on the pretreated carbon before and after the Baeyer-Villiger reaction and ester hydrolysis (electrolyte: 1M N_2-saturated H_2SO_4 solution, working electrode: catalyst-coated GDE, counter electrode: Pt foil, reference electrode: SCE, scan rate: 10mV/s)

The XRD in Figure 3.40 confirms the stable crystal structure, and the unchanged mass specific surface area of rhodium sulfide catalyst can be further verified by the TEM in Figure 3.41. The two TEM pictures before and after the organic reactions demonstrate that the average particle size and dispersion do not change during the Baeyer-Villiger reaction and ester hydrolysis which supports the results of CV in Figure 3.39.

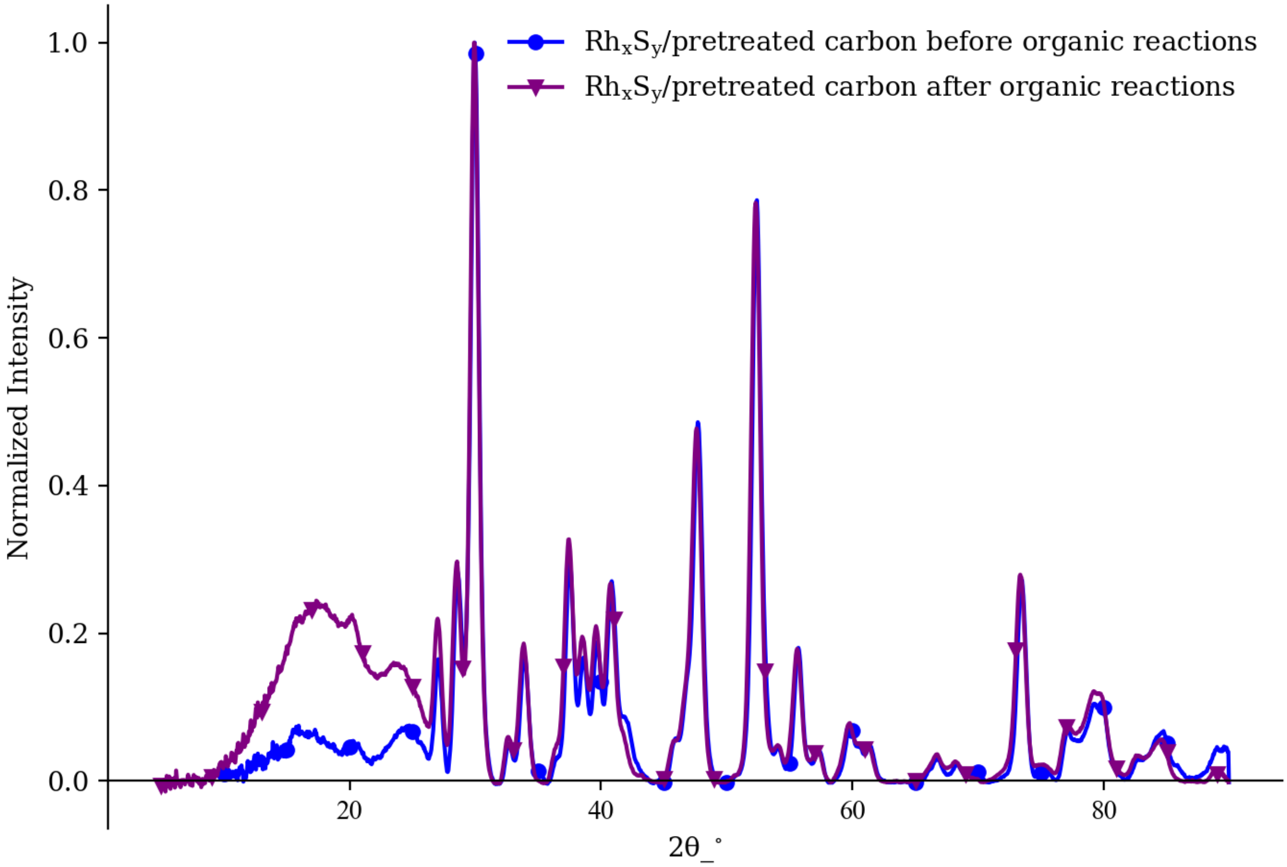

Figure 3.40. XRD patterns of the Rh_xS_y/pretreated carbon before and after the Baeyer-Villiger reaction and ester hydrolysis

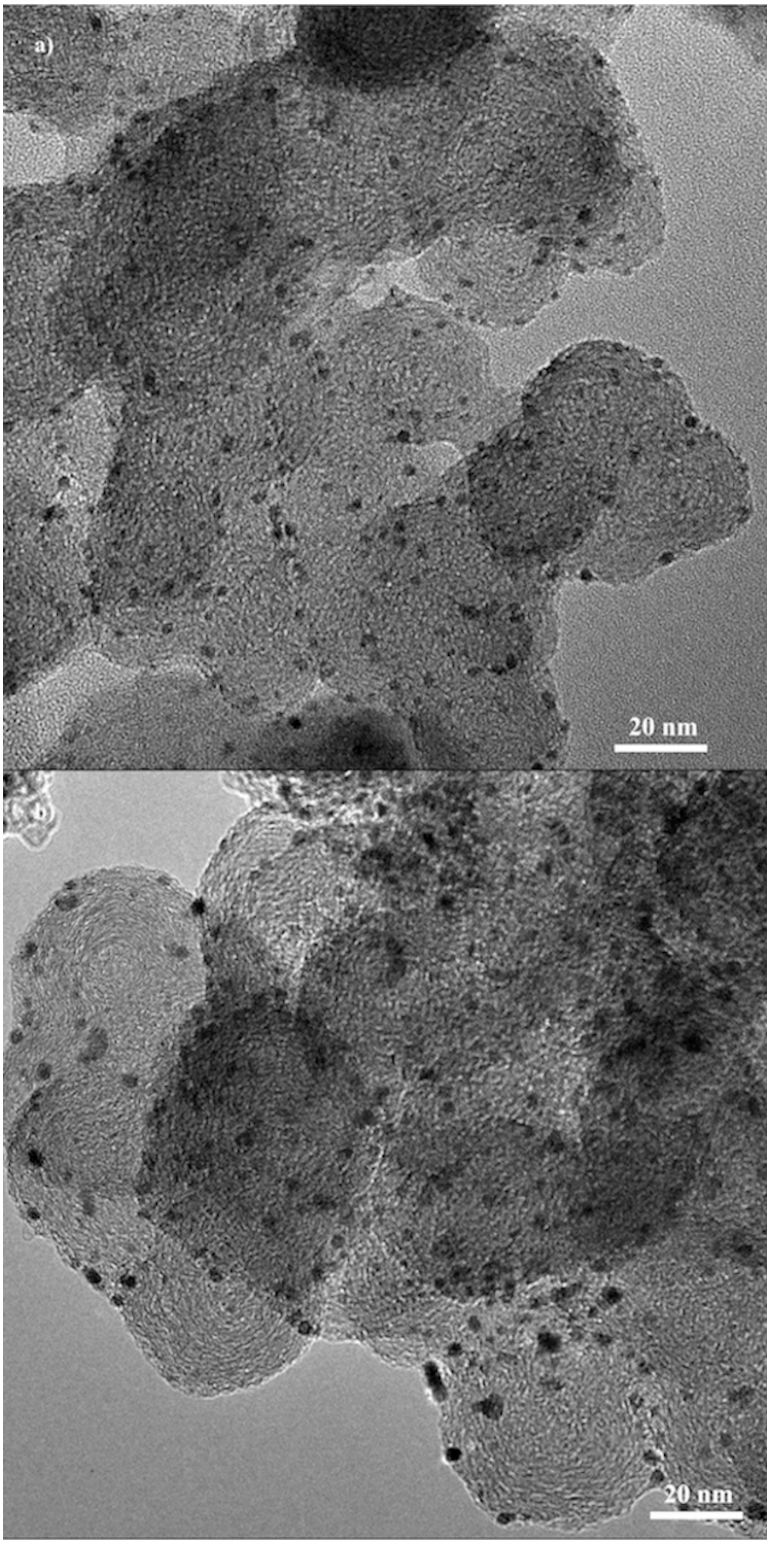

Figure 3.41. TEM pictures of the Rh_xS_y/pretreated carbon (a) before and (b) after the Baeyer-Villiger reaction and ester hydrolysis

3.5.3 Fuel Cell Tests

Figure 3.42 shows the charge and discharge polarization curves of H_2-Br_2 fuel cells with Rh_xS_y on untreated carbon and pretreated carbon with/without surface functional group conversion from the different sulfur sources used on the negative hydrogen electrode. These polarization curves have been corrected for IR losses. The polarization curves were fully IR corrected to remove the effect of all ohmic resistances in the fuel cell, including the resistance from the membrane, which allowed us to study the kinetics and mass transfer effects.

Though the functionalized carbon has been proven to improve the mass-specific surface area of rhodium sulfide catalyst by the TEM (Figure 3.21 and 3.30) and CV in the aqueous electrolyte (Figure 3.19 and 3.31), the catalyst/pretreated carbon without surface functional group conversion (purple curves in Figure 3.42(a) and (b)) demonstrates unexpected high mass transfer resistance in the high current density region when tested in the $H_2 - Br_2$ fuel cell. The unsatisfactory performance of the catalyst/pretreated carbon without surface functional group conversion in the fuel cell may be due to the repulsion effect between the Nafion-unfriendly ketone surface group and Nafion ionomer, which results in a non-uniform distribution of the Nafion on the pretreated carbon surface. Furthermore, the repulsive force leads to an excessively thick Nafion polymer layer in the covered area ($Thickness_{Nafion} = Volume_{Nafion}/Area_{Nafion-friendly\ area}$). The thicker Nafion layer can be expected when the Nafion-friendly area on the carbon surface is smaller for the carbon dominated by the ketone group. The high mass transportation resistance was not observed in the charge curves of the fuel cell with the catalyst/pretreated carbon without surface functional group conversion. In the charge reaction of the fuel cell, the hydronium ions, which are reduced to the hydrogen molecules come from not only the Nafion polymer but also the crossover HBr acid. This is why the non-uniform distribution of Nafion ionomer on the carbon surface has no effect on the access of hydronium ions. Consequently, fuel cells with a higher active surface area delivered higher charge performance.

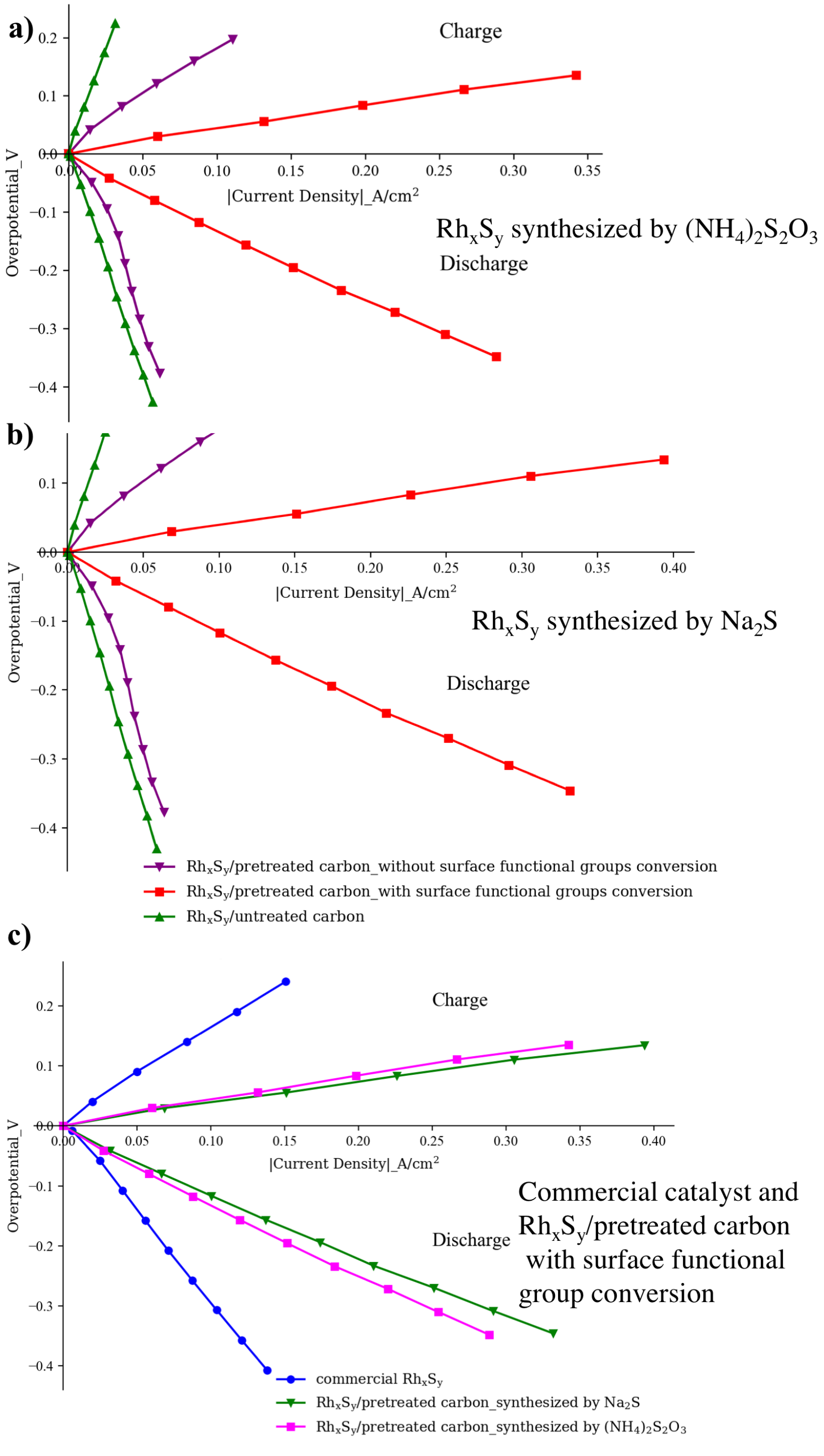

Figure 3.42. H_2-Br_2 fuel cell discharge and charge polarization curves of different catalysts after full IR correction (Nafion:catalyst=1:1) (a) Rh_xS_y synthesized by $(NH_4)_2S_2O_3$ (b)Rh_xS_y synthesized by Na_2S (c) Rh_xS_y from BASF and with surface functional group conversion

To solve the affinity issue between the ketone groups on the carbon surface and the Nafion ionomer, the Baeyer-Villiger reaction and ester hydrolysis were used to convert the ketone group to the Nafion-friendly carboxylic group, which was confirmed in the FT-IR spectra in Figure 3.38. The organic reactions have been convinced to be safe for the loaded rhodium sulfide catalyst in Figure 3.41,3.40 and 3.39. The excellent performance in the kinetics-controlled region of the Rh_xS_y/pretreated carbon with surface functional group conversion from $(NH_4)_2S_2O_3$ and Na_2S (red curves in Figure 3.42(a) and (b)) fully demonstrates the efforts of reducing the nanoparticle size and narrowing the distribution by using the functionalized carbon and diffusion-controlled nanoparticle growth process. Moreover, the mass transfer limitation effect in the fuel cell with the catalyst/pretreated carbon without surface functional group has been addressed. This promising result supports the hypothesis that the mass transfer limitation of the fuel cell is caused by the non-uniform distribution of Nafion ionomer on the carbon surface in Section 3.3. When the ketone groups are transformed into the carboxylic groups, the repulsion between the carbon and the Nafion ionomer is eliminated. The uniformly distributed Nafion ionomer covers all the high mass-specific Rh_xS_y catalyst particles on the Nafion-friendly carbon surface making all the catalyst surface accessible in the HOR/HER for the fuel cell operation, resulting in excellent performance. Furthermore, the high Nafion-friendly surface area on the supporting carbon reduces the thickness of Nafion thickness which eliminates high mass transfer resistance observed with the carbon with ketone group. In Figure 3.42(c), the fuel cell performances of Rh_xS_y/pretreated carbon with surface functional group conversion from $(NH_4)_2S_2O_3$ and Na_2S are compared to that of the commercial catalyst from BASF. It can be seen that Rh_xS_y/pretreated carbon from Na_2S achieves the highest performance in the charging and discharging operation which is 4.5 and 2.8 times higher than those of the commercial catalyst respectively.

3.5.4 Summary

The previous research developed a rhodium sulfide catalyst with a high mass-specific activity of HOR/HER catalysis by the usage of functionalized supporting carbon material, the diffusion-controlled growth process for the nanoparticle, and the new sulfur source Na_2S. However, the excellent performance of the new Rh_xS_y catalyst was not fully demonstrated in the fuel cell operation due to the affinity issue caused by the ketone group on the functionalized carbon material. Then Baeyer-Villiger reaction and ester hydrolysis were used to convert the Nafion-unfriendly ketone group into the Nafion-friendly carboxylic group. The results from the cyclic voltammetry, TEM, and XRD confirm that the mass-specific electrochemical surface area (ECSA/mass), average particle size and crystal phase composition do not change in the organic reaction process. The H_2-Br_2 fuel cell tests demonstrate that the Rh_xS_y/pretreated carbon with surface functional groups conversion outperform all other rhodium sulfide catalysts including the commercial one. The mass transfer limitation of the Rh_xS_y on the pretreated carbon with ketone group was eliminated in the fuel cell with Rh_xS_y on the carboxylic-dominated carbon. Besides the development of the practical catalyst for the negative electrode of H_2-Br_2 fuel cell, this section also provide a method to tune the types of functional groups on the carbon surface which may be applied in the other fields like heavy metal cation adsorption, the carbon nanotube (CNT) functionalization, and the development of metal-free catalyst.

Chapter 4

Future work and Recommendation

4.1 Future Work

4.1.1 Modification to the Aqueous Synthesis Method of Rhodium Sulfide

The ketone group on the carbon surface created in the process of functionalization is necessary for the adsorption of Rh^{3+} when the PZC of adsorbent is larger than the pH of the solution. However, the existence of the ketone group imposes the adverse effect on the uniform distribution of Nafion ionomer on the carbon surface. The time-consuming Baeyer-Villiger reaction and ester hydrolysis were developed to convert the ketone group into the carboxylic group. An attempt to increase the pH of $RhCl_3$ to be higher than the PZC of the adsorbent which is supposed to create the electrostatic attraction between the positively charged rhodium cation and the negatively charged carboxylate anion was reported in Section 3.3. However, it failed due to the precipitation reaction between the added hydroxide group and the Rh cation. The proposed solution to control the adding rate of ammonia water very carefully and stir the solution vigorously to avoid the high local concentration of the hydroxide group. The reaction between the hydronium ion and hydroxide group should be faster than the reaction between the Rh cation and hydroxide group due to the reaction mechanism and the size of ions. If the local concentration of hydroxide is well controlled, then the precipitation of rhodium cation may be avoided. After the pH of $RhCl_3$ solution is adjusted to be higher than the PZC of the adsorbent (3-4 for the carbon with the carboxylic group), the activated carbon with the carboxylic group can be directly used for the adsorption of rhodium cation in the synthesis. Then the surface functional group conversion can be avoided.

The adsorption of rhodium cation on the carbon with the carboxylic group is through the ion exchange/surface complex formation, which indicates that all the carboxylic group created in the functionalization process should be covered by the adsorbed rhodium cation and subsequent rhodium sulfide amorphous particles. After the thermal treatment, the carbon should be functional group-free, just like the untreated carbon. The untreated carbon does not show any repulsion with the Nafion ionomer. If the distribution of Nafion ionomer needs to be enhanced, the catalyst can be electrospun to the Nafion ionomer which creates a more uniform distribution of Nafion ionomer on the carbon surface.[111]

4.1.2 Development of the Gaseous Synthesis Method of Rhodium Sulfide

Facing the challenges brought by the aqueous synthesis method, the gaseous synthesis method may be used in future research. The gaseous sulfur sources like H_2S and CS_2 instead of the aqueous Na_2S solution will be used. In the gaseous synthesis method, the anionic $(RhC_6)^{3-}$ will provide the source of rhodium. Then the carbon with carboxylic groups can be used as supporting material since the anionic rhodium precursor can be adsorbed on the positively charged active sites by the formation of the metal surface complex when the PZC of carbon is larger than the pH of the solution. The adsorbed $(RhC_6)^{3-}$ will react with H_2S and CS_2 to form metal sulfide at certain temperature. Moreover, the carboxylic group also shows good affinity with Nafion ionomer which can facilitate the fuel cell performance due to the homogeneous distribution of Nafion ionomer in the catalyst layer. It may have other advantages from the gaseous synthesis method like potentially low particle size and better durability in the long-term fuel cell operation.

4.2 Contributions to this Area

- **Y. Li** and T. V. Nguyen, “New Process to Synthesize Highly Active and Dispersed Rh_xS_y Catalyst for HOR/HER in HBr solution." (**Manuscript in Preparation**)

- **Y. Li** and T. V. Nguyen, “Highly Dispersed Rh_xS_y Catalyst on Carbon Support with High Nafion Affinity for HER/HOR in H_2-Br_2 Reversible Fuel Cell." (**Manuscript in Preparation**)
- **Y. Li** and T. V. Nguyen, “Synthesis and Evaluation of Rh_xS_y Catalyst with Functionalized Carbon for HOR/HER in H_2-Br_2 Reversible Fuel Cell”, *Journal of Electrochemical Society*, 165 (14): F1139-F1146,2018.
- **Y. Li** and T. V. Nguyen, “Core-Shell Rhodium Sulfide Catalyst for Hydrogen Evolution Reaction / Hydrogen Oxidation Reaction in Hydrogen-Bromine Reversible Fuel Cell." *Journal of Power Sources*, 382:152–159, 2018.
- R. P. Dowd Jr., A. Verma,**Y. Li**, D. Powers, R. Wycisk, P. N. Pintauro, and T. Van Nguyen, “A Hydrogen-Vanadium Reversible Fuel Cell Crossover Study." *Journal of the Electrochemical Society*, 164(14): F1608–F1614, 2017.
- **Y. Li** and T. V. Nguyen, “Core-Shell Rhodium Sulfide Catalyst for HER/HOR in HBr Solution." *ECS Transactions*, 72(10):19–26, 2016.

Chapter 5

Conclusions

Catalyst development is a key factor in the development of the H_2-Br_2 fuel cell. Though rhodium sulfide catalyst is stable in the corrosive HBr environment, it suffers from the low activity of HOR/HER catalysis and the low mass-specific surface area. A series of methods have been discussed in this dissertation including the usage of core-shell structure, the functionalization of supporting carbon material, the application of a new sulfur source, and the selection of nanoparticle growth model. The Pt core-Rh_xS_y shell catalyst achieves 7 times higher mass-specific surface area compared to that of commercial Rh_xS_y catalyst. It also outperforms the Pt/C catalyst in the fuel cell cycling test. However, the attempt of replacing the expensive Pt core material by a cheaper metal like nickel failed due to the corrodible nature of cheap metal in the acidic $RhCl_3$ solution. Moreover, it is found that it is difficult to form an complete shell with high-temperature thermal treatment. Broken shells will result in a waste of expensive rhodium sulfide material. The core-shell method does not provide a satisfactory solution to the challenges of catalyst development in the H_2-Br_2 fuel cell.

Then the functionalization was used to create more active sites for the rhodium cation adsorption on the carbon surface. Besides the functionalization method, the diffusion-controlled growth mechanism of nanoparticle was developed by controlling the adding rate of sulfur source to reduce the average particle size. The TEM and cyclic voltammetry results confirm that the catalysts with treated carbon and diffusion-controlled nanoparticle growth approach have smaller average particle size (3.2 nm vs. 13.5 nm) and higher mass-specific ECSA (43 $m^2/g-Rh$ vs. 9.1 $m^2/g-Rh$) than those with the untreated carbon. In the study related to the usage of functionalized supporting material in this dissertation, it proves that the carbon with ketone surface groups is preferable for the adsorption of Rh cation when the PZC of the adsorbent is lower than the pH of the synthesis solution, and carboxylic surface groups impair the adsorption of Rh cation in this case. The ketone group on the modified catalyst, however, can influence the performance of this in a H_2-Br_2 fuel cell by changing the affinity between the catalyst and the Nafion ionomer. Consequently, due to the affinity issue between the ketone surface group and Nafion, improvements to the mass-specific surface area and the productivity of the catalyst were not adequately demonstrated in the H_2-Br_2 fuel cell.

The rhodium sulfide synthesized by the new sulfur source, Na_2S, is more active than the catalyst by the traditional sulfur source,$(NH_4)_2S_2O_3$. It can be contributed to the fast and complete release mechanism of S^{2-} of Na_2S that provide the extra S^{2-} in the amorphous Rh_2S_3 NPs which helps to form the active Rh_3S_4 phase in the thermal treatment due to the negative ΔG_r of the conversion from $Rh_{17}S_{15}$ to Rh_3S_4 with extra sulfur. The mass-specific exchange current of rhodium sulfide synthesized with the functionalized carbon material, diffusion-controlled particle growth model, and the Na_2S improves from $0.56\ \mathrm{A/mg-Rh}$ of the Rh_xS_y/untreated carbon with $(NH_4)_2S_2O_3$ as sulfur source to $2.8\ \mathrm{A/mg-Rh}$.

However, those excellent performances of the new Rh_xS_y catalysts were not adequately demonstrated in the fuel cell operation due to the affinity issue caused by the ketone group on the functionalized carbon material. The Nafion-unfriendly ketone group has to be converted into the Nafion-friendly carboxylic group. Both the electrochemical method and organic chemical method were explored. For the consideration of stability of the loaded catalyst, the Baeyer-Villiger reaction and ester hydrolysis were selected to accomplish the conversion. The cyclic voltammetry, TEM, and XRD results confirm that the mass-specific electrochemical surface area (ECSA/mass), average particle size and crystal phase composition do not change in the organic reaction process. It has proven in the H_2-Br_2 fuel cell tests that the Rh_xS_y on the pretreated carbon with carboxylic group outperforms all other rhodium sulfide catalysts including the commercial one. The discharge performance is increased by over 2.8 times compared to that of the commercial catalyst.

The successful development of high mass-specific activity rhodium sulfide catalyst is believed to facilitate the application and commercialization of H_2-Br_2 fuel cell and the energy storage system. Besides the H_2-Br_2 fuel cell, it can also help for the onsite electrolysis of the corrosive HBr/HCl for the production of Br_2/Cl_2, which are viewed as a market worth billions of dollars.

References

[1] Qingtao Luo, Huamin Zhang, Jian Chen, Dongjiang You, Chenxi Sun, and Yu Zhang. Preparation and characterization of nafion/speek layered composite membrane and its application in vanadium redox flow battery. *Journal of Membrane Science*, 325(2):553–558, 2008.

[2] Seyed Ehsan Hosseini, Amin Mahmoudzadeh Andwari, Mazlan Abdul Wahid, and Ghobad Bagheri. A review on green energy potentials in iran. *Renewable and Sustainable Energy Reviews*, 27:533–545, 2013.

[3] Godfrey Boyle. Renewable energy. *Renewable Energy, by Edited by Godfrey Boyle, pp. 456. Oxford University Press, May 2004. ISBN-10: 0199261784. ISBN-13: 9780199261789*, page 456, 2004.

[4] Magnus Korpaas, Arne T Holen, and Ragne Hildrum. Operation and sizing of energy storage for wind power plants in a market system. *International Journal of Electrical Power & Energy Systems*, 25(8):599–606, 2003.

[5] MH Albadi and EF El-Saadany. Overview of wind power intermittency impacts on power systems. *Electric Power Systems Research*, 80(6):627–632, 2010.

[6] U.S. Energy Information Administration. Us battery storage market trends. Technical report, May 2018.

[7] C Bueno and Jose A Carta. Wind powered pumped hydro storage systems, a means of increasing the penetration of renewable energy in the canary islands. *Renewable and Sustainable Energy Reviews*, 10(4):312–340, 2006.

[8] Samir Succar and RH Williams. Compressed air energy storage. *Theory, Resources, and Applications for Wind Power*, 2011.

[9] Gabriel O Cimuca, Christophe Saudemont, Benoit Robyns, and Mircea M Radulescu. Control and performance evaluation of a flywheel energy-storage system associated to a variable-speed wind generator. *IEEE Transactions on Industrial Electronics*, 53(4):1074–1085, 2006.

[10] Stefan Rönsch, Jens Schneider, Steffi Matthischke, Michael Schlüter, Manuel Götz, Jonathan Lefebvre, Praseeth Prabhakaran, and Siegfried Bajohr. Review on methanation–from fundamentals to current projects. *Fuel*, 166:276–296, 2016.

[11] Gutachten. Energiewirtschaftliche und ökologische bewertung eines windgas-angebotes. Technical report, February 2011.

[12] Li Li Zhang and XS Zhao. Carbon-based materials as supercapacitor electrodes. *Chemical Society Reviews*, 38(9):2520–2531, 2009.

[13] Warren Buckles and William V Hassenzahl. Superconducting magnetic energy storage. *IEEE Power Engineering Review*, 20(5):16–20, 2000.

[14] Luisa F Cabeza. Thermal energy storage. *Comprehensive renewable energy*, 3:211–253, 2012.

[15] John J Tomlinson and Landis D Kannberg. Thermal energy storage. *Mechanical Engineering*, 112(9):68, 1990.

[16] Languang Lu, Xuebing Han, Jianqiu Li, Jianfeng Hua, and Minggao Ouyang. A review on the key issues for lithium-ion battery management in electric vehicles. *Journal of power sources*, 226:272–288, 2013.

[17] Vinodkumar Etacheri, Rotem Marom, Ran Elazari, Gregory Salitra, and Doron Aurbach. Challenges in the development of advanced li-ion batteries: a review. *Energy & Environmental Science*, 4(9):3243–3262, 2011.

[18] Zhaoyin Wen, Jiadi Cao, Zhonghua Gu, Xiaohe Xu, Fuli Zhang, and Zuxiang Lin. Research

on sodium sulfur battery for energy storage. *Solid State Ionics*, 179(27-32):1697–1701, 2008.

[19] Joseph T Kummer and Weber Neill. Battery having a molten alkali metal anode and a molten sulfur cathode, Nov 1968.

[20] Sen Xin, Ya-Xia Yin, Yu-Guo Guo, and Li-Jun Wan. A high-energy room-temperature sodium-sulfur battery. *Advanced Materials*, 26(8):1261–1265, 2014.

[21] D Pavlov and P Nikolov. Lead–carbon electrode with inhibitor of sulfation for lead-acid batteries operating in the hrpsoc duty. *Journal of The Electrochemical Society*, 159(8):A1215–A1225, 2012.

[22] Leying Wang, Hao Zhang, Gaoping Cao, Wenfeng Zhang, Hailei Zhao, and Yusheng Yang. Effect of activated carbon surface functional groups on nano-lead electrodeposition and hydrogen evolution and its applications in lead-carbon batteries. *Electrochimica Acta*, 186:654–663, 2015.

[23] Wei Wang, Qingtao Luo, Bin Li, Xiaoliang Wei, Liyu Li, and Zhenguo Yang. Recent progress in redox flow battery research and development. *Advanced Functional Materials*, 23(8):970–986, 2013.

[24] Cong Ding, Huamin Zhang, Xianfeng Li, Tao Liu, and Feng Xing. Vanadium flow battery for energy storage: prospects and challenges. *The Journal of Physical Chemistry Letters*, 4(8):1281–1294, 2013.

[25] M Skyllas-Kazacos, MH Chakrabarti, SA Hajimolana, FS Mjalli, and M Saleem. Progress in flow battery research and development. *Journal of The Electrochemical Society*, 158(8):R55–R79, 2011.

[26] Werner Glass. Hydrogen-bromine fuel cell. Technical report, IONICS INC CAMBRIDGE MASS, 1964.

[27] Robert F Savinell and SD Fritts. Theoretical performance of hydrogen-bromine rechargeable spe fuel cell. 1987.

[28] V Livshits, A Ulus, and E Peled. High-power h2/br2 fuel cell. *Electrochemistry communications*, 8(8):1358–1362, 2006.

[29] William A Braff, Martin Z Bazant, and Cullen R Buie. Membrane-less hydrogen bromine flow battery. *Nature communications*, 4:2346, 2013.

[30] RS Yeo and D-T Chin. A hydrogen-bromine cell for energy storage applications. *Journal of The Electrochemical Society*, 127(3):549–555, 1980.

[31] S-J Shin, J-K Lee, H-Y Ha, S-A Hong, H-S Chun, and I-H Oh. Effect of the catalytic ink preparation method on the performance of polymer electrolyte membrane fuel cells. *Journal of power sources*, 106(1-2):146–152, 2002.

[32] Venkata Yarlagadda, Guangyu Lin, Pau Ying Chong, and Trung Van Nguyen. High surface area carbon electrodes for bromine reactions in h2-br2 fuel cells. *Journal of The Electrochemical Society*, 163(1):A5126–A5133, 2016.

[33] Venkata Yarlagadda, Guangyu Lin, Pau Ying Chong, and Trung Van Nguyen. High active surface area and durable multi-wall carbon nanotube-based electrodes for the bromine reactions in h2-br2 fuel cells. *Journal of The Electrochemical Society*, 163(1):A5134–A5143, 2016.

[34] Kenneth A Mauritz and Robert B Moore. State of understanding of nafion. *Chemical reviews*, 104(10):4535–4586, 2004.

[35] Venkata Yarlagadda, Regis P Dowd, Jun Woo Park, Peter N Pintauro, and Trung Van Nguyen. A comprehensive study of an acid-based reversible h2-br2 fuel cell system. *Journal of The Electrochemical Society*, 162(8):F919–F926, 2015.

[36] A HERMANN, T CHAUDHURI, and P SPAGNOL. Bipolar plates for PEM fuel cells: A review. *International Journal of Hydrogen Energy*, 30(12):1297–1302, September 2005.

[37] X LI and I SABIR. Review of bipolar plates in PEM fuel cells: Flow-field designs. *International Journal of Hydrogen Energy*, 30(4):359–371, March 2005.

[38] David L Wood III, S Yi Jung, and Trung V Nguyen. Effect of direct liquid water injection and interdigitated flow field on the performance of proton exchange membrane fuel cells. *Electrochimica Acta*, 43(24):3795–3809, 1998.

[39] Mahlon S Wilson and Shimshon Gottesfeld. Thin-film catalyst layers for polymer electrolyte fuel cell electrodes. *Journal of applied electrochemistry*, 22(1):1–7, 1992.

[40] Zhong Xie, Titichai Navessin, Ken Shi, Robert Chow, Qianpu Wang, Datong Song, Bernhard Andreaus, Michael Eikerling, Zhongsheng Liu, and Steven Holdcroft. Functionally graded cathode catalyst layers for polymer electrolyte fuel cells ii. experimental study of the effect of nafion distribution. *Journal of the Electrochemical Society*, 152(6):A1171–A1179, 2005.

[41] Guangyu Lin, Pau Ying Chong, Venkata Yarlagadda, TV Nguyen, RJ Wycisk, PN Pintauro, Michael Bates, Sanjeev Mukerjee, MC Tucker, and AZ Weber. Advanced hydrogen-bromine flow batteries with improved efficiency, durability and cost. *Journal of The Electrochemical Society*, 163(1):A5049–A5056, 2016.

[42] Joseph M Ziegelbauer, Daniel Gatewood, Andrea F Gulla, Maxime J-F Guinel, Frank Ernst, David E Ramaker, and Sanjeev Mukerjee. Fundamental investigation of oxygen reduction reaction on rhodium sulfide-based chalcogenides. *The Journal of Physical Chemistry C*, 113(17):6955–6968, 2009.

[43] Dhrubajit Konwar. *Synthesis and Characterization of Carbon-supported Rhodium Sulfide Catalyst*. PhD thesis, University of Kansas, 2015.

[44] Nirala Singh, David C Upham, Ru-Fen Liu, Jonathan Burk, Nick Economou, Steven Buratto, Horia Metiu, and Eric W McFarland. Investigation of the active sites of rhodium sulfide for hydrogen evolution/oxidation using carbon monoxide as a probe. *Langmuir*, 30(19):5662–5668, 2014.

[45] Oswaldo Diéguez and Nicola Marzari. First-principles characterization of the structure and electronic structure of α −S and Rh-S chalcogenides. *Physical Review B*, 80(21):1–6, December 2009.

[46] Jeff Greeley and Manos Mavrikakis. Alloy catalysts designed from first principles. *Nature materials*, 3(11):810, 2004.

[47] Li-Xian Sun and Tatsuhiro Okada. Studies on interactions between nafion and organic vapours by quartz crystal microbalance. *Journal of Membrane Science*, 183(2):213–221, 2001.

[48] Andrea F Gulla and Robert J Allen. Carbon-supported metal sulphide catalyst for electrochemical oxygen reduction, April 19 2016. US Patent 9,315,912.

[49] Adam Z Weber and Trung Van Nguyen. Redox Flow Batteries–Reversible Fuel Cells. *Journal of the Electrochemical Society*, 163(1):Y1–Y1, December 2015.

[50] Michael C Tucker, Kyu Taek Cho, Adam Z Weber, Guangyu Lin, and Trung Van Nguyen. Optimization of electrode characteristics for the Br2/H2 redox flow cell. *Journal of Applied Electrochemistry*, 45(1):11–19, October 2014.

[51] J Masud, T Van Nguyen, N Singh, E McFarland, M Ikenberry, bing joe hwang, keith Hohn, and Chun-Jern Pan. A RhxSy/C Catalyst for the Hydrogen Oxidation and Hydrogen Evolution Reactions in HBr. *Journal of the Electrochemical Society*, 162(4):F455–F462, January 2015.

[52] Nirala Singh, Michael Gordon, Horia Metiu, and Eric McFarland. Doped rhodium sulfide and thiospinels hydrogen evolution and oxidation electrocatalysts in strong acid electrolytes. *Journal of Applied Electrochemistry*, 46(4):497–503, December 2016.

[53] Nirala Singh, John Hiller, Horia Metiu, and Eric McFarland. Investigation of the Electrocatalytic Activity of Rhodium Sulfide for Hydrogen Evolution and Hydrogen Oxidation. *Electrochimica Acta*, 145:224–230, November 2014.

[54] T V Nguyen, H Kreutzer, V Yarlagadda, E McFarland, and N Singh. HER/HOR Catalysts for the H2-Br2 Fuel Cell System. *ECS Transactions*, 53(7):75–81, May 2013.

[55] Rajib Ghosh Chaudhuri and Santanu Paria. Core/shell nanoparticles: classes, properties, synthesis mechanisms, characterization, and applications. *Chemical reviews*, 112(4):2373–2433, 2011.

[56] Pu Zhang, Yan-Xia Chen, Jun Cai, Sang-Zi Liang, Jian-Feng Li, An Wang, Bin Ren, and Zhong-Qun Tian. An Electrochemical in Situ Surface-Enhanced Raman Spectroscopic Study of Carbon Monoxide Chemisorption at a Gold Core−Platinum Shell Nanoparticle Electrode with a Flow Cell. *The Journal of Physical Chemistry C*, 113(40):17518–17526, September 2009.

[57] RK Kirby. Platinum—a thermal expansion reference material. *International Journal of Thermophysics*, 12(4):679–685, 1991.

[58] Evgeny N Selivanov, OV Nechvoglod, and RI Gulyaeva. Thermal expansion of copper and nickel sulfides and their alloys. In *Defect and Diffusion Forum*, volume 334, pages 55–59. Trans Tech Publ, 2013.

[59] S Geller. The crystal structure of the superconductor rh17s15. *Acta Crystallographica*, 15(12):1198–1201, 1962.

[60] M Goor-Dar, Nina Travitsky, and Emanuel Peled. Study of hydrogen redox reactions on platinum nanoparticles in concentrated hbr solutions. *Journal of Power Sources*, 197:111–115, 2012.

[61] Abhishek Guha, Thomas A Zawodzinski Jr, and David A Schiraldi. Evaluation of electrochemical performance for surface-modified carbons as catalyst support in polymer electrolyte membrane (pem) fuel cells. *Journal of Power Sources*, 172(2):530–541, 2007.

[62] Xi Geng, Yinjie Cen, Richard D Sisson, and Jianyu Liang. An effective approach towards the immobilization of ptsn nanoparticles on noncovalent modified multi-walled carbon nanotubes for ethanol electrooxidation. *Energies*, 9(3):165, 2016.

[63] Takashi Ogi, Ratna Balgis, Kikuo Okuyama, Naoko Tajima, and Heru Setyawan. Influence of formic acid on electrochemical properties of high-porosity pt/tin nanoparticle aggregates. *AIChE Journal*, 59(8):2753–2760, 2013.

[64] Dongping Zhan, Jeyavel Velmurugan, and Michael V Mirkin. Adsorption/desorption of hydrogen on pt nanoelectrodes: Evidence of surface diffusion and spillover. *Journal of the American Chemical Society*, 131(41):14756–14760, 2009.

[65] Yu Sugawara, Takayoshi Okayasu, Amar Prasad Yadav, Atsushi Nishikata, and Tooru Tsuru. Dissolution mechanism of platinum in sulfuric acid solution. *Journal of The Electrochemical Society*, 159(11):F779–F786, 2012.

[66] Andrea F Gullá, Lajos Gancs, Robert J Allen, and Sanjeev Mukerjee. Carbon-supported low-loading rhodium sulfide electrocatalysts for oxygen depolarized cathode applications. *Applied Catalysis A: General*, 326(2):227–235, 2007.

[67] Donghwan Yoon, Bora Seo, Jaeyoung Lee, Kyoung Sik Nam, Byeongyoon Kim, Suhyun Park, Hionsuck Baik, Sang Hoon Joo, and Kwangyeol Lee. Facet-controlled hollow rh 2 s 3 hexagonal nanoprisms as highly active and structurally robust catalysts toward hydrogen evolution reaction. *Energy & Environmental Science*, 9(3):850–856, 2016.

[68] Young-Chul Park, Haruki Tokiwa, Katsuyoshi Kakinuma, Masahiro Watanabe, and Makoto Uchida. Effects of carbon supports on pt distribution, ionomer coverage and cathode performance for polymer electrolyte fuel cells. *Journal of Power Sources*, 315:179–191, 2016.

[69] Ralph G Pearson. Hard and soft acids and bases, hsab, part 1: Fundamental principles. *Journal of Chemical Education*, 45(9):581, 1968.

[70] Ralph G Pearson. Hard and soft acids and bases, hsab, part ii: Underlying theories. *Journal of Chemical Education*, 45(10):643, 1968.

[71] Robert J Buszek, Claron J Ridge, Samuel B Emery, C Michael Lindsay, and Jerry A Boatz. Theoretical Study of Cu/Mg Core–shell Nanocluster Formation. *The Journal of Physical Chemistry A*, 120(48):9612–9617, November 2016.

[72] Zhi Wei Seh, Jakob Kibsgaard, Colin F. Dickens, Ib Chorkendorff, Jens K. Nørskov, and Thomas F. Jaramillo. Combining theory and experiment in electrocatalysis: Insights into materials design. *Science*, 355(6321), 2017.

[73] Xiaoqing Huang, Zipeng Zhao, Liang Cao, Yu Chen, Enbo Zhu, Zhaoyang Lin, Mufan Li, Aiming Yan, Alex Zettl, Y. Morris Wang, Xiangfeng Duan, Tim Mueller, and Yu Huang. High-performance transition metal–doped pt3ni octahedra for oxygen reduction reaction. *Science*, 348(6240):1230–1234, 2015.

[74] Joseph M Barforoush, Dylan T Jantz, Tess E Seuferling, Kelly R Song, Laura C Cummings, and Kevin C Leonard. Microwave-assisted synthesis of a nanoamorphous (Ni 0.8,Fe 0.2) oxide oxygen-evolving electrocatalyst containing only “fast” sites. *Journal of Materials Chemistry A*, 5(23):11661–11670, 2017.

[75] Jason Tierney and Pelle Lidström. *Microwave assisted organic synthesis*. John Wiley & Sons, 2009.

[76] M Nüchter, B Ondruschka, W Bonrath, and A Gum. Microwave assisted synthesis–a critical technology overview. *Green chemistry*, 6(3):128–141, 2004.

[77] Daping He, Chao Zeng, Cheng Xu, Niancai Cheng, Huaiguang Li, Shichun Mu, and Mu Pan. Polyaniline-functionalized carbon nanotube supported platinum catalysts. *Langmuir*, 27(9):5582–5588, 2011.

[78] Cheng-Chuan Chen, Cheng-Lan Lin, and Lin-Chi Chen. Functionalized carbon nanomaterial supported palladium nano-catalysts for electrocatalytic glucose oxidation reaction. *Electrochimica Acta*, 152:408–416, 2015.

[79] Mohammad Saleh Shafeeyan, Wan Mohd Ashri Wan Daud, Amirhossein Houshmand, and Ahmad Shamiri. A review on surface modification of activated carbon for carbon dioxide adsorption. *Journal of Analytical and Applied Pyrolysis*, 89(2):143–151, 2010.

[80] Motoi Machida, Tomohide Mochimaru, and Hideki Tatsumoto. Lead (ii) adsorption onto the graphene layer of carbonaceous materials in aqueous solution. *Carbon*, 44(13):2681–2688, 2006.

[81] Sanae Sato, Kazuya Yoshihara, Koji Moriyama, Motoi Machida, and Hideki Tatsumoto. Influence of activated carbon surface acidity on adsorption of heavy metal ions and aromatics from aqueous solution. *Applied Surface Science*, 253(20):8554–8559, 2007.

[82] LR Radovic, IF Silva, JI Ume, JA Menendez, CA Leon Y Leon, and AW Scaroni. An experimental and theoretical study of the adsorption of aromatics possessing electron-withdrawing and electron-donating functional groups by chemically modified activated carbons. *Carbon*, 35(9):1339–1348, 1997.

[83] Jouko Kankare. Sauerbrey equation of quartz crystal microbalance in liquid medium. *Langmuir*, 18(18):7092–7094, 2002.

[84] Fan Yang, Le Xin, Aytekin Uzunoglu, Yang Qiu, Lia Stanciu, Jan Ilavsky, Wenzhen Li, and Jian Xie. Investigation of the interaction between nafion ionomer and surface functionalized carbon black using both ultrasmall angle x-ray scattering and cryo-tem. *ACS applied materials & interfaces*, 9(7):6530–6538, 2017.

[85] A Orfanidi, P Madkikar, HA El-Sayed, GS Harzer, T Kratky, and HA Gasteiger. The key to high performance low pt loaded electrodes. *Journal of The Electrochemical Society*, 164(4):F418–F426, 2017.

[86] Manuel Fernando R Pereira, Samanta F Soares, José JM Órfão, and José L Figueiredo. Adsorption of dyes on activated carbons: influence of surface chemical groups. *Carbon*, 41(4):811–821, 2003.

[87] PCC Faria, JJM Orfao, and MFR Pereira. Adsorption of anionic and cationic dyes on activated carbons with different surface chemistries. *Water Research*, 38(8):2043–2052, 2004.

[88] Pierre M Esteves, José Walkimar de M. Carneiro, Sheila P Cardoso, André GH Barbosa, Kenneth K Laali, Golam Rasul, GK Surya Prakash, and George A Olah. Unified mechanistic concept of electrophilic aromatic nitration: convergence of computational results and experimental data. *Journal of the American Chemical Society*, 125(16):4836–4849, 2003.

[89] Emma Sairanen, Reetta Karinen, Maryam Borghei, Esko I Kauppinen, and Juha Lehtonen. Preparation methods for multi-walled carbon nanotube supported palladium catalysts. *ChemCatChem*, 4(12):2055–2061, 2012.

[90] Tahira Mahmood, Muhammad Tahir Saddique, Abdul Naeem, Paul Westerhoff, Syed Mustafa, and Absar Alum. Comparison of different methods for the point of zero charge determination of nio. *Industrial & Engineering Chemistry Research*, 50(17):10017–10023, 2011.

[91] YF Jia, B Xiao, and KM Thomas. Adsorption of metal ions on nitrogen surface functional groups in activated carbons. *Langmuir*, 18(2):470–478, 2002.

[92] Kwan-Ho Park, Chang-Ho Lee, Seung-Kon Ryu, and Xiaoping Yang. Zeta-potentials of oxygen and nitrogen enriched activated carbons for removal of copper ion. *Carbon letters*, 8(4):321–325, 2007.

[93] Hideo Hata, Yoji Kobayashi, Vince Bojan, W Justin Youngblood, and Thomas E Mallouk. Direct deposition of trivalent rhodium hydroxide nanoparticles onto a semiconducting layered calcium niobate for photocatalytic hydrogen evolution. *Nano letters*, 8(3):794–799, 2008.

[94] Peter JF Harris, Zheng Liu, and Kazu Suenaga. Imaging the atomic structure of activated carbon. *Journal of Physics: Condensed Matter*, 20(36):362201, 2008.

[95] Nguyen Ngoc Ha et al. Theoretical study on the adsorption of phenol on activated carbon using density functional theory. *Journal of molecular modeling*, 19(10):4395–4402, 2013.

[96] Wuxing Zhang, Kazumichi Yanagisawa, Sumio Kamiya, and Tatsuo Shou. Phase controllable synthesis of well-crystallized rhodium sulfides by the hydrothermal method. *Crystal Growth and Design*, 9(8):3765–3770, 2009.

[97] I Bernard Rufus, V Ramakrishnan, B Viswanathan, and JC Kuriacose. Rhodium and rhodium sulfide coated cadmium sulfide as a photocatalyst for photochemical decomposition of aqueous sulfide. *Langmuir*, 6(3):565–567, 1990.

[98] Yuanchao Li and Trung Van Nguyen. Core-shell rhodium sulfide catalyst for hydrogen evolution reaction/hydrogen oxidation reaction in hydrogen-bromine reversible fuel cell. *Journal of Power Sources*, 382:152–159, 2018.

[99] Erika C Vreeland, John Watt, Gretchen B Schober, Bradley G Hance, Mariah J Austin, Andrew D Price, Benjamin D Fellows, Todd C Monson, Nicholas S Hudak, Lorena Maldonado-

Camargo, et al. Enhanced nanoparticle size control by extending lamer's mechanism. *Chemistry of Materials*, 27(17):6059–6066, 2015.

[100] Nguyen TK Thanh, N Maclean, and S Mahiddine. Mechanisms of nucleation and growth of nanoparticles in solution. *Chemical reviews*, 114(15):7610–7630, 2014.

[101] Tadao Sugimoto. Preparation of monodispersed colloidal particles. *Advances in Colloid and Interface Science*, 28:65–108, 1987.

[102] Spiros Olivotos and Maria Economou-Eliopoulos. Gibbs free energy of formation for selected platinum group minerals (pgm). *Geosciences*, 6(1):2, 2016.

[103] Matjaž Kristl, Brina Dojer, Sašo Gyergyek, and Janja Kristl. Synthesis of nickel and cobalt sulfide nanoparticles using a low cost sonochemical method. *Heliyon*, 3(3):e00273, 2017.

[104] Alan D McNaught and Alan D McNaught. *Compendium of chemical terminology*, volume 1669. Blackwell Science Oxford, 1997.

[105] Wilhelm Ostwald. Studien über die bildung und umwandlung fester körper. *Zeitschrift für physikalische Chemie*, 22(1):289–330, 1897.

[106] Johannes Beck and Tobias Hilbert. Ein, altes 'rhodiumsulfid mit überraschender struktur: Synthese, kristallstruktur und elektronische eigenschaften von rh3s4. *Zeitschrift für anorganische und allgemeine Chemie*, 626(1):72–79, 2000.

[107] Jinling He, Xiaofeng He, LiangLiang Liu, Binbin Hu, Feng Bai, Peng Zhang, and Yong Zhao. Tailoring carbon materials substrate to modify the electronic structure of platinum for boosting its electrocatalytic activity. *Journal of The Electrochemical Society*, 165(5):F247–F252, 2018.

[108] KT Jacob and Preeti Gupta. Gibbs free energy of formation of rhodium sulfides. *The Journal of Chemical Thermodynamics*, 70:39–45, 2014.

[109] Chenguang Liu, Zhenning Yu, David Neff, Aruna Zhamu, and Bor Z Jang. Graphene-based supercapacitor with an ultrahigh energy density. *Nano letters*, 10(12):4863–4868, 2010.

[110] Jie Jack Li. Baeyer–villiger oxidation. In *Name Reactions*, pages 12–13. Springer, 2009.

[111] Wenjing Angela Zhang. Electrospinning pt/c catalysts into a nanofiber fuel cell cathode. *The Electrochemical Society Interface*, 19(4):51, 2010.

Appendix A

Appendix I

All the data for the figures in this dissertation have been shared through Google drive. The linkages are summarized below.

1. The data for the figures in Section 3.1
2. The data for the figures in Section 3.2
3. The data for the figures in Section 3.3
4. The data for the figures in Section 3.4
5. The data for the figures in Section 3.5